

# General Relativistic Magnetohydrodynamic Simulations of Magnetically Choked Accretion Flows around Black Holes

Jonathan C. McKinney<sup>1\*</sup>, Alexander Tchekhovskoy<sup>2</sup>, Roger D. Blandford<sup>1</sup>

<sup>1</sup>Kavli Institute for Particle Astrophysics and Cosmology, Stanford University, P.O. Box 20450, MS 29, Stanford, CA 94309

<sup>2</sup>Center for Theoretical Science, Jadwin Hall, Princeton University, Princeton, NJ 08544; Princeton Center for Theoretical Science Fellow

Accepted 2012 Jan xx. Received 2012 Jan xx; in original form 2012 Jan xx.

## ABSTRACT

Black hole (BH) accretion flows and jets are qualitatively affected by the presence of ordered magnetic fields. We study fully three-dimensional global general relativistic magnetohydrodynamic (MHD) simulations of radially extended and thick (height  $H$  to cylindrical radius  $R$  ratio of  $|H/R| \sim 0.2$ –1) accretion flows around BHs with various dimensionless spins ( $a/M$ , with BH mass  $M$ ) and with initially toroidally-dominated ( $\phi$ -directed) and poloidally-dominated ( $R$ – $z$  directed) magnetic fields. Firstly, for toroidal field models and BHs with high enough  $|a/M|$ , coherent large-scale (i.e.  $\gg H$ ) dipolar poloidal magnetic flux patches emerge, thread the BH, and generate transient relativistic jets. Secondly, for poloidal field models, poloidal magnetic flux readily accretes through the disk from large radii and builds-up to a natural saturation point near the BH. While models with  $|H/R| \sim 1$  and  $|a/M| \leq 0.5$  do not launch jets due to quenching by mass infall, for sufficiently high  $|a/M|$  or low  $|H/R|$  the polar magnetic field compresses the inflow into a geometrically thin highly non-axisymmetric “magnetically choked accretion flow” (MCAF) within which the standard linear magneto-rotational instability is suppressed. The condition of a highly-magnetized state over most of the horizon is optimal for the Blandford-Znajek mechanism that generates persistent relativistic jets with  $\gtrsim 100\%$  efficiency for  $|a/M| \gtrsim 0.9$ . A magnetic Rayleigh-Taylor and Kelvin-Helmholtz unstable magnetospheric interface forms between the compressed inflow and bulging jet magnetosphere, which drives a new jet-disk quasi-periodic oscillation (JD-QPO) mechanism. The high-frequency QPO has spherical harmonic  $|m| = 1$  mode period of  $\tau \sim 70GM/c^3$  for  $a/M \sim 0.9$  with coherence quality factors  $Q \gtrsim 10$ . Overall, our models are qualitatively distinct from most prior MHD simulations (typically,  $|H/R| \ll 1$  and poloidal flux is limited by initial conditions), so they should prove useful for testing accretion-jet theories and measuring  $a/M$  in systems such as SgrA\* and M87.

**Key words:** accretion, accretion discs, black hole physics, hydrodynamics, (magnetohydrodynamics) MHD, methods: numerical, gravitation

## 1 INTRODUCTION

Modern black hole (BH) accretion disk theory suggests that angular momentum transport, in the past modelled using an  $\alpha$ -viscosity (Shakura & Sunyaev 1973; Novikov & Thorne 1973; Thorne 1974), is due to magnetohydrodynamic (MHD) turbulence driven by the magneto-rotational instability (MRI) within a differentially rotating disk (Balbus & Hawley 1991, 1998) and due to large-scale magnetic torques within the plunging region of a BH (Znajek 1976; MacDonald 1984; Gammie 1999; Krolik 1999; Agol & Krolik 2000; Li 2000; Li & Paczyński 2000; Li 2002; Reynolds et al. 2006; Oda et al. 2009, 2010; Penna et al. 2012). However, even outside

the plunging region, transport may occur via large-scale magnetic field threading the disk (e.g., Blandford 1976; Lovelace 1976; Cao 2011) or even by ordered field within the disk far beyond the plunging region (Bisnovatyi-Kogan & Ruzmaikin 1974, 1976; Narayan et al. 2003; Bisnovatyi-Kogan & Lovelace 2007).

How are strong, large-scale, or ordered magnetic fields generated in BH accretion flows? The MHD turbulence increases the magnetic field’s *strength* up to some non-linear saturation point, while the solenoidal constraint in electrodynamics that  $\nabla \cdot \mathbf{B} = 0$  for magnetic field  $\mathbf{B}$  ensures that, within some radius  $r_0$ , the magnetic field’s *flux* (e.g.  $\int_0^{r_0} B^z dA$  at the equator for vertical field  $B^z$  and equatorial area  $A$ ) remains fixed unless added at  $r_0$ .

Patches of constant polarity magnetic flux might form stochastically out of an MHD dynamo (Tout & Pringle 1996) as occurs for

\* E-mail: jmckinne@stanford.edu (JCM)

the toroidal ( $\phi$ -directed) magnetic field as seen in MHD simulations (Davis et al. 2010; Guan & Gammie 2011) and for the large-scale poloidal ( $R$ - $z$ -directed) magnetic field as seen in the Sun (Babcock 1959). However, so far no evidence exists for the development of large-scale poloidal field from only a dominant toroidal field (De Villiers et al. 2005). The MRI-driven MHD turbulence-generated poloidal field remains small-scale on the order of the disk height (often used to estimate jet field strength, e.g. in Meier 2001 and Livio et al. 2003) and does not sustain relativistic jets due to persistent mass-loading (Beckwith et al. 2008a). Patches of constant polarity flux may also develop by the Poynting-Robertson drag (PRD) effect (Contopoulos & Kazanas 1998), but the PRD effect might saturate at low field strengths (Bisnovaty-Kogan et al. 2002).

An alternative is that ordered constant polarity magnetic flux comes from large radii, as implicit in outflow models (Blandford 1976; Blandford & Znajek 1977; Blandford & Payne 1982; Narayan et al. 2007; Tchekhovskoy et al. 2009, 2010a,b), but transport of flux from large radii may be inefficient (Lubow et al. 1994; Spruit & Uzdensky 2005; Rothstein & Lovelace 2008; Beckwith et al. 2009). Such magnetic fields can lead to angular momentum transport within the disk and out of a rotating BH (the latter having some observational basis; Narayan & McClintock 2012). Indeed, production of persistent relativistic jets may require steady large-scale dipolar (i.e. sub-dominant higher multipoles) fields near BHs (Beckwith et al. 2008a; McKinney & Blandford 2009).

Observations do show patches of coherent magnetic flux ( $\Phi$ ) surrounding astrophysical systems that can feed BHs. The interstellar medium has  $\Phi \sim 0.1\text{pc}^2\text{G}$  (Lang et al. 1999; Vallée 2011), threads near the Galactic Nucleus have  $\Phi \gtrsim 0.01\text{pc}^2\text{G}$  (LaRosa et al. 2004; Ferrière 2009; Vallée 2011), and each O-type star with a dipolar field with strength  $B \sim 1000\text{G}$  feeding SgrA\* provides up to  $\Phi \sim 10^{-10}\text{pc}^2\text{G}$ . Such a coherent flux might be available for accretion near SgrA\*, M87, and other active galactic nuclei (AGNs). Indeed, the constancy over several years of the sign of the circular polarization from near the BH in SgrA\* implies that the magnetic field is coherent with constant polarity for many dynamical times (Muñoz et al. 2012). Also, many AGN jets show persistent signs for the transverse Faraday rotation gradient, indicating accretion of a persistent magnetic polarity (e.g., Mahmud et al. 2009; Broderick & McKinney 2010). For BH x-ray binaries, some portion of the donor star's surface dipolar field of order  $B \sim 100\text{--}1000\text{G}$  may be available for accretion, such that  $\Phi \sim 10^{-13}\text{--}10^{-12}\text{pc}^2\text{G}$  (Justham et al. 2006). For cosmological gamma-ray bursts (GRBs) that require  $B \sim 3 \times 10^{15}\text{G}$  for MHD-driven jets by the Blandford-Znajek (BZ) mechanism (Blandford & Znajek 1977; Narayan et al. 1992; Barkov & Komissarov 2008), one obtains a requirement of  $\Phi \sim 10^{-9}\text{pc}^2\text{G}$  corresponding to about 10% of the total ordered poloidal flux within a presupernova progenitor (Heger et al. 2005; Komissarov & Barkov 2009). Even if  $N$  random polarity patches accrete over time, on average  $\Phi \propto N^{1/2}$  in a random walk near the BH. Some flux can annihilate before reaching the BH, but field reversals are unlikely to have exactly equal flux magnitude and so magnetic flux should tend to accumulate.

Magnetic flux is conserved such that accumulation of a sufficient amount of constant polarity poloidal magnetic flux brought in from large radii might substantially modify the standard picture of an MRI-driven MHD turbulent disk that applies for relatively weak magnetic field. Accumulation of magnetic flux can eventually lead to the formation of a semi-permeable magnetic barrier (Bisnovaty-Kogan & Ruzmaikin 1976), and in such a state the inflow must somehow accrete through the accumulated magnetosphere.

The inflow strongly interacts with the magnetospheric barrier

at the “magnetospheric radius”  $r_m$ , where the force of gravity by the accreting mass equals the magnetic force by the barrier.  $r_m$  is readily estimated in a similar way for both neutron stars (NSs) (Lamb et al. 1973; Elsner & Lamb 1977; Scharlemann 1978) and BHs (Bisnovaty-Kogan & Ruzmaikin 1974; Narayan et al. 2003). The disk surface density  $\Sigma$  inside  $r_m$  is  $\Sigma = \dot{M}/(2\pi r v_{\text{ff}})$ , where  $\dot{M}$  is the mass accretion rate.  $\epsilon \equiv 10\epsilon_{-1}$  is the ratio of mass advection velocity to free-fall velocity ( $v_{\text{ff}}$ ), where  $\epsilon \sim 0.1$  in our simulations discussed later. Also, let  $\dot{M} = \dot{M}_{\text{H}} (r/r_g)^n$  for horizon accretion rate  $\dot{M}_{\text{H}}$ , as in Blandford & Begelman (1999). The condition for magnetic support against disk gravity in the equatorial plane is  $G M \Sigma / r^2 \sim 2 B_r B_z / (4\pi) \sim B_z^2 / (2\pi)$  for  $B_r \sim B_z$ . Then,  $B_z \sim 10^5 \epsilon_{-1}^{1/2} m_8^{-1/2} \dot{m}^{1/2} (r/r_g)^{-5/4+n/2} \text{G}$ , where  $r_g = GM/c^2$ ,  $c$  is the speed of light,  $G$  is the gravitational constant,  $M$  is the BH mass,  $m_8 \equiv M/(10^8 M_\odot)$ ,  $\dot{m} \equiv \dot{M}/\dot{M}_{\text{Edd}}$ , and  $\dot{M}_{\text{Edd}} \equiv L_{\text{Edd}}/(0.1c^2) \approx 1.4 \times 10^{25} m_8 \text{ g s}^{-1}$  is the Eddington mass accretion rate. If  $\epsilon$  is independent of  $r$ , integrating  $B_z$  over  $r$  gives an estimate of  $\Phi$  within the “magnetospheric radius”  $r_m$ . Inverting  $\Phi(r_m)$  gives

$$r_m \sim r_g \left( 12000 \left( \frac{3}{4} + \frac{n}{2} \right) \right)^{\frac{4}{3+2n}} \epsilon_{-1}^{\frac{2}{3+2n}} m_8^{-\frac{6}{3+2n}} \dot{m}_H^{-\frac{2}{3+2n}} \left( \frac{\Phi}{0.1\text{pc}^2\text{G}} \right)^{\frac{4}{3+2n}}, \quad (1)$$

such that  $r_m$  varies weakly with parameters for higher  $n$  and for  $n = \{0, 1, 2\}$  the coefficient is  $\sim \{10^5, 10^3, 10^2\} r_g$ , respectively. As another measure of how important the magnetic flux is, we also consider the limit that all the surrounding flux ( $\Phi$ ) reaches the BH. Then, the horizon's dimensionless magnetic flux would be

$$\Upsilon_{\text{H}} \approx \frac{\Phi}{5(r_g^2 c M_{\text{H}})^{1/2}} \sim 10^4 m_8^{-3/2} \dot{m}_H^{-1/2} \left( \frac{\Phi}{0.1\text{pc}^2\text{G}} \right), \quad (2)$$

(Gammie 1999; Penna et al. 2010), which measures the mass-loading of the magnetic field lines. An MRI-driven MHD turbulent disk has  $\Upsilon_{\text{H}} \lesssim 1$  for integrals within the heavy disk inflow (Gammie 1999; Penna et al. 2010). If  $\Upsilon_{\text{H}} \gtrsim 1$  for integrals over some portion of the horizon (e.g. polar regions or heavy disk inflow), then this indicates the formation of a force-free magnetosphere and the BZ effect can be activated there (Komissarov & Barkov 2009).

The quantities  $r_m^{n=0}$ ,  $r_m^{n=1}$ , and  $\Upsilon_{\text{H}}$  can be estimated for various systems (using  $\Phi$  estimated in a preceding paragraph) to check whether a magnetosphere could dominate the flow dynamics. For M87 with  $\Phi \sim 0.1\text{pc}^2\text{G}$ ,  $M \approx 6.4 \times 10^9 M_\odot$ , mass accretion rate  $\dot{m}_{\text{H}} \sim 10^{-4}$  (Dexter et al. 2011), one obtains  $r_m^{n=0} \sim 10^3 r_g$ ,  $r_m^{n=1} \sim 10^2 r_g$ , and  $\Upsilon_{\text{H}} \sim 10^3$ . For SgrA\* with  $\Phi \sim 0.1\text{pc}^2\text{G}$ ,  $M \approx 4.5 \times 10^6 M_\odot$ , mass accretion rate  $\dot{m}_{\text{H}} \sim 1.5 \times 10^{-6}$  (Dexter et al. 2010), one obtains  $r_m^{n=0} \sim 10^{11} r_g$ ,  $r_m^{n=1} \sim 10^7 r_g$ , and  $\Upsilon_{\text{H}} \sim 10^9$ . A single O-type star feeding SgrA\* would give  $r_m \sim r_g$  for  $n = 0, 1, 2$  and  $\Upsilon_{\text{H}} \sim 2$ . For GRS1915+105 with  $\Phi \sim 10^{-12}\text{pc}^2\text{G}$ ,  $M \sim 15 M_\odot$ ,  $\dot{m}_{\text{H}} \sim 0.7$  (Greiner et al. 2001), one obtains  $r_m^{n=0} \sim 10^4 r_g$ ,  $r_m^{n=1} \sim 10^3 r_g$ , and  $\Upsilon_{\text{H}} \sim 10^4$ . For cosmological long-duration GRBs with  $\Phi \sim 10^{-9}\text{pc}^2\text{G}$ ,  $M \sim 3 M_\odot$  and  $\dot{M}_{\text{H}} \sim 0.1 M_\odot \text{ s}^{-1}$  (Woosley et al. 1993), one obtains  $r_m^{n=0} < r_g$ ,  $r_m^{n=1} \sim r_g$ , and  $\Upsilon_{\text{H}} \sim 1$ . One obtains only smaller  $r_m$  and  $\Upsilon_{\text{H}}$  for short-duration GRBs as modelled by NS-NS or BH-NS collisions that reach higher  $\dot{M}$  at similar  $\Phi$ . For GRBs, at late time  $\dot{M}_{\text{H}}$  drops, after which  $r_m$  and  $\Upsilon_{\text{H}}$  can be much higher (Proga & Zhang 2006). These estimates show that one must consider how plasma accretes through a magnetospheric barrier. For SgrA\* (where  $n \sim 1$  is plausible), even a millionth of  $\Phi$  is sufficient to lead to magnetospheric accretion near the BH.

Such flows with accumulated magnetic flux, called “magnetically choked accretion flows” (MCAFs) by us for reasons based upon our simulation results described later, have been considered theoretically (Znajek 1976; Bisnovaty-Kogan & Ruzmaikin 1976;

Narayan et al. 2003), via pseudo-Newtonian MHD simulations (Igumenshchev & Narayan 2002; Igumenshchev et al. 2003; Pen et al. 2003; Igumenshchev 2008; Pang et al. 2011), and via general relativistic (GR) MHD (GRMHD) simulations (Tchekhovskoy et al. 2011). MCAFs are qualitatively related to flows with strong magnetic field (Shibata et al. 1990; Mineshige et al. 1995; Machida et al. 2006; Oda et al. 2007; Fragile & Meier 2009).

MCAFs effectively accrete through a magnetic flux barrier via magnetic interchange type modes (Kruskal-Schwarzschild or magnetic Rayleigh-Taylor instabilities) (Wang 1984; Kaisig et al. 1992; Lovelace et al. 1994; Spruit et al. 1995; Lubow & Spruit 1995; Wang 1996; Stehle & Spruit 2001; Nakamura et al. 2002; Narayan et al. 2003; Li & Narayan 2004; Spruit & Uzdensky 2005; Stone & Gardiner 2007; Johansen & Levin 2008). Even with flow shear that might remove some specific magnetic interchange modes, still other non-axisymmetric magnetic modes operate (Tagger & Pellat 1999; Stehle & Spruit 2001). Interchange modes may also affect jet formation and propagation (Nakamura et al. 2002). One might expect that magnetic flux accumulation could be prevented by Parker-type instabilities (Parker 1966; Johansen & Levin 2008). However, the Parker instability cannot operate if the magnetic pressure dominates the gas pressure due to strong magnetic tension (Shibata et al. 1990). The MCAF-type state is also seen in other systems that develop a magnetosphere, including young-stellar objects, star formation regions (Cunningham et al. 2012), and neutron stars (Mestel & Strittmatter 1967; Arons & Lea 1976, 1980; Burnard et al. 1983; Aly & Kuijpers 1990; Shu et al. 1994; Romanova et al. 2008; Kulkarni & Romanova 2008; Romanova et al. 2011). Unlike these systems that can have a closed dipolar magnetosphere, BHs harbor a split-monopolar magnetosphere (Igumenshchev 2008).

Most 3D pseudo-Newtonian MHD simulations (except in Igumenshchev et al. 2003; Igumenshchev 2008) and most 3D GRMHD simulations (except in Tchekhovskoy et al. 2011, 2012; Tchekhovskoy & McKinney 2012) of accretion disks have only considered relatively weak magnetic fields leading to little accumulated poloidal flux. Such simulations do not reach the MCAF state (for GRMHD simulations, e.g., see De Villiers et al. 2003; McKinney & Gammie 2004; McKinney 2005; De Villiers et al. 2005; Hawley & Krolik 2006; McKinney 2006b; Komissarov & McKinney 2007; Komissarov et al. 2007; McKinney & Narayan 2007a,b; Fragile et al. 2007; Beckwith et al. 2008a; McKinney & Blandford 2009; Noble et al. 2010; Shiokawa et al. 2012), typically because their initial conditions used relatively small-sized hydro-equilibrium tori within which weak magnetic fields are inserted (so only little poloidal flux can accumulate, see section 4.3 in Igumenshchev et al. 2003). Tchekhovskoy et al. (2011) also used an initial torus, but the torus is radially extended and they ensured the initial conditions make available a sufficient amount of magnetic flux to reach flux saturation near the BH. Note that 3D is required for simulations to avoid decaying turbulence (Cowling 1934) and to properly resolve a MCAF. For example, the suspended inflow seen in 2D axisymmetric MHD simulations (McKinney & Gammie 2004; Proga & Zhang 2006; Komissarov & Barkov 2009) is due to axisymmetry (Igumenshchev 2008, 2009). Other 2D MHD simulations have constant poloidal flux due to using a purely radial field (Proga & Begelman 2003), which gives results similar to torus simulations with limited poloidal flux.

Also, MHD simulations have typically studied relatively thin disks compared to expected for radiatively inefficient accretion flows (RIAFs), as applicable to (e.g.) SgrA\*, M87, and some x-ray binary states. Quasi-analytical RIAF models include advection-dominated accretion flows (ADAFs) (Ichimaru 1977; Narayan & Yi

1994, 1995b; Abramowicz et al. 1996, 1995; Popham & Gammie 1998), convection-dominated accretion flows (CDAFs) (Narayan et al. 2000; Quataert & Gruzinov 2000), and advection-dominated inflow-outflow solutions (ADIOSs) (Blandford & Begelman 1999; Begelman 2011). These models suggest that RIAFs should have disk height ( $H$ ) to cylindrical radius ( $R$ ) ratio of  $|H/R| \sim 0.5\text{--}0.9$ . Simulations have studied  $|H/R| \sim 0.05\text{--}0.1$  (Shafee et al. 2008; Reynolds & Miller 2009; Noble et al. 2009, 2010; Sorathia et al. 2010; Beckwith et al. 2011),  $|H/R| \sim 0.1\text{--}0.15$  (Hawley & Krolik 2001; De Villiers et al. 2003; Beckwith et al. 2008b,a, 2009),  $|H/R| \sim 0.2$  (Hawley & Balbus 2002; Machida et al. 2000; Machida & Matsumoto 2003; McKinney & Gammie 2004; Fragile et al. 2007; McKinney & Blandford 2009),  $|H/R| \sim 0.3\text{--}0.4$  (Igumenshchev et al. 2003; Penna et al. 2010),  $|H/R| \sim 0.6$  (Run F type in Stone & Pringle 2001; Hawley et al. 2001), and rarely  $|H/R| \sim 1$  (Igumenshchev & Narayan 2002; Pen et al. 2003; Pang et al. 2011).

In this work, we use fully 3D GRMHD simulations to study radially extended and thick (including  $|H/R| \sim 1$ ) radiatively inefficient BH accretion flows with poloidal and toroidal magnetic field geometries and various  $a/M$ . Our initially poloidally-dominated field models are designed so that near the horizon the poloidal magnetic flux reaches a saturation point independent of the initial poloidal magnetic flux. Most prior MHD simulations would have only required a few times more poloidal magnetic flux to reach this natural saturation point. The only other natural limit of poloidal magnetic flux is its negligible. So, for comparison, we also consider models with initially toroidally-dominated magnetic field.

The equations solved are presented in §2, diagnostics are described in §3, and models are described in §4. Results for our fiducial model of a thick disk around a rapidly rotating BH are in §5. Results for various field geometries, BH spins, and disk thicknesses are in §6. We discuss our results in §7 and conclude in §8. Some numerical method details are given in Appendix A.

## 2 GOVERNING EQUATIONS

We solve the GRMHD equations for a radiatively inefficient magnetized accretion flow around a rotating black hole defined by the Kerr metric in Kerr-Schild coordinates with internal coordinates  $\underline{x}^\alpha \equiv (t, \underline{x}^{(1)}, \underline{x}^{(2)}, \underline{x}^{(3)})$  mapped to the spherical polar coordinates  $\underline{r}^\alpha \equiv (t, r, \theta, \phi)$ . We write orthonormal vectors as  $u_i$ , contravariant (covariant) vectors as  $\underline{u}^i$  ( $\underline{u}_i$ ), and higher-ranked coordinate basis tensors with no underbar. We work with Heaviside-Lorentz units, often set  $c = GM = 1$ , and let the horizon radius be  $r_H$ .

Mass conservation gives

$$\nabla_\mu(\rho_0 \underline{u}^\mu) = 0, \quad (3)$$

where  $\rho_0$  is the rest-mass density,  $\underline{u}^\mu$  is the contravariant 4-velocity, and  $\rho = \rho_0 \underline{u}^\mu$  is the lab-frame mass density.

Energy-momentum conservation gives

$$\nabla_\mu T^\mu_\nu = 0, \quad (4)$$

where the stress energy tensor  $T^\mu_\nu$  includes both matter (MA) and electromagnetic (EM) terms:

$$\begin{aligned} T^{\text{MA}\mu}_\nu &= (\rho_0 + u_g + p_g) \underline{u}^\mu \underline{u}_\nu + p_g \delta^\mu_\nu, \\ T^{\text{EM}\mu}_\nu &= b^2 \underline{u}^\mu \underline{u}_\nu + p_b \delta^\mu_\nu - \underline{b}^\mu \underline{b}_\nu, \\ T^\mu_\nu &= T^{\text{MA}\mu}_\nu + T^{\text{EM}\mu}_\nu. \end{aligned} \quad (5)$$

The MA term can be decomposed into a particle (PA) term:  $T^{\text{PA}\mu}_\nu = \rho_0 \underline{u}_\nu \underline{u}^\mu$  and an enthalpy (EN) term. The MA term can be reduced to

a free thermo-kinetic energy (MAKE) term, which is composed of free particle (PAKE) and enthalpy (EN) terms:

$$T^{\text{MAKE}\mu}_v = T^{\text{MA}\mu}_v - \rho_0 \underline{u}^\mu \underline{\eta}_v / \alpha, \quad (6)$$

$$T^{\text{PAKE}\mu}_v = (\underline{u}_v - \underline{\eta}_v / \alpha) \rho_0 \underline{u}^\mu,$$

$$T^{\text{EN}\mu}_v = (u_g + p_g) \underline{u}^\mu \underline{u}_v + p_g \delta^\mu_v,$$

such that  $T^{\text{MAKE}\mu}_v = T^{\text{PAKE}\mu}_v + T^{\text{EN}\mu}_v$ . Here,  $u_g$  is the internal energy density and  $p_g = (\Gamma - 1)u_g$  is the ideal gas pressure with adiabatic index  $\Gamma = 4/3$  ( $\Gamma = 5/3$  may lead to somewhat different results; McKinney & Gammie 2004; Mignone & McKinney 2007). The contravariant fluid-frame magnetic 4-field is given by  $\underline{b}^\mu$ , which is related to the lab-frame 3-field via  $\underline{b}^\mu = \underline{B}^\nu h^\mu_\nu / \underline{u}^\mu$  where  $h^\mu_\nu = \underline{u}^\mu \underline{u}_\nu + \delta^\mu_\nu$  is a projection tensor, and  $\delta^\mu_\nu$  is the Kronecker delta function. The magnetic energy density ( $u_b$ ) and pressure ( $p_b$ ) are  $u_b = p_b = \underline{b}^\mu \underline{b}_\mu / 2 = b^2 / 2$ . The total pressure is  $p_{\text{tot}} = p_g + p_b$ , and plasma  $\beta \equiv p_g / p_b$ . The 4-velocity of a zero angular momentum observer (ZAMO) is  $\underline{\eta}_\mu = \{-\alpha, 0, 0, 0\}$  where  $\alpha = 1 / \sqrt{-g^{tt}}$  is the lapse. The 4-velocity relative to this ZAMO is  $\underline{\tilde{u}}^\mu = \underline{u}^\mu - \gamma \underline{\eta}^\mu$  where  $\gamma = -\underline{u}^\alpha \underline{\eta}_\alpha$ . For any 3-vector (e.g.  $\underline{B}^i$ ), the “quasi-orthonormal” vector is  $B_i \equiv \underline{B}^i \sqrt{g_{ii}}$  computed in spherical polar coordinates.

Magnetic flux conservation is given by the induction equation

$$\partial_t (\sqrt{-g} \underline{B}^i) = -\partial_j [\sqrt{-g} (\underline{B}^i \underline{v}^j - \underline{B}^j \underline{v}^i)], \quad (7)$$

where  $g = \text{Det}(g_{\mu\nu})$  is the metric’s determinant, and the lab-frame 3-velocity is  $\underline{v}^i = \underline{u}^i / \underline{u}^t$ . No explicit viscosity or resistivity are included, but we use the energy conserving HARM scheme so all dissipation is captured (Gammie et al. 2003; McKinney 2006a).

The energy-momentum conservation equations are only modified due to so-called numerical density floors that keep the numerical code stable as described in detail in Appendix A. The injected densities are tracked and removed from all calculations.

### 3 DIAGNOSTICS

Diagnostics are computed from snapshots produced every  $\sim 2r_g/c$ . For quantities  $Q$ , averages over space ( $\langle Q \rangle$ ) and time ( $[Q]_t$ ) are performed directly on  $Q$  (e.g. on  $v_\phi$  rather than on any intermediate values). Any flux ratio vs. time with numerator  $F_N$  and denominator  $F_D$  ( $F_D$  often being mass or magnetic flux) is computed as  $R(t) = \langle F_N(t) \rangle / \langle F_D(t) \rangle_t$ . Time-averages are then computed as  $[R]_t$ .

#### 3.1 Fluxes and Averages vs. Radius

For flux density  $F_d$ , the flux integral is

$$F(r) \equiv \int dA_{23} F_d, \quad (8)$$

where  $dA_{23} = \sqrt{-g} d\underline{x}^{(2)} d\underline{x}^{(3)}$  ( $dA_{\theta\phi}$  is the spherical polar version). For example,  $F_d = \rho_0 \underline{u}^{(1)}$  gives  $F = \dot{M}$ , the rest-mass accretion rate. For weight  $w$ , the average of  $Q$  is

$$Q_w(r) \equiv \langle Q \rangle_w \equiv \frac{\int dA_{\theta\phi} w Q}{\int dA_{\theta\phi} w}, \quad (9)$$

All  $\theta, \phi$  angles are integrated over.

#### 3.2 Fluxes and Averages vs. $\theta$

The flux angular distribution, at any given radius, is

$$F(\theta) = \int_{\theta'=0}^{\pi/2-|\theta-\pi/2|} dA_{\theta'\phi} F_d + \int_{\theta'=\pi/2+|\theta-\pi/2|}^{\pi} dA_{\theta'\phi} F_d, \quad (10)$$

which just integrates up from both poles towards the equator, is symmetric about the equator, and gives the total flux value at  $\theta = \pi/2$ . The average of  $Q$  vs.  $\theta$  using weight  $w$  is given by

$$Q_w(\theta) = \frac{\int dA_{\theta\phi} w Q}{\int dA_{\theta\phi} w}. \quad (11)$$

All  $\phi$ -angles are integrated over.

### 3.3 Disk Thickness Measurements

The disk’s geometric half-angular thickness is given by

$$\theta^d \equiv \left( \langle (\theta - \theta_0)^2 \rangle_\rho \right)^{1/2}, \quad (12)$$

where we integrate over all  $\theta$  for each  $r, \phi$ , and  $\theta_0 \equiv \pi/2 + \langle (\theta - \pi/2) \rangle_\rho$  is also integrated over all  $\theta$  for each  $r, \phi$ , and the final  $\theta^d(r)$  is from  $\phi$ -averaging with no additional weight or  $\sqrt{-g}$  factor. This way of forming  $\theta^d(r)$  works for slightly tilted thin disks or disordered thick disks. For a Gaussian distribution in density, this satisfies  $\rho/(\rho[\theta = 0]) \sim \exp(-\theta^2/(2(\theta^d)^2))$ . For sound speed  $c_s = \sqrt{\Gamma p_g/(\rho_0 + u_g + p_g)}$ , the thermal half-angular thickness is

$$\theta_w^t \equiv \arctan \left( \frac{\langle c_s \rangle_w}{\langle v_{\text{rot}} \rangle_w} \right), \quad (13)$$

where  $v_{\text{rot}}^2 = v_\phi^2 + v_\theta^2$ . For a thin hydrostatic non-relativistic Keplerian (i.e.  $v_{\text{rot}} = |v_K|$  with  $v_K \approx R/(a + R^{3/2})$ ) Gaussian disk,  $\theta^d = c_s/v_{\text{rot}}$  for  $c_s$  and  $v_{\text{rot}}$  at the disk plane. Also,  $\theta_\rho^t \approx 0.93\theta^d$  for  $\Gamma = 4/3$ . Ram pressure forces (Beskin & Tchekhovskoy 2005) and magnetic forces (Cao 2011) can cause  $\theta^d \ll \theta^t$ . See Tables 1, 3. Note that ADAFs have  $\theta^t \gtrsim 1$  (Narayan & Yi 1994).

### 3.4 BH, Disk, Jet, Magnetized Wind, and Entire Wind

Many quantities ( $Q$ ) vs.  $r$  or vs.  $\theta$  or vs.  $\phi$  are considered for various weights and conditions. We define the superscript “f” (full flow) case as applies for weight  $w = 1$  with no conditions, “fdc” (full flow except avoids highly magnetized jet where numerical floors are activated), “dc” (disk plus corona but no jet) case as applies for  $w = 1$  with condition  $b^2/\rho_0 < 1$ , “dcden” (density-weighted average) with  $w = \rho$  and no conditions, “ $\theta^d$ ” (within 1 disk half-angular thickness) case with  $w = 1$  and condition of  $|\theta - \theta_0| < \theta^d$ , “eq” (within 3 cells around the equator) case with  $w = 1$ , and “jet” or “j” case (jet only) with  $w = 1$  and the condition that density floors are activated (see Appendix A). For quantities vs.  $\theta$  or vs.  $\phi$ , we radially average within  $\pm 0.1r$  at radius  $r$ .

Fluxes, described in the next section, have integrals computed for a variety of (somewhat arbitrary) conditions. The subscript “BH” or “H” is for all angles on the horizon. The subscript “j” or “jet” is for the “jet” with condition  $b^2/\rho_0 \geq 1$ . When the jet is measured at a single radius, we use  $r = 50r_g$  (except the MB09Q model that uses  $r = 30r_g$  due to its limited radial range). The subscript “mw” is for the “magnetized wind” with conditions  $b^2/\rho_0 < 1$  and  $\beta < 2$  for all fluxes, except for the rest-mass flux that also has  $-(\rho_0 + u_g + p_g)\underline{u}_t/\rho_0 > 1$  (i.e. thermo-kinetically unbound). The “w” or “wind” subscript is for the “entire wind” with the condition of  $b^2/\rho_0 < 1$  that includes all of the flow except the jet. The subscript is “in” (“out”) for the condition  $u_r < 0$  ( $u_r > 0$ ).

We also compute (as shown in Table 3) the number of grid cells that cover the disk half-angular thickness ( $\theta^d$ ) computed by Eq. (12) at the horizon ( $\theta_H^d$ ) and other radii  $r$  ( $\theta_{r/r_g}^d$ ). For comparison, we also compute the thermal half-angular thickness ( $\theta^t = \theta_\rho^t$ ).

Also computed are the disk-corona interface angular location at a given radius  $r$  (denoted  $\theta_{r/r_g}^{dc}$ ) defined by where  $\beta = 1$  and the corona-jet interface angular location at a given radii  $r$  (denoted  $\theta_{r/r_g}^j$ ) defined by where  $b^2/\rho_0 = 1$ . In practice, these interface locations are defined similarly to Eq. (12), except  $\theta_0 = \pi/2$  and weight  $w = u'(\rho_0 + u_g + p_g + b^2)$  are chosen with the following conditions. The disk-corona interface calculation uses the condition  $1/2 < \beta < 1$ , unless that condition is not met by any grid cells at that radius – in which case the condition  $1/10 < \beta < 1$  is used. The corona-jet interface calculation uses the condition  $1 < b^2/\rho_0 < 2$ , unless (very rarely) that condition is not met by any grid cells at that radius – in which case the condition  $30 > b^2/\rho_0 > 1$  is used.

### 3.5 Fluxes of Mass, Energy, and Angular Momentum

The rest-mass flux, specific energy flux, and specific angular momentum flux are respectively given by

$$\dot{M} = \left| \int \rho_0 u^r dA_{\theta\phi} \right|, \quad (14)$$

$$e \equiv \frac{\dot{E}}{[\dot{M}]_t} = -\frac{\int T_r^r dA_{\theta\phi}}{[\dot{M}]_t}, \quad (15)$$

$$j \equiv \frac{\dot{J}}{[\dot{M}]_t} = \frac{\int T_\phi^r dA_{\theta\phi}}{[\dot{M}]_t}, \quad (16)$$

and are computed in Tables 5–6.

The net flow efficiency is given by

$$\eta = \frac{\dot{E} - \dot{M}}{[\dot{M}]_t} = \frac{\dot{E}^{\text{EM}}(r) + \dot{E}^{\text{MAKE}}(r)}{[\dot{M}_H]_t}. \quad (17)$$

Positive values correspond to an extraction of positive energy from the system at some radius. These  $\eta$ 's are computed in Tables 5, 6.

The BH's dimensionless spin-up parameter is

$$s \equiv \frac{d(a/M)}{dt} \frac{M}{[\dot{M}]_t} = -j - 2 \frac{a}{M} (1 - \eta), \quad (18)$$

(computed in Table 7). All  $\theta$  and  $\phi$  angles are integrated over. The BH is in “spin equilibrium” for  $s = 0$  (Gammie et al. 2004).

### 3.6 Magnetic Flux

The radial magnetic flux vs.  $\theta$  at any radius is

$$\Psi_r(r, \theta) = \int dA_{\theta\phi} \underline{B}^r. \quad (19)$$

The signed value of the maximum absolute value over all  $\theta$  angles ( $\text{smax}_{\theta}$ ) of the magnetic flux is

$$\Psi_t(r) \equiv \text{smax}_{\theta} \Psi_r, \quad (20)$$

and  $\Psi_{\text{H}} \equiv \Psi_t(r = r_{\text{H}})$  is the horizon's magnetic flux. The half-hemisphere horizon flux is

$$\Psi_{\text{H}} \equiv \Psi_r(r = r_{\text{H}}), \quad (21)$$

as integrated from  $\theta = \pi/2$  to  $\pi$  (negative compared to the integral from  $\theta = 0$  to  $\pi/2$ ). The  $\theta$  magnetic flux vs. radius at angle  $\theta$  is

$$\Psi_{\theta}(r, \theta) = \int_{r_{\text{H}}}^r \sqrt{-g} d\underline{x}^{(1)} d\underline{x}^{(3)} \underline{B}^{x^{(2)}}, \quad (22)$$

where the vertical magnetic flux threading the equator is

$$\Psi_{\text{eq}}(r) \equiv \Psi_{\theta}(r, \theta = \pi/2). \quad (23)$$

The total magnetic flux along the equator is

$$\Psi(r) \equiv \Psi_{\text{H}} + \Psi_{\text{eq}}(r). \quad (24)$$

For all forms of  $\Psi$ , all  $\phi$ -angles are integrated over.

The magnetic flux can be normalized in various ways (as computed in Table 9). Normalization by the initial flux at  $r_0$  gives  $\Psi(r)/\Psi(r_0)$ . One type of field geometry we will use has multiple field loops of alternating polarity as a function of radius. So another normalization is by the initial  $i$ -th extrema vs. radius, which gives  $\Psi/\Psi_i$  that picks up the extrema in the magnetic flux over each field loop. Normalization by the initial value of an extrema gives  $\Psi/\Psi_i(t = 0)$ . We also need to form a measure that indicates how much flux is available to the BH. So we consider the normalization by the flux in the disk that is immediately available to the horizon of the same polarity. This measure is given by  $\Psi_{\text{H}}/\Psi_a$ , where  $\Psi_a$  is the value where  $\Psi(r)$  goes through its first extremum of the same sign of magnetic flux (i.e. out to the radius with the same polarity of dipolar-like field) as on the horizon. If the horizon value is itself an extremum, then  $\Psi_{\text{H}}/\Psi_a = 1$  implying that the region immediately beyond the horizon only has opposite polarity field.

The absolute magnetic flux ( $\Phi$ ) is computed similarly to  $\Psi$ , except one 1) inserts absolute values around the field (e.g.  $\underline{B}^r$  and  $\underline{B}^\theta$  in the integrals); 2) puts absolute values around the integral; and 3) divides by 2 so that a dipolar field has  $|\Psi_t| = \Phi$ . For example,  $\Phi_r(r, \theta) = (1/2) \left| \int dA_{\theta\phi} \underline{B}^r \right|$ . The quantity  $\Phi/\Psi_t$  (computed in Table 9, and which is the only flux ratio directly time-averaged as  $[\Phi/\Psi_t]_t$ ) is roughly the vector spherical harmonic multipole  $l$  of the  $\phi$ -component of the magnetic vector potential:

$$\underline{A}_\phi = \int_{\theta'=0}^{\theta} \sqrt{-g} \underline{B}^r d\theta' \quad (25)$$

as integrated over all  $\phi$ . For example, for  $l = \{1 \dots 8\}$  one gets  $|\Phi/\Psi_t| = 1, 2, 2.6, 3.5, 4, 5.6, 5.7$ , and 6.7.

The Gammie (1999) model normalization gives

$$\Upsilon \approx 0.7 \frac{\Phi_r}{\sqrt{[\dot{M}]_t}}, \quad (26)$$

which accounts for  $\Phi_r$  being in Heaviside-Lorentz units (Penna et al. 2010). Compared to Gaussian units version of  $\phi_{\text{H}} \equiv \Phi_{\text{H}}/\sqrt{\dot{M} r_g^2 c}$  defined in Tchekhovskoy et al. (2011),  $\Upsilon \approx 0.2 \phi_{\text{H}}$ .  $\Upsilon_{\text{H}}$  and  $\Upsilon_j$  are normalized by  $\dot{M}_{\text{H}}$ ,  $\Upsilon_{\text{in}}$  by  $\dot{M}_{\text{in}}$ , and  $\Upsilon_{\text{mw}}$  and  $\Upsilon_{\text{w}}$  respectively by  $\dot{M}_{\text{mw}}$  and  $\dot{M}_{\text{w}}$ .  $\Upsilon$  is computed in Table 9.

The field line rotation frequency with respect to the BH spin ( $z$ ) axis is computed various ways. We consider  $\Omega_{\text{F}}^a \equiv F_{tr}/F_{r\phi}$ ,  $\Omega_{\text{F}}^b \equiv F_{t\theta}/F_{\theta\phi}$ ,  $\Omega_{\text{F}}^c \equiv |\underline{v}^\phi| + \text{sign}[\underline{u}^r](v_p/B_p)|\underline{B}^\phi|$  with  $v_p = \sqrt{v_r^2 + v_\theta^2}$  and  $B_p = \sqrt{B_r^2 + B_\theta^2}$ , and

$$\Omega_{\text{F}} \equiv \Omega_{\text{F}}^d \equiv \underline{v}^\phi - \underline{B}^\phi \left( \frac{v_r B_r + v_\theta B_\theta}{B_r^2 + B_\theta^2} \right). \quad (27)$$

We also consider  $\Omega_{\text{F}}^e \equiv [F_{t\theta}]_t/[F_{\theta\phi}]_t$ . These  $\Omega_{\text{F}}$  are normalized by the BH rotation angular frequency  $\Omega_{\text{H}} = a/(2Mr_{\text{H}})$ .

### 3.7 Inflow Equilibrium and $\alpha$ Viscosity

Inflow equilibrium is defined as when the flow is in a complete quasi-steady-state and the accretion fluxes are constant (apart from noise) vs. radius and time. The inflow equilibrium timescale is

$$t_{\text{ie}} = N \int_{r_i}^{r_{\text{ie}}} dr \left( \frac{-1}{[\langle v_r \rangle_\rho]_t} \right), \quad (28)$$

for  $N$  inflow times from  $r = r_{ie}$  and  $r_i = 12r_g$  to focus on the more self-similar flow.  $t_{ie}$  is used in Table 10, where  $r_i^{\text{dcden}} = r_i$ ,  $r_f^{\text{dcden}} = r_{ie}$  with  $N = 1$ , and  $r_o^{\text{dcden}}$  uses  $r_{ie}$  with  $N = 3$ .

Viscous theory gives a GR  $\alpha$ -viscosity estimate for  $v_r$  of  $v_{\text{visc}} \sim -G\alpha(\theta^d)^2|v_{\text{rot}}|$  (Page & Thorne 1974; Penna et al. 2010), with GR correction  $G (\lesssim 1.5$  for  $r \gtrsim 58r_g$ ) and (not the lapse)

$$\begin{aligned} \alpha &= \alpha_{\text{PA}} + \alpha_{\text{EN}} + \alpha_{\text{M1}} + \alpha_{\text{M2}}, \\ \alpha_{\text{PA}} &\approx \frac{\rho_0 \delta u_r (\delta u_\phi \sqrt{g^{\phi\phi}})}{p_{\text{tot}}}, \\ \alpha_{\text{M2}} &\approx -\frac{b_r (b_\phi \sqrt{g^{\phi\phi}})}{p_{\text{tot}}}, \\ \alpha_{\text{mag}} &\approx -\frac{b_r (b_\phi \sqrt{g^{\phi\phi}})}{p_b}, \\ \alpha_{\text{eff}} &\equiv \frac{v_r}{v_{\text{visc}}/\alpha}, \end{aligned} \quad (29)$$

$\alpha_{\text{eff2}} \equiv \alpha_{\text{eff}}(|v_{\text{rot}}|/|v_K|)$ , and (small)  $\alpha_{\text{EN}} \approx (u_g + p_g)\delta u_r (\delta u_\phi \sqrt{g^{\phi\phi}})/p_{\text{tot}}$  and  $\alpha_{\text{M1}} \approx b^2 \delta u_r (\delta u_\phi \sqrt{g^{\phi\phi}})/p_{\text{tot}}$ . Here,  $\delta u$  is the deviation of the velocity from its average (taken over all  $\phi$  and over the time-averaging period). The  $\alpha$  (e.g. in Table 8) is averaged as follows. The numerator and denominator are separately volume averaged in  $\theta, \phi$  for each  $r$ . Weight  $w = 1$  with condition  $b^2/\rho_0 < 1$  gives  $\alpha_a$  for the disk+corona, while  $w = \rho$  gives  $\alpha_b$  for the heavy disk. Notice  $\alpha_{\text{M2}} = \alpha_{\text{mag}}/(1 + \beta_{\text{mag}})$  for some  $\beta$  denoted  $\beta_{\text{mag}}$ , and  $\sin(2\theta_b) = \alpha_{\text{mag}}$  for tilt angle  $\theta_b$  (Sorathia et al. 2011). These  $\alpha$ 's are accurate for  $|v| \ll c$  as true for  $r \gtrsim 2r_g$  in our models, while  $\alpha_{\text{eff}}$  is accurate far outside the inner-most stable circular orbit (ISCO).

### 3.8 Modes and Correlation Lengths

The flow structure is studied via the discrete Fourier transform of  $dq$  (related to quantity  $Q$ ) along  $x = r, \theta, \phi$  giving amplitude  $a_p$  for  $p = n, l, m$ , respectively. The averaged amplitude is

$$\langle |a_p| \rangle \equiv \langle |\mathcal{F}_p(dq)| \rangle \equiv \int_{\text{not } x} \left| \sum_{k=0}^{N-1} dq e^{-\frac{2\pi i p k}{N-1}} \right|, \quad (30)$$

computed at  $r = r_H, 4r_g, 8r_g, 30r_g$ . The  $x$  is one of  $r, \theta, \phi$  and “not  $x$ ” are others (e.g.  $\theta, \phi$  for  $x = r$ ). The  $dq$  is (generally) a function of  $x$  on a uniform grid indexed by  $k$  of  $N$  cells that span:  $\delta r$  equal to  $0.75r$  around  $r$  for  $x = r$ ,  $\pi$  for  $x = \theta$ , and  $2\pi$  for  $x = \phi$ . The  $N$  is chosen so all structure from the original grid is resolved, while the span covered allows many modes to be resolved.

For all  $x$ ,  $dq \equiv \sqrt{-g} dx^{(1)} dx^{(2)} dx^{(3)} \delta Q / q_N$ . For  $x = r, \theta$ , we let  $q_N = \int_{\text{not } x} \sqrt{-g} dx^{(1)} dx^{(2)} dx^{(3)} \langle [Q]_t \rangle$ ,  $\langle [Q]_t \rangle$  as the time- $\phi$  averaged  $Q$ , and  $\delta Q = Q - \langle [Q]_t \rangle$ . Using  $dq$  removes gradients with  $r, \theta$  so the Fourier transform acts on something closer to periodic with constant amplitude (see also Beckwith et al. 2011). For  $x = \phi$ , we let  $q_N = 1$  and  $\delta Q = Q$  because the equations of motion are  $\phi$ -ignorable. For  $x = \theta, \phi$ , the radial integral is computed within  $\pm 0.1r$ . For  $x = r, \theta$ , the  $\phi$  integral is over all  $2\pi$ . For  $x = r, \phi$ , the  $\theta$  integral is over all  $\pi$ . For all  $x$  cases, the  $\theta$  range of values uses the “fdc” or “jet” conditions (respectively called “Disk” and “Jet” in sections 5.7, 6.7, 6.10), where these conditional regions are defined via  $\phi$ -averaged quantities at each time. Notice we average the mode’s absolute amplitude, because the amplitude of  $\langle \delta Q \rangle$  de-resolves power (e.g.  $m = 1$  out of phase at different  $\theta$  gives  $\langle \delta Q \rangle \rightarrow 0$  and  $a_m \rightarrow 0$ ) and is found to underestimate small-scale structure.

We also compute the correlation length:  $\lambda_{x,\text{cor}} = x_{\text{cor}} - x_0$ , where  $x_0 = 0$  for  $x = \theta, \phi$  and  $x_0$  is the inner radius of the above

given radial span for  $x = r$ , where  $n_{\text{cor}} = \delta r / \lambda_{r,\text{cor}}$ ,  $l_{\text{cor}} = \pi / \lambda_{\theta,\text{cor}}$ , and  $m_{\text{cor}} = (2\pi) / \lambda_{\phi,\text{cor}}$ . The Wiener-Khinchin theorem for the auto-correlation gives

$$\exp(-1) = \frac{\mathcal{F}_{x=x_{\text{cor}}}^{-1}[\langle |a_{p>0}|^2 \rangle]}{\mathcal{F}_{x=x_0}^{-1}[\langle |a_{p>0}|^2 \rangle]}, \quad (31)$$

where  $\mathcal{F}^{-1}[\langle |a_{p>0}|^2 \rangle]$  is the inverse discrete Fourier transform of  $\langle |a_p|^2 \rangle$  but with  $\langle a_0 \rangle$  reset to 0 (i.e. mean value is excluded).

### 3.9 Suppression of the MRI

The MRI is a linear instability with fastest growing wavelength of

$$\lambda_{x,\text{MRI}} \approx 2\pi \frac{|v_{x,A}|}{|\Omega_{\text{rot}}|}, \quad (32)$$

for  $x = \theta, \phi$ , where  $|v_{x,A}| = \sqrt{b_x b^x} / \epsilon$  is the  $x$ -directed Alfvén speed,  $\epsilon \equiv b^2 + \rho_0 + u_g + p_g$ , and  $r\Omega_{\text{rot}} = v_{\text{rot}}$ .  $\lambda_{\text{MRI}}$  is accurate for  $\Omega_{\text{rot}} \propto r^{-5/2}$  to  $r^{-1}$ .  $\Omega_{\text{rot}}, v_A$  are separately angle-volume-averaged at each  $r, t$ .

The MRI suppression factor corresponds to the number of MRI wavelengths across the full disk:

$$S_{d,\text{MRI}} \equiv \frac{2r\theta^d}{\lambda_{\theta,\text{MRI}}}. \quad (33)$$

Wavelengths  $\lambda < 0.5\lambda_{\theta,\text{MRI}}$  are stable, so the linear MRI is suppressed for  $S_{d,\text{MRI}} < 1/2$  when no unstable wavelengths fit within the full disk (Balbus & Hawley 1998; Pessah & Psaltis 2005).  $S_{d,\text{MRI}}$  (or  $S_{d,\text{weak,MRI}}$ ) uses averaging weight  $w = (b^2\rho)^{1/2}$  (or  $w = \rho$ ), condition  $\beta > 1$ , and excludes regions where density floors are activated. Weight  $w = (b^2\rho)^{1/2}$  is preferred, because much mass flows in current sheets where the magnetic field vanishes and yet the MRI is irrelevant. When computing the averaged  $S_{d,\text{MRI}}$ ,  $v_A$  and  $|\Omega_{\text{rot}}|$  are separately  $\theta, \phi$ -volume-averaged within  $\pm 0.2r$  for each  $t, r$ . The averaged  $S_{d,\text{MRI}}$  is at most 30% smaller than  $S_{d,\text{weak,MRI}}$ .

$S_{d,t=0,\text{MRI},[i,o]}$  (in Table 1) gives  $S_{d,\text{MRI}}$  at  $t = 0$  at  $r = r_i = 30r_g$  and  $r = r_o = 50r_g$  averaged within  $\pm 0.2r$ , except models MB09D/Q use  $r_i = 10r_g$  and  $r_o = 15r_g$  due to their disk’s limited radial extent. Time-averages (see Table 8) are obtained for  $r = r_i^{\text{dcden}}$  and  $r = r_o^{\text{dcden}}$  (see Table 10) averaged within  $\pm 0.2r$ . Table 8 also gives  $r = rS_{d,\text{MRI}}=1/2$ , within which the linear MRI is suppressed.

## 4 PHYSICAL AND NUMERICAL MODELS

This section describes our models with parameters shown in Tables 1, 2. The model names are in the form AxByNz, where x is the approximate value of the BH spin, y identifies the field geometry (p=poloidal, f=flipping poloidal, t=toroidal), and z identifies the normalization of the magnetic field. For instance, our fiducial model A0.94BfN40 has a spinning BH ( $a/M = 0.9375$ ), a poloidal field that flips polarity with radius, and  $\beta_{\text{min}} \approx 40$  (i.e. smallest value of  $\beta$  is 40). The label  $c?$  (with number ?) is appended for convergence tests,  $r$  is appended to the model name if it is another realization of an identical model, and  $HR$  is appended if it is a high-resolution continuation of some model. 2D axisymmetric models are marked with \*. Models from McKinney & Blandford (2009) are denoted MB09D and MB09Q for their dipolar and large-scale quadrupolar models, respectively. The remaining TMN11 models are similar to Tchekhovskoy et al. (2011). Primary models (fiducial thick poloidal: A0.94BfN40, thick retrograde poloidal: A-0.94BfN40HR, thick toroidal: 0.94BtN10HR, thinner poloidal: A0.99N100) have bold font labels.

Table 2 gives the time-averaging period (from  $T_i^a$  to  $T_f^a$  in

$r_g/c$ ). Models have  $T_i = 0$ , except A0.94BtN10HR starts as a super-sampled A0.94BtN10 at  $T_i = 57400r_g/c$ , A-0.94BfN40HR starts as A0.94BfN40 at  $T_i = 7995r_g/c$  with  $a/M = -0.9375$ , and A0.99N100 doubles  $N_\phi$  (to shown  $N_\phi$ ) at  $t \approx 14675r_g/c$ . For A0.94BpN100,  $T_i^a, T_f^a = 14000, 27048$  and  $T_i^a, T_f^a = 8000, 13000$  give similar results (validating  $T_f^a = 13000$  for similar models).

#### 4.1 Physical Models

This study considers BH accretion disk systems. Our “thick disk” models have initial geometric half-angular thickness  $\theta^d \sim 0.6$ , a range of BH spins ( $a/M = -0.9375, -0.5, 0, 0.5, 0.9375$ ), a range of field geometries (constant polarity poloidally-dominated, flipping polarity poloidally-dominated, and toroidally-dominated), and a range of initial disk magnetic field strengths ( $\beta_{\min} = 10, 30, 40, 100$ ). Our “thinner disk” TNM11 models have initial  $\theta^d \sim 0.2$ ,  $a/M = -0.9, -0.5, -0.2, 0, 0.1, 0.2, 0.5, 0.9, 0.99$ , a poloidally-dominated field geometry, and  $\beta_{\min} = 25, 50, 100, 200$  for  $a/M = 0.9$ . MB09 models are like most prior MHD simulations with limited poloidal flux.

The initial mass for the thick disk models is an isentropic hydro-equilibrium torus (Fishbone & Moncrief 1976; Gammie et al. 2003) with inner edge at  $r_{\text{in}} = 10r_g$  and pressure maximum at  $r_{\text{max}} = 100r_g$ . The torus is marginally unbound by tens of percent, as similar to ADAFs that we want to model (Narayan & Yi 1995a). The magnetic field inserted (described later) makes negligible changes to the torus’ boundedness. Table 3 shows the disk’s geometric half-angular thickness ( $\theta^d$ ) at  $r_{\text{max}}$ . We set  $\rho_0 = \rho_{\text{max}} = 1$  at the maximum rest-mass density. To seed the MRI,  $u_g$  is perturbed by a factor  $1 + F_R(E - 0.5)$ , where  $F_R = 0.1$  and  $E$  is a random number from 0 to 1. The torus is surrounded by an atmosphere with  $\rho_0 = 10^{-4}(r/r_g)^{-2}$ ,  $u_g = 10^{-6}(r/r_g)^{-5/2}$ ,  $\tilde{u}^i = 0$ , and  $B^i = 0$ .

We consider an initial poloidal field geometry to seek poloidal magnetic flux saturation near the BH. Field polarity flips are inserted by modulating the poloidal polarity vs. radius in order to generate multiple loops of alternating polarity for studying magnetic field inversion/annihilation. For this poloidal field geometry, the  $\phi$ -component of the magnetic vector potential is

$$\begin{aligned} \underline{A}_\phi &\propto f_1 f_2, \\ f_1 &= |q|^p |r \sin(\theta)|^\nu, \\ q &= u_g/u_{g,\text{max}} - f_c, \\ f_2 &= \sin(\log(r/S)/T), \end{aligned} \quad (34)$$

where  $f_1$  has  $p = 1$  and  $\nu = 2$ ,  $q$  has  $f_c = 0.2$ ,  $u_{g,\text{max}}$  is the maximum  $u_g$ ,  $q = 0$  is set if  $q < 0$ , and  $f_2$  has  $S = 0.5r_{\text{in}}$  and  $T = 0.28$  for the flipping field and  $f_2 = 1$  for the non-flipping field.

We also consider an initial toroidal field geometry, as the limit of negligible coherent poloidal magnetic flux, where the  $\theta$ -component of the magnetic vector potential is

$$\underline{A}_\theta \propto r^2(u_g/u_{\text{max}} - f_c), \quad (35)$$

with  $f_c = 0.2$ . If  $\underline{A}_\theta < 0$ , then  $\underline{A}_\theta = 0$  is set. Then  $\sqrt{-g}\underline{B}^\phi = \underline{A}_{\theta,r}$  is computed. The random perturbations of  $u_g$  also lead to a small radial field via  $\sqrt{-g}\underline{B}^r = -\underline{A}_{\theta,\phi}$ , which corresponds to radial wiggles in the toroidal field. Within  $r \sim 100r_g$  there is about 10 times less energy in this radial field compared to the toroidal field. Very small truncation-level  $\underline{B}^\theta$  is also present.

Table 1 shows each model’s initial field, marked as “Poloidal” for the non-flipping poloidal field, “PoloidalFlip” for the flipping poloidal field, and “Toroidal” for the toroidal field. The models from McKinney & Blandford (2009) use the “PoloidalOld”

poloidal field geometry (i.e.  $\underline{A}_\phi \propto (\rho_0 - \rho_{\text{cut}})$  and, e.g.,  $\rho_{\text{cut}} \sim 0.25\rho_{\text{max}} = 0.25$ ) or use the “LSQuad” large-scale quadrupolar field geometry. The models marked as “Poloidal2” use the magnetic field geometry described in Tchekhovskoy et al. (2011).

The magnetic field strength is set via the plasma  $\beta = p_g/p_b \sim (2/\Gamma)(c_s/v_a)^2$  where  $v_a^2 = b^2/(\rho_0 + u_g + p_g + b^2)$  gives the Alfvén speed  $v_a$ . Our thick disk models have  $\beta_{\min}$ , the smallest value of  $\beta$  (within the resolved disk region, e.g.,  $r \sim 1000r_g \ll R_{\text{out}}$ ) of  $\beta_{\min} \approx 10$  to 200. An alternative measure is  $\beta_{\text{rat-of-maxes}} \equiv p_{g,\text{max}}/p_{b,\text{max}}$ , where  $p_{g,\text{max}}$  is the maximum thermal pressure on the domain and  $p_{b,\text{max}}$  is the maximum magnetic pressure on the domain. Another alternative is  $\beta_{\text{rat-of-avg}} \equiv p_{g,\text{avg}}/p_{b,\text{avg}} = \langle p_g \rangle / \langle p_b \rangle$ . These  $\beta$  (see Table 1) are computed with condition  $b^2/\rho_0 < 1$ . For poloidal field models, our choices for  $\beta$  ensure that  $S_{d,\text{MRI}} > 1$  so the MRI operates, while we push close to  $S_{d,\text{MRI}} \sim 1$  as reached even in toroidal field models.

#### 4.2 Numerical Models

The uniform spatial coordinates  $\underline{x}^{(i)}$  have resolution  $N_r \times N_\theta \times N_\phi$  active grid cells and 4 boundary cells for each of the 6 boundaries in 3D. The radial grid of  $N_r$  cells spans from  $R_{\text{in}}$  to  $R_{\text{out}}$  with mapping

$$r(\underline{x}^{(1)}) = R_0 + \exp f[\underline{x}^{(1)}] \quad (36)$$

where  $R_0 = 0$  is chosen in this paper. For  $\underline{x}^{(1)} < x_{\text{break}}$

$$f[\underline{x}^{(1)}] = n_0 \underline{x}^{(1)}, \quad (37)$$

where  $x_{\text{break}} = \log(r_{\text{break}} - R_0)/n_0$  (with  $n_0 = 1$ ), and otherwise

$$f[\underline{x}^{(1)}] = n_0 \underline{x}^{(1)} + c_2(\underline{x}^{(1)} - x_{\text{break}})^{n_2}, \quad (38)$$

where  $c_2 = 1$ , and  $n_2 = 10$ . The  $\underline{x}^{(1)}$  grid ranges from  $\underline{x}_s^{(1)} = (\log(R_{\text{in}} - R_0))/n_0$  to  $\underline{x}_f^{(1)} = (\log(R_{\text{out}} - R_0))/n_0$  if  $R_{\text{out}} < r_{\text{break}}$  and otherwise determined iteratively from  $R_{\text{out}} = r[\underline{x}_f^{(1)}]$ . The value of  $R_{\text{in}}$  is chosen so that there are 6 active grid cells inside the outer horizon, while  $R_{\text{in}}$  is outside the inner horizon. So the boundary cells only connect to stencils (each  $\pm 4$  cells) that are inside the horizon, which avoids causal connection between the inner boundary and the flow outside the horizon. For models where no persistent jet is launched, we set  $R_{\text{out}} = 10^3 r_g$  and  $r_{\text{break}} \gg R_{\text{out}}$ . For models where a jet is launched, we set  $R_{\text{out}} = 26000r_g$  and  $r_{\text{break}} = 5 \times 10^2 r_g$ . The radius  $r_{\text{break}}$  is where the grid changes from exponential to hyperexponential, which allows the grid to focus on the dynamics at small radii while avoiding numerical reflections off the outer grid. Radial boundaries use absorbing conditions.

The  $\theta$ -grid of  $N_\theta$  cells spans from 0 to  $\pi$  with mapping

$$\theta(\underline{x}^{(2)}) = \Theta_2 + W(\Theta_1 - \Theta_2) \quad (39)$$

where  $\underline{x}^{(2)}$  ranges from 0 to 1 (i.e. no polar cut-out ; but see Appendix A). The first grid mapping function is given by

$$\begin{aligned} \Theta_1 &= T_0 S_2 + T_2 S_0, \\ T_2 &= (\pi/2)(1 + \arctan(h_2(\underline{x}^{(m2)} - (1/2)))/\arctan(h_2/2)), \\ h_2 &= h_3 + ((r - r_{sj3})/r_{0j3})^{n_{j1}}, \\ T_0 &= \pi \underline{x}^{(2)} + ((1 - h_0)/2) \sin(2\pi \underline{x}^{(2)}), \\ h_0 &= 2 - Q_j(r/r_{1j})^{-n_{j2}((1/2)+(1/\pi)\arctan(r/r_{0j} - r_{sj}/r_{0j}))}, \\ S_2 &= (1/2) - (1/\pi) \arctan((r - r_s)/r_0), \\ S_0 &= (1/2) + (1/\pi) \arctan((r - r_s)/r_0), \end{aligned} \quad (40)$$

where  $r_s = 40$  and  $r_0 = 20$ . For  $h_2$ , we set  $h_3 = 0.3$ ,  $r_{0j3} = 20$ ,  $r_{sj3} = 0$ , and  $n_{j1} = 1$  so the jet is resolved with grid lines following  $\theta_j \propto r^{-n_{j1}}$ . For  $h_0$ , we set  $r_{1j} = 2.8$ ,  $n_{j2} = 1$ ,  $r_{0j} = 15$ ,  $r_{sj} = 40$ , and

**Table 1.** Physical Model Parameters

ModelName	$a/M$	FieldType	$\beta_{\min}$	$\beta_{\text{rat-of-avg}}$	$\beta_{\text{rat-of-max}}$	$\theta_{r_{\max}}^d$	$\theta_{r_{\max}}^t$	$S_{d,t=0,\text{MRI},\{i,o\}}$	$T_f$
<b>A0.94BfN40</b>	0.9375	PoloidalFlip	40	230	40	0.61	1.1	1.6, 2.6	26548
A0.94BfN100c1	0.9375	PoloidalFlip	120	490	130	0.61	1.1	2.4, 4.4	13000
A0.94BfN100c2	0.9375	PoloidalFlip	130	480	140	0.61	1.1	2.3, 4.4	13000
A0.94BfN100c3	0.9375	PoloidalFlip	120	490	130	0.61	1.1	2.3, 4.5	13000
A0.94BfN100c4	0.9375	PoloidalFlip	130	490	130	0.61	1.1	2.3, 4.4	13000
A0.94BfN40c5*	0.9375	PoloidalFlip	40	230	43	0.61	1.1	1.6, 2.6	13000
<b>A-0.94BfN40HR</b>	-0.9375	PoloidalFlip	40	230	40	0.61	1.1	1.6, 2.6	18416
A-0.94BfN30	-0.9375	PoloidalFlip	30	120	31	0.6	1.1	1.2, 2.2	13000
A-0.5BfN30	-0.5	PoloidalFlip	34	130	35	0.61	1.1	1.3, 2.2	13000
A0.0BfN10	0	PoloidalFlip	10	42	11	0.61	1.1	0.68, 1.2	13832
A0.5BfN30	0.5	PoloidalFlip	33	120	36	0.61	1.1	1.3, 2.2	13000
A0.94BfN30	0.9375	PoloidalFlip	30	120	32	0.61	1.1	1.2, 2.2	13000
A0.94BfN30r	0.9375	PoloidalFlip	32	120	33	0.61	1.1	1.2, 2.2	13000
A0.94BpN100	0.9375	Poloidal	93	240	110	0.61	1.1	1.8, 1.8	27048
A-0.94BtN10	-0.9375	Toroidal	10	1600	25	0.6	1.1	370, 350	93944
A-0.5BtN10	-0.5	Toroidal	10	980	17	0.61	1.1	300, 260	129392
A0.0BtN10	0	Toroidal	10	1200	28	0.61	1.1	320, 300	96796
A0.5BtN10	0.5	Toroidal	10	1000	17	0.61	1.1	290, 250	135572
A0.94BtN10	0.9375	Toroidal	10	1300	20	0.61	1.1	300, 290	93648
<b>A0.94BtN10HR</b>	0.9375	Toroidal	10	1300	20	0.61	1.1	300, 290	80184
MB09D	0.92	PoloidalOld	14	530	100	0.18	0.24	3.4, 16	5662
MB09Q	0.9375	LSQuad	0.0067	540	140	0.19	0.25	41, 60	5688
A-0.9N100	-0.9	Poloidal2	100	150	220	0.21	0.27	3.6, 4.4	20060
A-0.5N100	-0.5	Poloidal2	100	140	210	0.22	0.28	3.5, 4.3	16335
A-0.2N100	-0.2	Poloidal2	100	140	200	0.22	0.29	3.5, 4.3	15175
A0.0N100	0	Poloidal2	100	140	210	0.22	0.29	3.6, 4.3	18585
A0.1N100	0.1	Poloidal2	100	150	210	0.22	0.29	3.6, 4.4	20000
A0.2N100	0.2	Poloidal2	100	140	210	0.23	0.29	3.6, 4.3	19350
A0.5N100	0.5	Poloidal2	100	150	210	0.23	0.29	3.6, 4.4	19540
A0.9N25	0.9	Poloidal2	25	36	51	0.23	0.3	1.8, 2.2	17350
A0.9N50	0.9	Poloidal2	50	72	100	0.23	0.3	2.5, 3.1	14385
A0.9N100	0.9	Poloidal2	100	140	210	0.23	0.3	3.6, 4.4	19895
A0.9N200	0.9	Poloidal2	200	290	420	0.23	0.3	5.1, 6.2	28620
<b>A0.99N100</b>	0.99	Poloidal2	100	160	230	0.24	0.3	3.7, 4.6	31400

$Q_j = 1.3$ . We set  $\underline{x}^{(m2)} = \underline{x}^{(2)}$  unless  $\underline{x}^{(2)} > 1$  then  $\underline{x}^{(m2)} = 2 - \underline{x}^{(2)}$  and unless  $\underline{x}^{(2)} < 0$  then  $\underline{x}^{(m2)} = -\underline{x}^{(2)}$ .  $\Theta_1$  focuses on the disk at small radii and the jet at large radii. The second mapping function is

$$\Theta_2 = (\pi/2)(h_\theta(2\underline{x}^{(2)} - 1) + (1 - h_\theta)(2\underline{x}^{(2)} - 1)^{n_\theta} + 1), \quad (41)$$

where  $n_\theta = 5$  and  $h_\theta = 0.15$ .  $\Theta_2$  focuses on the thin inflow near the horizon in poloidal field models, while it also avoids small  $\phi$  polar cells that would limit the time step. The interpolation factor is

$$W = (1/2) + (1/\pi)(\arctan((r - r_{sj2})/r_{0j2})), \quad (42)$$

where  $r_{sj2} = 5$  and  $r_{0j2} = 2$ . The polar axis boundary condition is transmissive as described in Appendix A.

The  $\phi$ -grid of  $N_\phi$  cells spans from 0 to  $2\pi$  with mapping  $\phi(\underline{x}^{(3)}) = 2\pi\underline{x}^{(3)}$ . Many of our simulations have  $\underline{x}^{(3)}$  vary from 0 to 1 such that  $\Delta\phi = 2\pi$ . This is a fully 3D (no assumed symmetries) domain. Periodic boundary conditions are used in the  $\phi$ -direction. Our TNM11 type models use various  $\Delta\phi$ , and the spatial integrals are renormalized to account for the full  $2\pi$  range in  $\phi$ .

Table 2 marks the grid as “Exp” if exponential, “HypExp”

if hyperexponential, “ExpOld” for MB09’s exponential grid, and “TNM11” for TNM11’s hyperexponential grid.

We choose a resolution  $N_r \times N_\theta \times N_\phi$  that has a grid aspect ratio of 1:1:1 for most of the inner-radial domain. This allows the  $\phi$  dimension to be treated equally to the  $r - \theta$  dimensions. The aspect ratio (as volume-averaged within  $|\theta - \pi/2| \leq [\theta^d]_r$ ) is given as  $A_r$  in Table 2, where  $r_H$  is the horizon (focusing on the geometrically thinning disk),  $r_i = 20r_g$  (but applies for  $50r_g \gtrsim r \gtrsim 5r_g$  such that  $A$  is uniform for much of the flow), and  $r_o = 100r_g$  (showing the aspect ratio changes at large radii due to focusing on the jet). The MB09D/Q models use  $r_i = 10r_g$  and  $r_o = 20r_g$ .

The MRI is resolved for grid cells per wavelength (Eq. (32)),

$$Q_{x,\text{MRI}} \equiv \frac{\lambda_{x,\text{MRI}}}{\Delta_x}, \quad (43)$$

of  $Q_{x,\text{MRI}} \gtrsim 6$ , for  $x = \theta, \phi$ , where  $\Delta_r \approx d\underline{x}^{(1)}(dr/d\underline{x}^{(1)})$ ,  $\Delta_\theta \approx rd\underline{x}^{(2)}(d\theta/d\underline{x}^{(2)})$ , and  $\Delta_\phi \approx r \sin \theta d\underline{x}^{(3)}(d\phi/d\underline{x}^{(3)})$ . Volume-averaging is done as with  $S_{d,\text{MRI}}$ , except  $v_{x,A}/\Delta_x$  and  $|\Omega_{\text{rot}}|$  are separately  $\theta, \phi$ -volume-averaged before forming  $Q_{x,\text{MRI}}$ . Averaged  $Q_{\theta,\text{MRI}}, Q_{\phi,\text{MRI}}$  are typically 30% larger than  $Q_{\theta,\text{weak,MRI}}, Q_{\phi,\text{weak,MRI}}$  for toroidal



**Table 2.** Numerical Model Parameters

ModelName	GridType	$N_r$	$N_\theta$	$N_\phi$	$R_{\text{in}}/r_H$	$R_{\text{out}}$	$\Delta\phi$	$A_{rH}$	$A_{r_i}$	$A_{r_o}$	$Q_{\theta,\text{MRI}} _{t=0, [i,o]}$	$T_i^a - T_f^a$
<b>A0.94BfN40</b>	HypExp	272	128	256	0.855	26000	$2\pi$	4.6:1:4.3	1.1:1.1:1	1.2:2.1:1	17, 11	8000–17000
A0.94BfN100c1	HypExp	136	64	128	0.727	26000	$2\pi$	4.6:1:4.2	1.2:1.1:1	1.2:2.1:1	5.6, 3.4	8000–13000
A0.94BfN100c2	HypExp	136	64	64	0.727	26000	$2\pi$	4.7:1:8.5	1:1:1.8	1:1.8:1.7	5.8, 3.4	8000–12000
A0.94BfN100c3	HypExp	136	64	32	0.727	26000	$2\pi$	4.6:1:17	1:1:3.6	1:1.8:3.4	5.6, 3.4	8000–13000
A0.94BfN100c4	HypExp	136	64	16	0.727	26000	$2\pi$	4.5:1:33	1:1:7.2	1:1.8:6.7	5.7, 3.4	9000–13000
A0.94BfN40c5*	HypExp	272	128	1	0.855	26000	$2\pi$	4.7:1:1100	1:1:230	1:1.8:220	16, 11	8000–13000
<b>A-0.94BfN40HR</b>	HypExp	272	128	256	0.855	26000	$2\pi$	4.6:1:4.3	1.1:1.1:1	1.2:2.1:1	17, 11	10000–15000
A-0.94BfN30	HypExp	136	64	128	0.727	26000	$2\pi$	4.4:1:4	1.2:1.1:1	1.2:2.1:1	11, 6.5	8000–13000
A-0.5BfN30	HypExp	136	64	128	0.735	26000	$2\pi$	4.2:1:4	1.1:1.1:1	1.1:2.1:1	9.6, 6.7	8000–13000
A0.0BfN10	Exp	128	64	128	0.808	1000	$2\pi$	2.2:1:2	1.1:1.1:1	1.1:2.2:1	19, 12	8000–13832
A0.5BfN30	HypExp	136	64	128	0.735	26000	$2\pi$	4.2:1:4	1.1:1.1:1	1.1:2.1:1	10, 7	8000–13000
A0.94BfN30	HypExp	136	64	128	0.727	26000	$2\pi$	4.6:1:4.2	1.2:1.1:1	1.2:2.1:1	11, 6.8	8000–13000
A0.94BfN30r	HypExp	136	64	128	0.727	26000	$2\pi$	4.6:1:4.2	1.2:1.1:1	1.2:2.1:1	11, 6.8	8000–13000
A0.94BpN100	HypExp	136	64	128	0.727	26000	$2\pi$	4.5:1:4.1	1.2:1.1:1	1.2:2.1:1	7.5, 8.4	14000–27048
A-0.94BtN10	Exp	128	64	128	0.797	1000	$2\pi$	2.2:1:2	1.2:1.1:1	1.2:2.1:1	< 1	58000–93944
A-0.5BtN10	Exp	128	64	128	0.806	1000	$2\pi$	2:1:1.9	1.1:1.1:1	1.1:2.1:1	< 1	80000–129392
A0.0BtN10	Exp	128	64	128	0.808	1000	$2\pi$	2:1:1.9	1.1:1.2:1	1.1:2.2:1	< 1	58000–96796
A0.5BtN10	Exp	128	64	128	0.806	1000	$2\pi$	2:1:1.9	1.1:1.1:1	1.1:2.1:1	< 1	80000–135572
A0.94BtN10	Exp	128	64	128	0.797	1000	$2\pi$	2.4:1:2.1	1.2:1.1:1	1.2:2.1:1	< 1	58000–93648
<b>A0.94BtN10HR</b>	Exp	256	128	256	0.894	1000	$2\pi$	2.2:1:2	1.2:1.1:1	1.2:2.1:1	< 1	58000–80184
MB09D	ExpOld	256	128	32	0.79	1000	$2\pi$	1.6:1:12	1.4:1:11	1.4:1:10	4.7, 1.3	2000–3000
MB09Q	ExpOld	128	128	32	0.816	40	$2\pi$	1.6:1:11	1.5:1:10	1.4:1:9.7	< 1	1500–5688
A-0.9N100	TNM11	288	128	64	0.7	100000	$2\pi$	2.3:1:7.9	2:1:6.8	1.6:1:5.4	7, 7.2	11000–20060
A-0.5N100	TNM11	288	128	32	0.81	100000	$\pi$	1.6:1:8.1	1.4:1:6.8	1.1:1:5.3	7.4, 7.5	11000–16335
A-0.2N100	TNM11	288	128	32	0.81	100000	$\pi$	1.6:1:8.2	1.4:1:6.9	1.1:1:5.2	7.6, 7.5	11000–15175
A0.0N100	TNM11	288	128	32	0.81	100000	$\pi$	1.6:1:8	1.4:1:6.8	1.1:1:5.2	7.6, 7.6	11000–18585
A0.1N100	TNM11	288	128	32	0.81	100000	$\pi$	1.6:1:8	1.4:1:6.8	1.1:1:5.2	7.5, 7.4	11000–20000
A0.2N100	TNM11	288	128	32	0.81	100000	$\pi$	1.6:1:8.2	1.4:1:6.8	1.1:1:5.2	7.7, 7.6	11000–19350
A0.5N100	TNM11	288	128	32	0.81	100000	$\pi$	1.6:1:8.1	1.4:1:6.9	1.1:1:5.2	7.7, 7.6	11000–19540
A0.9N25	TNM11	288	128	32	0.8	100000	$\pi$	1.7:1:8.2	1.4:1:6.7	1.2:1:5.3	16, 15	11000–17350
A0.9N50	TNM11	288	128	32	0.8	100000	$\pi$	1.7:1:8.2	1.5:1:6.8	1.2:1:5.3	11, 11	11000–14385
A0.9N100	TNM11	288	128	64	0.8	100000	$2\pi$	1.7:1:8.2	1.5:1:6.8	1.2:1:5.3	7.9, 7.7	11000–19895
A0.9N200	TNM11	288	128	32	0.8	100000	$\pi$	1.7:1:8.2	1.5:1:6.8	1.2:1:5.4	5.5, 5.4	16000–28620
<b>A0.99N100</b>	TNM11	288	128	128	0.83	100000	$2\pi$	1.8:1:4	2:1:3.3	1.7:1:2.7	7.5, 7.3	15000–31400

field and MB09 models. The  $t = 0$  values (see Table 1) and time-averaged values (see Table 8) are measured at same radii as  $S_{d,\text{MRI}}$ .

Turbulence is resolved for grid cells per correlation length (Eq. (31)),

$$Q_{p,\text{cor}} \equiv \frac{\lambda_{x,\text{cor}}}{\Delta_x}, \quad (44)$$

of  $Q_{p,\text{cor}} \geq 6$ , for  $x = r, \theta, \phi$  and  $p = n, l, m$ , respectively. Otherwise, modes are numerically damped on a dynamical timescale (even  $Q = 5$  would not indicate the mode is marginally resolved, because numerical noise can keep  $Q \approx 5$  at increasing resolution until finally the mode is actually resolved – finally leading to an increasing  $Q \geq 6$  with increasing resolution; as seen by Shiokawa et al. 2012). Reported  $Q_{p,\text{cor}}$  take  $1/\Delta_x$  as the number of grid cells covering the span of  $\lambda_{x,\text{cor}}$  as centered on: middle of  $x^{(1)}$  within the used radial span for  $x = r$ ,  $\theta = \pi/2$  for  $x = \theta$  for the “Disk” and  $\theta = 0$  for  $x = \theta$  for the “Jet”, and anywhere for  $x = \phi$ . For  $\Delta\phi < 2\pi$ ,  $Q_{\phi,\text{MRI}}, Q_{m,\text{cor}} \ll N_\phi$  is required to avoid truncating the mode (as happens in model A0.9N25).

## 5 FIDUCIAL THICK DISK MODEL

Our fiducial model, A0.94BfN40, consists of an initially weakly magnetized thick accretion disk around a rotating ( $a/M = 0.9375$ ) BH. The initial magnetic field consists of field loops that alternate polarity with radius (the “flipping” field geometry). Model parameters given in Table 1 and Table 2.

### 5.1 Initial and Evolved Disk Structure

Figure 1 and Figure 2 show color plots of  $b^2$  and field line contours (contours of  $\underline{A}_\phi$  integrated over  $\phi$ , so is axially symmetric) for the initial and quasi-steady-state evolved solution, respectively. The initial solution consists of a radially extended thick torus within which several weak field loops (of alternating poloidal polarity) are embedded. The disk is geometrically thick with  $\theta^d \sim 1$  and also quite thermally thick with  $c_s/v_{\text{rot}} \gtrsim 1$  and  $c_s/v_K \gtrsim 1$  through-out the solution both initially and at late times.

The evolved solution, shown in Figure 2, shows that the first two field loops have been completely accreted or ejected. During

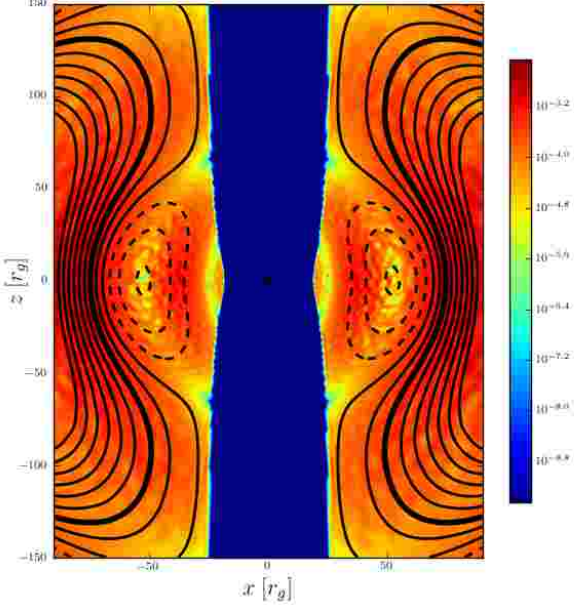


**Figure 1.** The fiducial model's initial ( $t = 0$ ) state consists of a weakly magnetized geometrically thick torus around a spinning ( $a/M = 0.9375$ ) BH.  $b^2$  is shown as color with legend. Black lines show  $\Delta_\phi$  (integrated over all  $\phi$ ). The inner-most-radial field loop is small and shows up as a high magnetic energy density with no field lines shown, the next field lines (black dashed lines) show the 2nd field loop, and the next field lines (black solid lines) show the 3rd field loop. The thickest black solid line is the same field line in Figure 2 that tracks the outer-most-angular part of the BH-driven jet.

accretion of the 3rd field loop, the magnetic flux reaches a maximum saturated value over a long period of inflow equilibrium.

Figure 3 shows an instantaneous meridional snapshot of the flow-field, which shows significant circulation. The field lines threading the BH are a dipolar split-monopolar magnetosphere.

## 5.2 Overall Time Dependence

Figure 4 shows a typical snapshot for the rest-mass density, field lines, and fluxes ( $\dot{M}$ ,  $\Upsilon$ , and  $\eta$ ) on the BH, through  $r = 50r_g$  in the jet, and at  $r = 50r_g$  in the magnetized wind.

The flow consists of a magnetized polar jet and a turbulent equatorial disk inflow. Near the BH, the rest-mass density in the inflow rises substantially due to vertical compression by the accumulated polar magnetic flux that surrounds the BH. The large-scale polar magnetic flux forms a semi-permeable magnetic barrier to the massive inflow, which is forced to undergo non-axisymmetric accretion through magnetic Rayleigh-Taylor instabilities.

The BH's magnetic flux dominates the mass influx with  $\Upsilon_H \approx 17$  during the quasi-steady-state period. Any additional magnetic flux that temporarily accretes onto the hole is ejected in magnetic Rayleigh-Taylor modes that push the flux back into the disk. This suggests that the magnetic flux near the BH has reached a maximum saturation point via some force balance condition. Because  $\Upsilon \gg 1$ , one expects the BZ effect to be activated, and indeed the energy extraction efficiency is high at  $\eta \sim 200\%$ . Most of the energy extracted from the BH reaches the jet at large radii (i.e.  $\eta_H \sim \eta_j$ ). The shown temporal behavior tracks the fact that  $\eta \propto \Upsilon^2$ . At the latest times the efficiency drops as the magnetic flux (from the 3rd field loop) begins to be destroyed by an incoming polarity field reversal (outer part of 3rd field loop and inner part of 4th field loop).

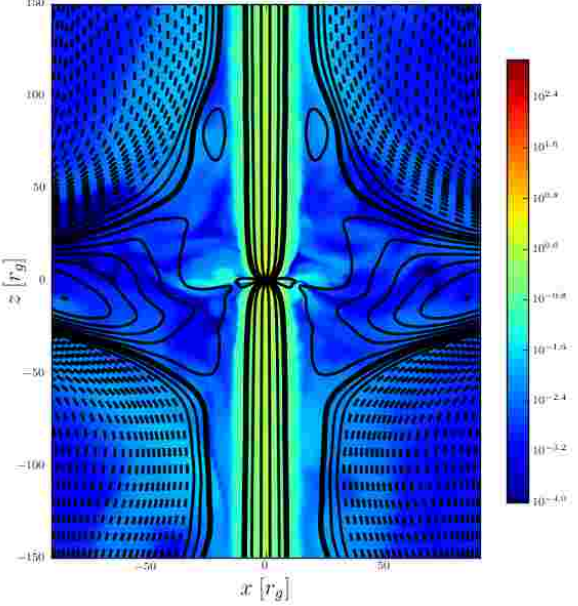


**Figure 2.** The evolved ( $t \approx 10412r_g/c$ ) state of the fiducial model (otherwise similar to Figure 1) consists of strongly magnetized gas near the BH that launches a jet that is visible as the vertical beam of large electromagnetic energy density. The jet is nearly cylindrical at small radii due to the pressure support from the thick accretion flow. All field lines in the 1st and 2nd field loops (shown in Figure 1) have been accreted or ejected in an out-flow. The 3rd (solid black lines) and 4th (dashed black lines) evolved field loops are shown, where the thickest solid black line traces the field line that connects to the outer angular part of the jet from the BH.

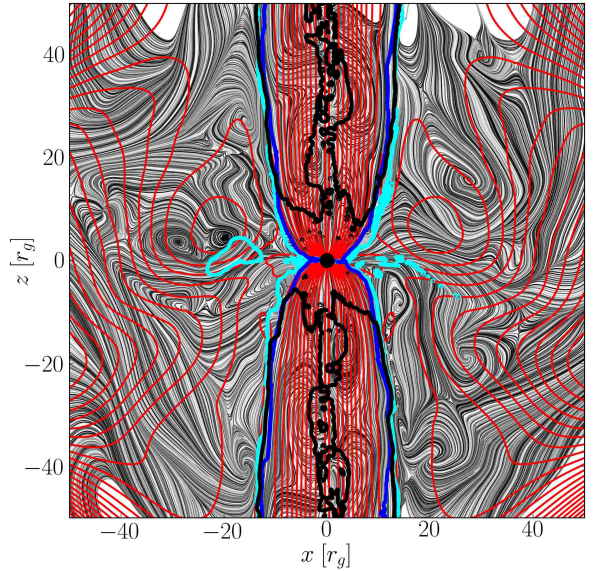


**Figure 3.** The evolved ( $t \approx 10412r_g/c$ ) state of the fiducial model showing velocity flow lines (traces of  $v_i$  shown as grayscale) and field lines ( $\Delta_\phi$  integrated over all  $\phi$ , shown as red lines). Also shown are contour lines, where  $-u_t = 1$  (most particles are unbound in the jet and in the wind at larger radii) is a thick black line,  $\beta = 2$  (beyond where corona and jet exist) is a thick cyan line, and  $b^2/\rho_0 = 1$  (beyond where the relativistic jet exists) is a thick blue line. The accretion flow is turbulent with circulating eddies.

The obvious complete polarity reversal (destruction of inner part of 2nd field loop by outer 2nd and inner 3rd) occurs at  $t \sim 2700r_g/c$  when  $\dot{M}$  doubles. At  $t \sim 7000r_g/c$ , magnetic flux is ejected in a large magnetic Rayleigh-Taylor disruption allowing  $\dot{M}$  to double.

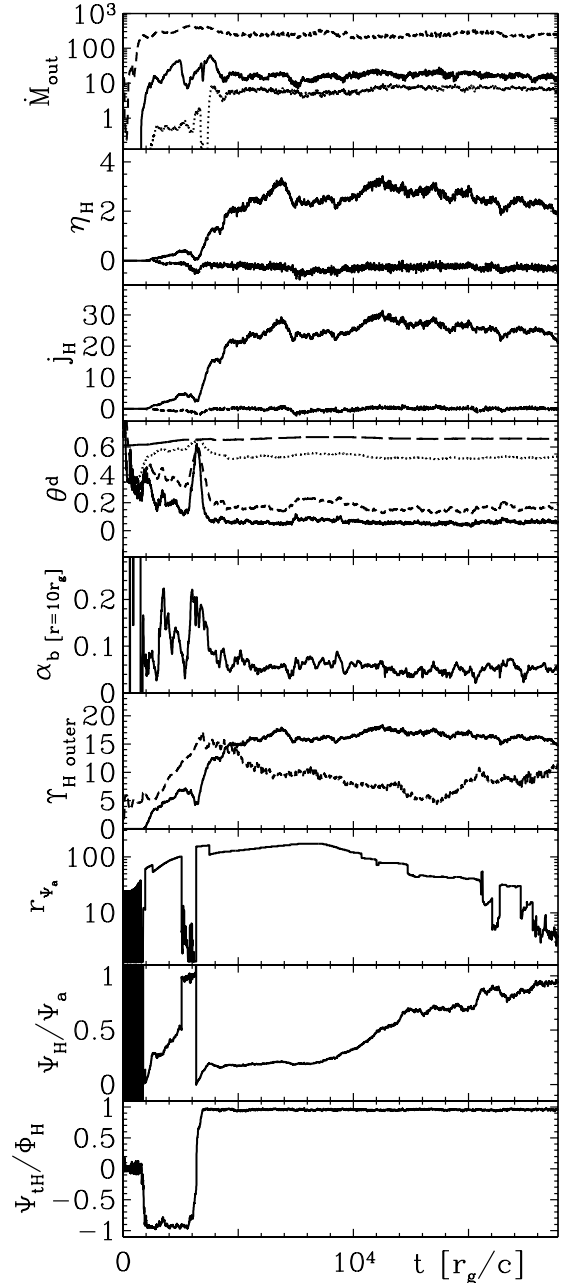
Figure 5 shows various quantities vs. time. All quantities are in a quasi-steady-state for  $t \gtrsim 8000r_g/c$  far after the last field polarity inversion at  $t \sim 2700r_g/c$  and after magnetic flux has accumulated near the BH. The mass ejected in the circulating wind ( $\dot{M}_{w,o}$ , seen as eddies in Fig. 3) dominates the magnetized wind ( $\dot{M}_{mw,o}$ ) and jet ( $\dot{M}_j$ ) at large radii ( $r_o = 50r_g$  here); see §3.4 for definitions of various outflow components. The EM term dominates the MAKE term in  $\eta_H$  and  $j_H$ , and the flow has a high efficiency of  $\eta_H \sim 200\%$ . The MAKE term is composed of a particle term (i.e.  $\eta^{\text{PAKE}} = 1 + \frac{u_r}{c}$ ) and an enthalpy term (i.e.  $\eta^{\text{EN}} = \frac{u_r(u_g + p_g)}{\rho_0}$ ). We find that  $\eta^{\text{MAKE}} \sim -30\%$  as composed of  $\eta^{\text{PAKE}} \sim 63\%$  and  $\eta^{\text{EN}} \sim -93\%$  ( $\eta^{\text{MAKE}} \approx -26\%$  in the initial torus, so  $\eta^{\text{EN}} \sim -67\%$  can be chosen for marginally bound inflow). So the inflow is bound as particles but thermo-kinetically unbound due to high enthalpy.

Accumulation of magnetic flux near the BH leads to geometric compression of the inflow as it approaches the horizon. The geometric thickness drops before the field inversion at  $t \sim 2700r_g/c$  as magnetic flux accumulates and compresses the disk inflow. However, during the field inversion, the geometric thickness restores to the prior geometric thickness ( $\theta^d \approx 0.7$ ) at all radii, which indicates that the field (lost during the field annihilation) is responsible for the thinning of the dense part of the disk. After the field polarity inversion, the magnetic flux re-accumulates near the BH, which leads again to the vertical compression of the disk flow. The  $\alpha$ -viscosity parameter holds steady at about  $\alpha_b \sim 0.05$ .  $\Upsilon$  in the pure inflow ( $u_r < 0$  only) available at large radii (here  $r = 50r_g$ , giving  $\Upsilon_{\text{outer}}$  in the plot) is large (the BH and “outer” values are similar for this chosen “outer” radius).

The value of  $r_{\Psi_a}$  shows the radius out to which the magnetic polarity is the same as on the horizon. As expected,  $r_{\Psi_a}$  drops to the horizon during the field inversion (destruction of inner part of 2nd field loop) at  $t \sim 2700r_g/c$ . It also gradually drops as the next polarity inversion (outer part of 3rd field loop) eats away at the magnetic flux outside the BH. The process of field inversion is also evident by looking at  $\Psi_H(t)/\Psi_a(t)$  (i.e. ratio of time-dependent fluxes) corresponding to [the flux on the hole] per unit [flux on the hole plus available of the same polarity just beyond the hole].  $\Psi_H(t)/\Psi_a(t) \sim 1$  is reached during the field polarity inversion, and at late times  $\Psi_H(t)/\Psi_a(t) \sim 1$  is approached. However, while  $\Upsilon$  holds steady, the value of  $|\Psi_H(t)/\Psi_a(t)| \ll 1$ , which indicates that much more same-polarity flux is available. This shows that the saturated value of  $\Upsilon$  (and so  $\eta$ ) is controlled by some force balance condition and not simply limited by initial conditions. Finally,  $|\Psi_H(t)/\Phi_H(t)| \sim 1$  shows that the horizon’s field is dipolar ( $l \approx 1$ ).

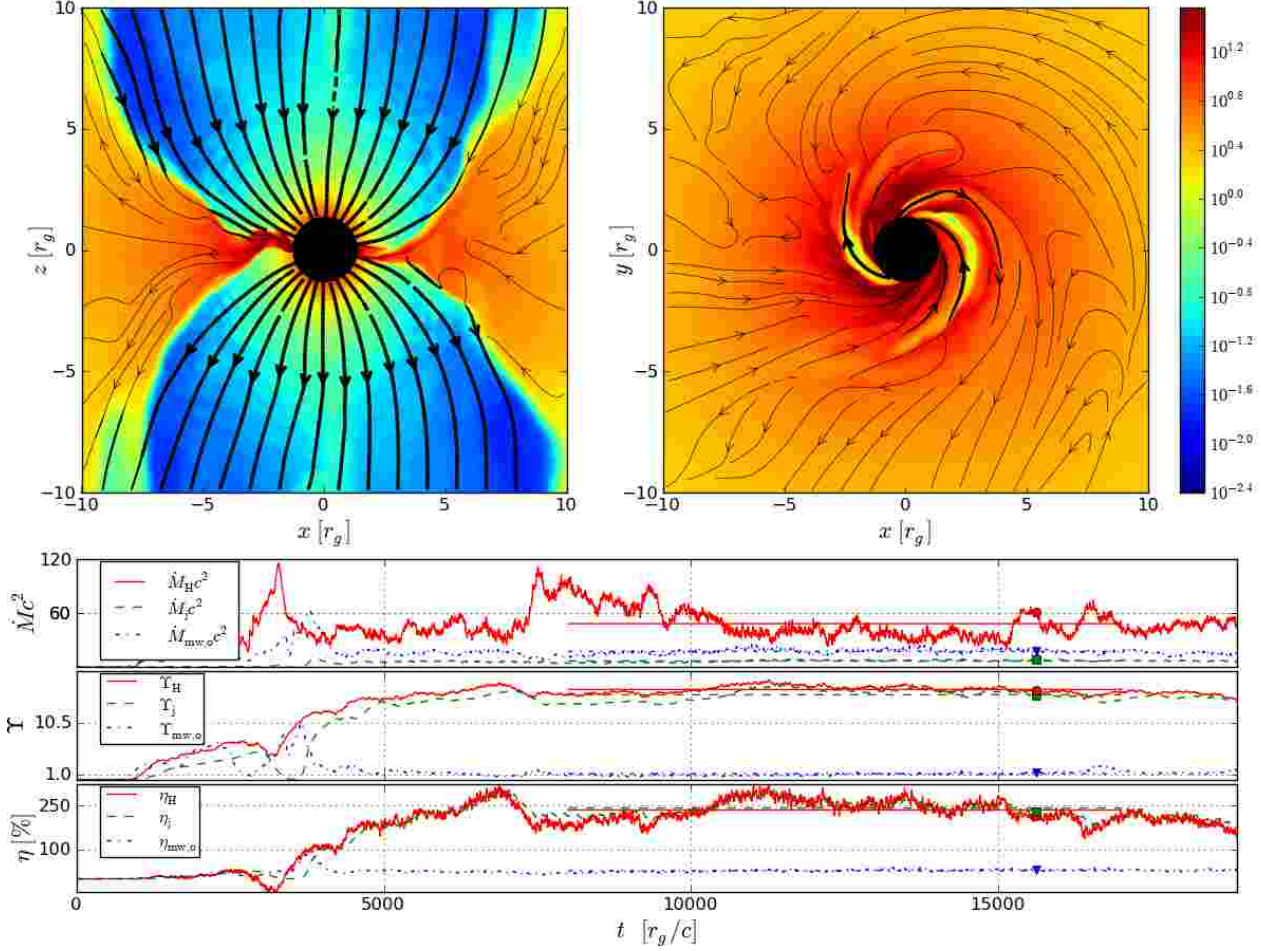
### 5.3 Time-Averaged Poloidal ( $r - \theta$ ) Dependence

Figure 6 shows the time-averaged flow-field and contours for other conditions. The figure is comparable to the snapshot shown in Figure 3. The jet region contains significant magnetic flux and same-signed polarity field exists near the BH ready to be accreted. In the quasi-stationary state, the BH’s magnetic flux oscillates around its saturated magnitude, whose time-averaged value is determined by some force balance condition as managed by non-axisymmetric Rayleigh-Taylor instabilities.



**Figure 5.** Quantities vs. time. Top Panel:  $\dot{M}_{\text{out}}$  for magnetized wind ( $\dot{M}_{mw,o}$ , solid line, and mostly middle line), entire wind ( $\dot{M}_{w,o}$ , short-dashed line, and upper-most line), and jet ( $\dot{M}_j$ , dotted line, and lowest line). Next Panel: Efficiency ( $\eta_H$ ) for EM (solid line, upper line) and MAKE (short-dashed line, lower line) terms. Next Panel: Specific angular momentum ( $j_H$ ) for EM (solid line, upper line) and MAKE (short-dashed line, lower line) terms. Next Panel:  $\theta^d$  at  $r = \{r_H/r_g, 5, 20, 100\}r_g$  with, respectively, lines: {solid, short-dashed, dotted, long dashed} corresponding to the lowest to upper-most lines. Next panel:  $\alpha_b$  at  $r = 10r_g$ . Next Panel:  $\Upsilon$  on the horizon (solid line, mostly upper line) and in the disk at  $r = 50r_g$  for only the ingoing flow (short-dashed line, mostly lower line). Next Panel:  $r_{\Psi_a}$  for the radius out to where there is the same magnetic polarity as on the hole (solid line). Next panel: Magnetic flux on the BH per unit flux available in the flow with the same polarity:  $\Psi_H(t)/\Psi_a(t)$ . Bottom panel:  $\Psi_H(t)/\Phi_H(t) \sim 1/l$ , for  $l$  mode of vector spherical harmonic multipole expansion of  $\underline{A}_\phi$ . In summary, the flow has reached a quasi-steady-state at late times. The magnetic flux on the horizon has saturated to a large value leading to a high efficiency for energy and angular momentum extraction from the BH.





**Figure 4.** Evolved snapshot (see Supporting Information for the movie) of the fiducial model at  $t \approx 15612 r_g/c$  showing log of rest-mass density in color (see legend on right) in both the  $z-x$  plane at  $y=0$  (top-left panel) and  $y-x$  plane at  $z=0$  (top-right panel). Black lines trace field lines, where thicker black lines show where field is lightly mass-loaded. The bottom panel has 3 subpanels. The top subpanel shows  $\dot{M}$  through the BH ( $\dot{M}_H$ ), out in the jet ( $\dot{M}_j$ , at  $r = 50 r_g$ ), and out in the magnetized wind ( $\dot{M}_{mw,o}$ , at  $r = 50 r_g$ ) with legend. The middle subpanel shows  $Y$  for similar conditions. The bottom subpanel shows the efficiency ( $\eta$ ) for similar conditions. Horizontal lines of the same colors show the averages over the averaging period, while square/triangle/circle tickers are placed at the given time and values. In summary, the efficiency is high at  $\eta \sim 200\%$ . Also, despite plenty (up to  $10\times$  around  $t \sim 8500 r_g/c$ ) of same-signed polarity magnetic flux surrounding the BH, the magnetic flux reaches a stable saturated value of  $Y_H \approx 17$  as managed by magnetic Rayleigh-Taylor modes. This suggests that the simulation has reached a force balance between the magnetic flux in the disk and the hot heavy inflow.

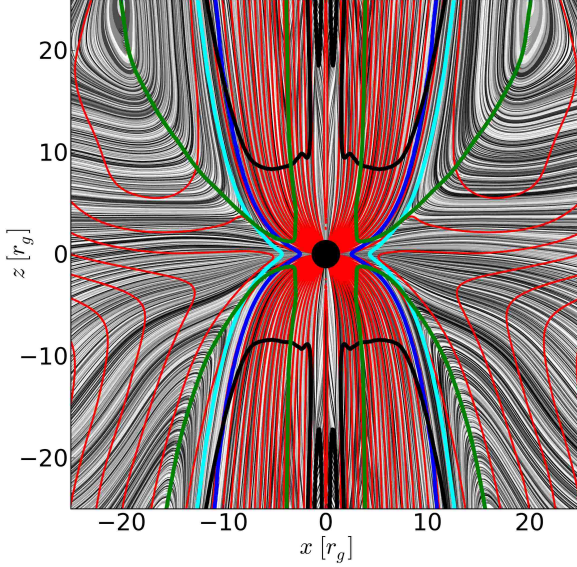
#### 5.4 Time-Averaged Radial ( $r$ ) Dependence

Figure 7 shows the time-averaged densities, 3-velocities, and comoving 4-fields vs. radius using a density-weighted average to focus on heavy disk material. The solution is in inflow equilibrium (3 inflow times; see section 3.7) only out to  $r \sim 30 r_g$  and has reached a single inflow time within  $r \sim 55-100 r_g$  depending upon how one defines it. Beyond the BH, the rest-mass and internal energy densities are quite flat. The rotational velocity is quite sub-Keplerian, which is primarily a consequence of thermal pressure playing an equal role to total gravity, unlike in thinner disks that are more naturally Keplerian. This effect is also seen in prior MHD simulations (Igumenshchev et al. 2003; Pen et al. 2003).

The GR viscosity estimate for  $v_r$  denoted  $v_{\text{visc}}$  (see above Eq. (29)) underestimates the simulation  $v_r$  when using the  $\alpha$ -viscosity with total pressure. A more accurate match is found when using magnetic pressure. Also, choosing  $\theta^d \rightarrow \theta^e$  or  $\theta^d \rightarrow |c_s/v_{\text{rot}}|$  still leads to a poor fit to  $v_r$ . Only if we set  $\alpha(\theta^d) \rightarrow 0.1$  at all radii does  $|v_{\text{visc}}| \approx |v_r|$  outside the ISCO and inside the inflow equilibrium region. The simulation  $v_r$  gives  $\epsilon \sim 0.1$  for Eq. (1).

Figure 8 shows the fluxes (see section 3.5) vs. radius as well as the field line angular rotation frequency  $\Omega_F$  (using various definitions defined in section 3.6). These quantities are associated with conserved quantities such that ratios of total fluxes would be constant along flow-field lines in stationary ideal MHD. The total fluxes are constant out to large radii, indicating a single inflow time is achieved over about 2 decades in radius. The true total fluxes are actually even flatter near the BH if one more accurately accounts for numerical floor injection as done in Tchekhovskoy et al. (2011), but this is a small error. Also shown are the components (inflow, jet, magnetized wind, and entire wind) of the mass and energy flow. The mass inflow and outflow at large radii follow power-laws after sufficient averaging over turbulent eddies. The jet efficiency is order 200% and is constant at large radii.

The winds increase in efficiency with radius, but the jet dominates the efficiencies of the winds. Power-law fits over the outer-radial domain (including the region not actually in inflow equilibrium) for the mass flow rates are  $\dot{M} \propto r^{1.7}$  for the inflow and entire wind,  $\dot{M} \propto r^{0.9}$  for the jet, and  $\dot{M} \propto r^{0.4}$  for the magnetized wind.



**Figure 6.** Flow-field as in Figure 3, except time-averaged and zoomed-in on the BH region that is in inflow equilibrium (3 inflow times). The colored (green, black, cyan, and blue) thick lines correspond to time-averages of quantities  $Q = \{u', u_r, \beta, b^2/\rho_0\}$ , respectively, at values  $[Q]_t = \{0, -1, 2, 1\}$ . While near the BH the flow has  $[b^2/\rho_0]_t \gtrsim 1$  as averaged directly, the dense inflow has  $b^2/\rho_0 \lesssim 1$  at all radii. The inflow occurs in geometrically thin streams not accounted for when computing the unweighted average. In summary, the BH is threaded by ordered magnetic flux, and the flow exhibits equatorial asymmetry over many inflow times.

At  $r \sim 30r_g$ , the entire wind component has an average velocity of order  $v_w/c \sim 0.01$  or  $v_w \sim 3000\text{km/s}$ .

The specific magnetic flux  $\Upsilon$  measures the total absolute radial flux. The figure shows that the total radial flux is much larger than the inflow-only component because the jet harbors most of the magnetic flux. The field line angular frequency  $\Omega_F \sim \Omega_H/4$  (as in BZ77's paraboloidal model) in the disk+corona+wind (i.e. “fdc” averaging, for full flow except the highly-magnetized jet).

Figure 9 shows the time-averages for the disk's geometric half-angular thickness ( $\theta^d$ ), the thermal half-thickness ( $\theta^t$ , using the density-weighted average), flow interface angular locations, resolution of the MRI wavelength, approximate  $\alpha$  viscosity parameter, and magnetic fluxes vs. radius. The magnetic field compresses the disk leading to decreasing  $\theta^d$  with decreasing radius. While  $\theta^d \ll 1$  near the BH,  $\theta^t = \arctan(c_s/v_{\text{rot}}) \gtrsim 1$  and  $\arctan(c_s/v_K) \gtrsim 1$ . Hence, the flow is not in vertical hydrostatic equilibrium due to the strong magnetic field. Note that using  $v_K$  instead of  $v_{\text{rot}}$  in the expression for  $\theta^t$  gives a similarly large thermal half-thickness. The disk-corona and corona-jet interfaces trace the path of the well-collimated jet out to large radii. The  $Q_{\theta, \text{MRI}} \gg 6$  as required to resolve the MRI (Sano et al. 2004), while in the inflow equilibrium region  $S_{d, \text{MRI}} \lesssim 1/2$ , indicating the MRI is suppressed. Even using  $\Omega \rightarrow \Omega_K$  in  $S_{d, \text{MRI}}$  leads to  $r_{S_{d, \text{MRI}}=1/2} \approx 8r_g$ , so the MRI suppression near the BH is not only due to sub-Keplerian motion but also disk compression by the accumulated magnetic flux. The horizon's time-averaged radial absolute magnetic flux is  $\Phi_{r, \text{H}} \sim 200$  and there is an additional  $\Psi_{\text{eq}} \sim 100$  same polarity magnetic flux available.

#### 5.4.1 Comparison with Gammie (1999) Model

Figure 10 shows a comparison between the fiducial model and the Gammie (1999) model of a magnetized unstratified accretion flow

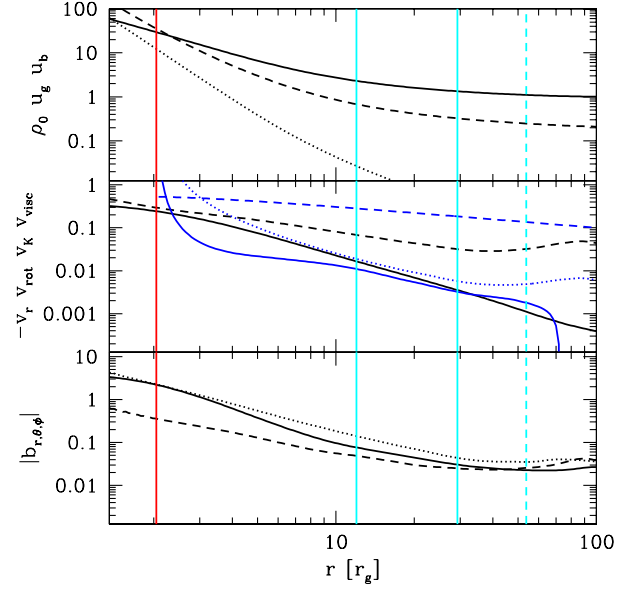


**Figure 7.** The time-angle-averaged densities, 3-velocities, and 4-field strengths using a density-weighted average. Top panel shows rest-mass density ( $\rho_0$ ) as black solid line, internal energy density ( $u_g$ ) as black short-dashed line, and magnetic energy density ( $u_b$ ) as black dotted line. Middle panel shows negative radial velocity ( $-v_r$ ) as black solid line, rotational velocity ( $v_{\text{rot}}$ ) as black short-dashed line, Keplerian rotational velocity ( $v_K$ ) as blue short-dashed line, and  $\alpha$ -viscosity theory radial velocity ( $v_{\text{visc}}$ ) when using  $p_b$  in denominator for  $\alpha = \alpha_b$  (blue solid line) and when choosing a fixed  $\alpha(\theta^d)^2 = 0.1$  (blue dotted line). Bottom panel shows comoving 4-field spatial components with  $r$ ,  $\theta$ , and  $\phi$  components shows as solid, short-dashed, and dotted black lines, respectively. The vertical red line marks the ISCO. Vertical solid cyan lines show range from  $r = 12r_g$  to 3 inflow times. The short-dashed vertical cyan line marks a single inflow time. In summary, dense filaments maintain  $u_b/\rho_0 \lesssim 1$  and  $\beta \gg 1$  near the horizon, while a similar plot (see bottom-left panel in Figure 10) averaged over the entire disk+corona+winds shows  $u_b/\rho_0 \gg 1$  and  $\beta \ll 1$  near the horizon. Also, the rotational velocity is quite sub-Keplerian.

within the ISCO. A value of  $\Upsilon \approx 8.7$  was used to match the Gammie model's value of the EM component of the specific angular momentum at the horizon, while the effective disk thickness was varied to best fit the magnitude of  $u_b$  at the horizon. All quantities use “fdc” type averaging focusing on all parts of the flow except the highly-magnetized jet. Compared to the densities vs. radius shown in Figure 7, here clearly  $u_b \gg \rho_0$  on the horizon due to averaging over the entire disk+corona+winds. The densities monotonically increase towards the BH as the inflow is vertically compressed by magnetic field.

If  $\Upsilon$  is only integrated across the time-averaged disk where  $\dot{M}$  is non-zero (i.e. “fdc” averaging: full flow except the highly magnetized part of the jet), then we find  $\Upsilon \approx 1.5$ . However, within the heavy dense filaments (i.e. density-weighted average), we find  $\Upsilon \approx 0.1$ . Also,  $\beta \gg 1$  in the dense flow, while  $\beta \ll 1$  over the disk+corona+winds. This shows that the heavy filamentary parts of the disk inflow are quite under-magnetized compared to their surroundings, which is as expected for accretion through efficient magnetic Rayleigh-Taylor instabilities.

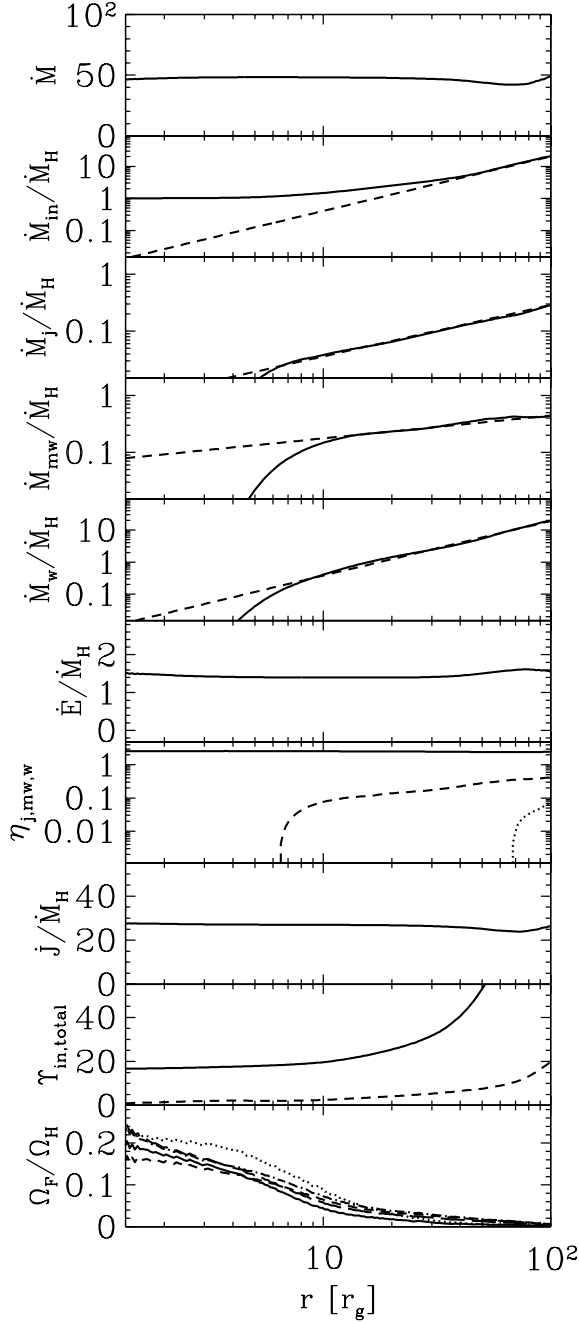


**Figure 8.** The time-averaged angle-integrated fluxes. From top to bottom, panels are: Total mass accretion rate ( $\dot{M}$ ), inflow rate ( $\dot{M}_{\text{in}}$ ), jet outflow rate ( $\dot{M}_j$ ), magnetized wind outflow rate ( $\dot{M}_{\text{mw}}$ ), entire wind outflow rate ( $\dot{M}_w$ ), total specific energy accretion rate ( $\dot{E}/\dot{M}_H$ ), efficiency for the jet (solid line) magnetized wind (short-dashed line) and wind (dotted line), total specific angular momentum accretion rate ( $j = j/\dot{M}_H$ ), specific magnetic flux  $\Upsilon$  for the total flow (solid line) and pure inflow with  $u_r < 0$  (short-dashed line), and field line angular rotation frequency per unit BH angular frequency ( $\Omega_F/\Omega_H$ ) for time-averaged versions of  $\Omega_F^d$  (solid line),  $\Omega_F^c$  (short-dashed line),  $\Omega_F^e$  (dotted line),  $|\Omega_F^d|$  (long-dashed line), and  $|\Omega_F^c|$  (dot-short-dashed line). These  $\Omega_F$  are averaged within the disk+corona part of the flow. Power-law fits for mass inflow and outflow rates are shown as short-dashed lines. In summary, inflow equilibrium is achieved over a couple decades in radius, and the mass outflows follow a power-law behavior.

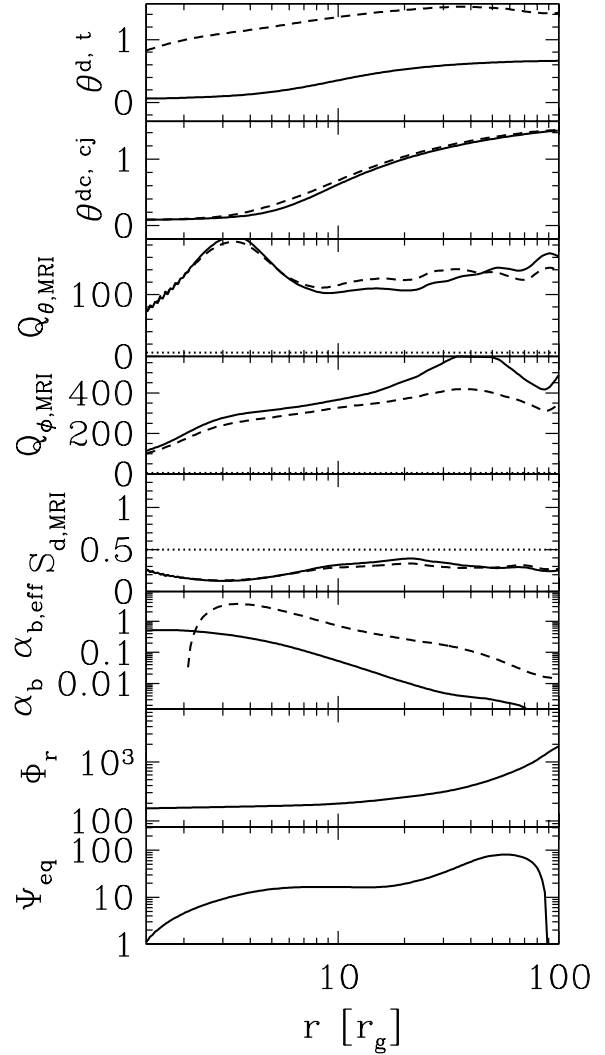


**Figure 9.** Other time-angle-averaged quantities. From top to bottom, panels are: density half-angular thickness ( $\theta^d$ , solid line) and thermal half-angular thickness ( $\theta^t$ , short-dashed line), disk-corona interface angle ( $\theta^{dc}$ , solid line) and corona-jet interface angle ( $\theta^{cj}$ , short-dashed line), number of cells per fastest growing MRI wavelength ( $Q_{\theta,\text{MRI}}$ , solid line;  $Q_{\theta,\text{weak,MRI}}$ , short-dashed line) with  $Q_{\theta,\text{MRI}} = 6$  shown as dotted line above where the vertical ( $\theta$ ) MRI is resolved, number of cells per fastest growing MRI wavelength ( $Q_{\phi,\text{MRI}}$ , solid line;  $Q_{\phi,\text{weak,MRI}}$ , short-dashed line) with  $Q_{\phi,\text{MRI}} = 6$  shown as dotted line above where the azimuthal ( $\phi$ ) MRI is resolved, number of fastest growing MRI wavelengths across the full disk thickness ( $S_{d,\text{MRI}}$ , solid line;  $S_{d,\text{weak,MRI}}$ , short-dashed line) with  $S_{d,\text{MRI}} = 1/2$  shown as dotted line below where the MRI is suppressed, viscosity parameter ( $\alpha_b$ , solid line;  $\alpha_{b,\text{eff}}$ , short-dashed line), radial absolute magnetic flux ( $\Phi_r$ ), and equatorial magnetic flux ( $\Psi_{\text{eq}}$ ). In summary, the disk is compressed by the horizon's magnetic flux leading to smaller  $\theta^d$  as  $r$  drops despite little change in  $\theta^t$ . Also, the linear MRI is suppressed even in the dense inflow.

### 5.5 Time-Averaged Angular ( $\theta$ ) Dependence

Figure 11 is similar to Figure 7 but for quantities vs.  $\theta$  at four different radii. This also highlights how the disk flow is compressed as it approaches the horizon. The time-averaged density is well-fit by a Gaussian with width  $\theta^d \approx 0.12$  at  $r = r_H$  even though the time-average of the instantaneous  $\theta^d \sim 0.06$ . This is because the time-average of density blurs the width of the narrow disk that oscillates

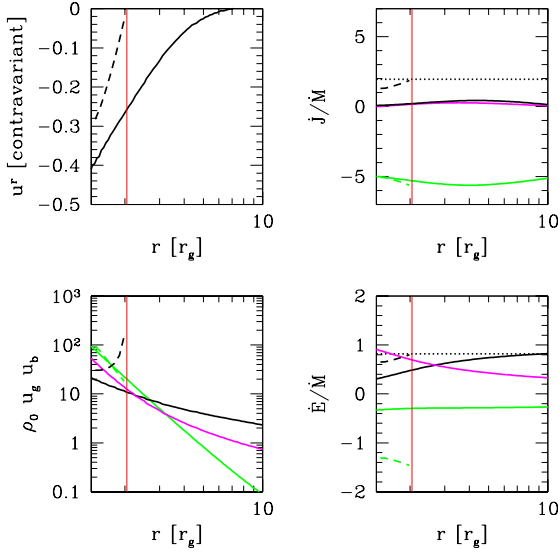


**Figure 10.** Comparison between the accretion flow for the fiducial simulation (“fdc” averaging, focusing on entire flow except the highly-magnetized jet, shown by solid lines) and the Gammie (1999) model for an unstratified magnetized inflow within the ISCO (shown by dashed lines). In all panels, red vertical lines shows the location of the ISCO. Top-left panel: Shows the radial 4-velocity, where the Gammie solution assumes  $\underline{u}^r = 0$  at the ISCO. Finite thermal effects lead to non-zero  $\underline{u}^r$  at the ISCO for the simulated disk. Bottom-left panel: Shows the rest-mass density ( $\rho_0$ , black line), the internal energy density ( $u_g$ , magenta line), and magnetic energy density ( $u_b$ , green line). Top-right and bottom-right panels: Show simulation results and Gammie solution for the specific particle (PA) flux (black line), specific enthalpy (EN) flux (magenta line), and specific electromagnetic (EM) flux (green line). Horizontal dotted black lines are the Novikov-Thorne thin disk solution (i.e. particle/radiation term). This figure is comparable to fig. 10 for a somewhat thick ( $\theta^d \sim 0.2$ – $0.25$ ) disk in McKinney & Gammie (2004) and to fig. 11 for a thin ( $\theta^d \sim 0.05$ ) disk in Penna et al. (2010). As for the prior thick disk simulations, the model fits  $\dot{J}$  and  $b^2$  but not  $\dot{E}$ .

in height about equal to its own height. Since the time-averaged density is a Gaussian, the estimate of the thermal thickness  $\theta'_p$  given by Eq. (13) would have given  $\theta'_p \sim \theta^d$  if the disk were in hydrostatic equilibrium. That  $\theta^d \ll \theta'$  close to the BH (as shown in Figure 9) shows that the thermal content remains relatively unchanged despite significant geometric compression by the polar magnetic flux. The figure also shows that the total pressure is roughly constant with angle as dominated by the magnetic pressure. The behavior of  $v_\theta, v_\phi$  near the polar axes is affected by the numerical floor mass injection, although this region contains little energy or energy flux compared to other angles.

Figure 12 shows the horizon’s values of quantities related to the BZ effect (Blandford & Znajek 1977). The simulation’s fluxes are computed via Eq. (10). The “full BZ-type EM formula” referred to in the figure uses the EM energy flux computed from equation 33 in McKinney & Gammie (2004), which only assumes stationarity and axisymmetry (rather than also small spin in BZ77) and uses the simulation’s  $\Omega_F(\theta)$  and  $\underline{B}'(\theta)$  on the horizon. This figure shows that most of the horizon is highly magnetized due to accretion occurring through a magnetically compressed inflow.

The agreement between the simulations and the BZ picture is excellent for the highly magnetized regions, where roughly  $\Omega_F \sim \Omega_H/4$  near the disk-jet interface (here,  $\Omega_F$  is the time-average of Eq. (27)). While the simulation is roughly consistent with BZ’s

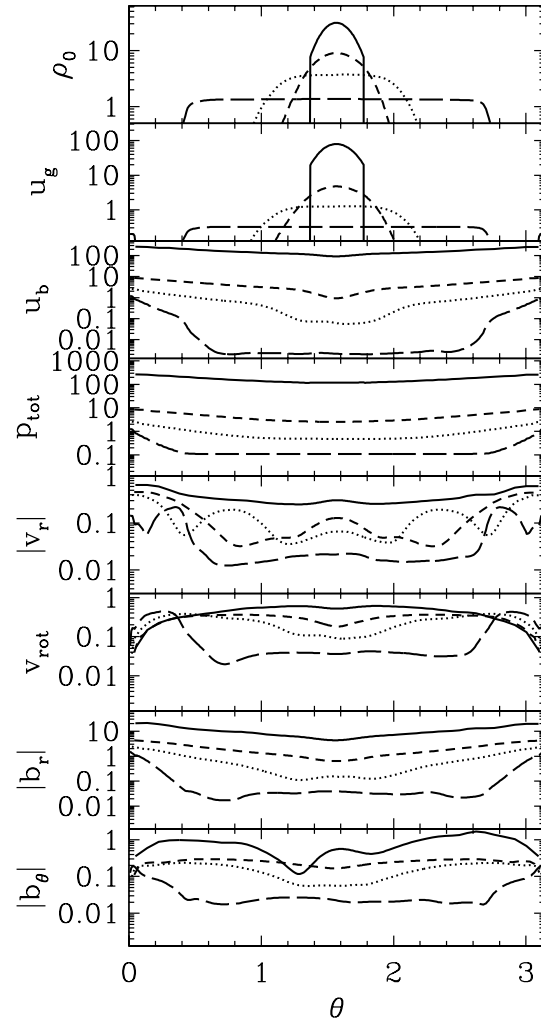


**Figure 11.** Similar quantities as in Figure 7, except plotted vs.  $\theta$  at  $r = \{r_H/r_g, 4, 8, 30\}r_g$  (respectively: solid, short-dashed, dotted, and long dashed lines). If numerical density floors were activated at some space-time point, then  $\rho_0 = u_g = 0$  was set there. This shows up even in these time-averaged densities as a sharp drop-off, because the jet maintains high magnetizations at the poles during the interval time-averaged. In summary, the disk is compressed by the polar magnetic flux as the inflow approaches the horizon, and the total pressure is roughly constant with  $\theta$ .

paraboloidal solution, the equatorial  $\Omega_F$  is somewhat suppressed due to the disk inflow. Also, near the polar axes,  $\Omega_F$  is affected by ideal MHD effects and numerical floor mass injection. In the last  $\sim 3$  grid cells, limited resolution affects  $\Omega_F$ . However, both the grid and jet collimate, which leads to a well-resolved  $\Omega_F$  near the axes at slightly larger radii. Also, the most energetic part of the jet is near the disk-jet interface that dominates the dynamics at all radii. Even if we used a paraboloidal extension of our simulation data into the region where the numerical floor injection is important, this only changes the total efficiency by less than 20%.

## 5.6 Azimuthal ( $\phi$ ) Time Dependence

Figure 13 shows a large magnetic Rayleigh-Taylor disruption at  $t \approx 15172r_g/c$  once  $\Upsilon$  has reached its saturated value and the



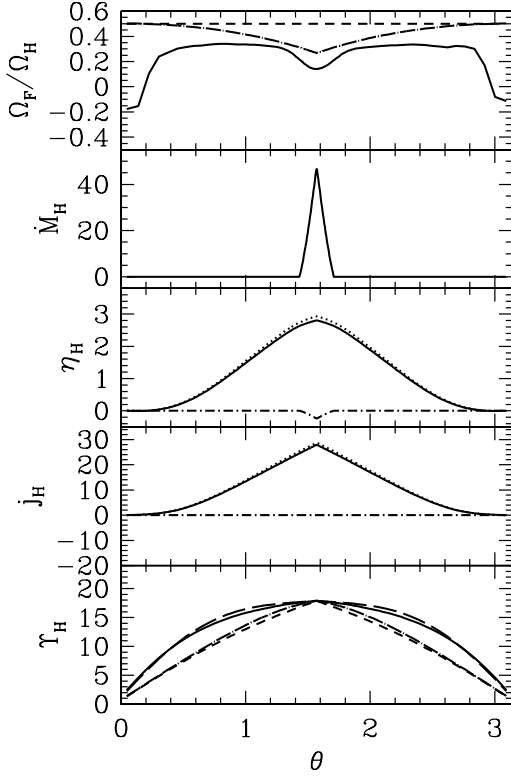


**Figure 12.** Time- $\phi$ -averaged quantities and flux integrals on the horizon as a function of  $\theta$ . From top to bottom: 1) Field line rotational angular frequency ( $\Omega_F/\Omega_H$ ) for simulation (solid line), 1st-order-in-spin accurate value for monopolar (short-dashed line) and paraboloidal (dot-long-dashed line) BZ solutions; 2) Rest-mass flux ( $\dot{M}_H$ ); 3) Electromagnetic (EM, solid line) and matter (MA, dot-short-dashed line) efficiency ( $\eta_H$ ), along with the full BZ-type EM formula without any renormalization (dotted line); 4) Electromagnetic (EM, solid line) and matter (MA, dot-short-dashed line) specific angular momentum flux ( $j_H = \dot{J}_H/\dot{M}_H$ ), along with the full BZ-type EM formula without any renormalization (dotted line); 5) Gammie parameter ( $\Upsilon_H$ ) for the simulation (solid line), and the BZ model for the cases: 0th-order-in-spin accurate monopolar field (short-dashed line), 0th-order-in-spin accurate paraboloidal field (dot-long-dashed line), and 2nd-order-in-spin accurate monopolar field (long-dashed line). These BZ versions are normalized so total magnetic flux is the same as in the simulation. Notice how the 2nd-order-in-spin accurate monopolar BZ model fits the simulation result quite well. For the last 3 panels, the divisor is (implicitly)  $\dot{M}_H$  that has been fully angle-integrated to a single value. So,  $\eta_H$ ,  $j_H$ , and  $\Upsilon_H$  show the angular dependence of  $\dot{E}_H$ ,  $\dot{J}_H$ , and  $\Psi_H$ , respectively. In summary, the agreement between the simulation and the BZ picture is excellent.

flow can no longer accept new magnetic flux on the BH. While an atypical looking outburst, other more typical snapshots, such as at  $t \approx 11272r_g/c$ , show roughly similar behavior including the same range of density variations. Such outbursts occur because magnetic flux is temporarily added to the BH and exceeds the saturated value, but then that extra flux is ejected back in magnetic interchange modes. Here,  $|m| = 1, 2$  modes appear to dominate.

Figure 14 shows the density vs.  $\phi$  at three radii ( $r = r_H, 4r_g, 8r_g$ ) for  $t \approx 15172r_g/c$  (as shown in Figure 13).  $\rho_0^{\text{avg}}$  shows the average with weight  $w = 1$ , and  $\rho_0^{\text{eq}}$  shows the density for a single grid cell cut exactly at the equator. Typical density variations averaged over the flow are up to factors of 10 near the horizon, while at any given  $\theta - \phi$  angles (here the equator) the density varies considerably (down to the limits of the numerical density floors).

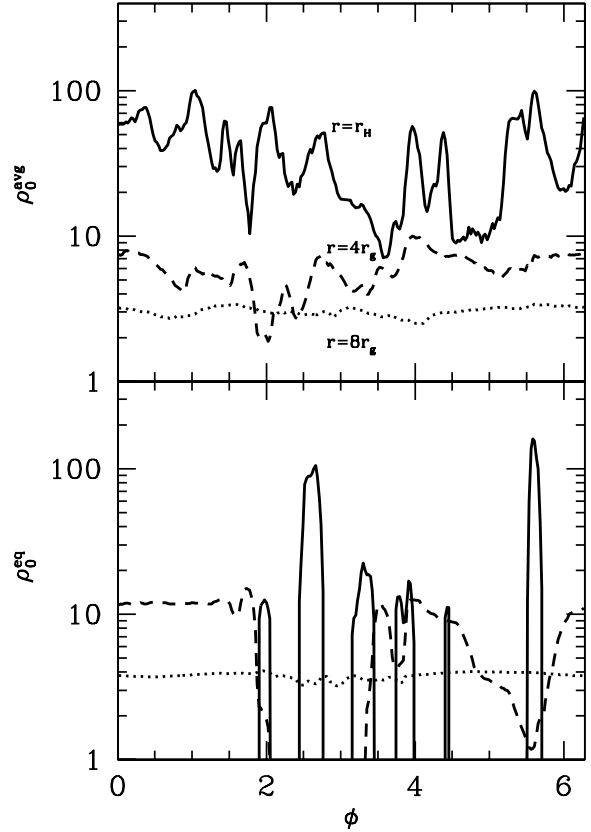


**Figure 14.** Shows rest-mass density at  $t \approx 15172r_g/c$  (as shown in Figure 13), as  $\theta$ -averaged over the entire flow ( $\rho_0^{\text{avg}}$ ) and as cut along the equator ( $\rho_0^{\text{eq}}$ ) at three radii (in all panels:  $r = r_H$  shown as solid line,  $r = 4r_g$  shown as short-dashed line, and  $r = 8r_g$  shown as dotted line). The drop-outs in density correspond to where the mass is dominated by numerical floor mass injection due to the high  $u_b/\rho_0$  in such regions, so we have set  $\rho_0 = 0$  there to show where the density could be smaller than the floor. In summary, the variations in density become quite large near the BH.

This shows how the dense part of the flow is forced through the magnetosphere via magnetic Rayleigh-Taylor modes.

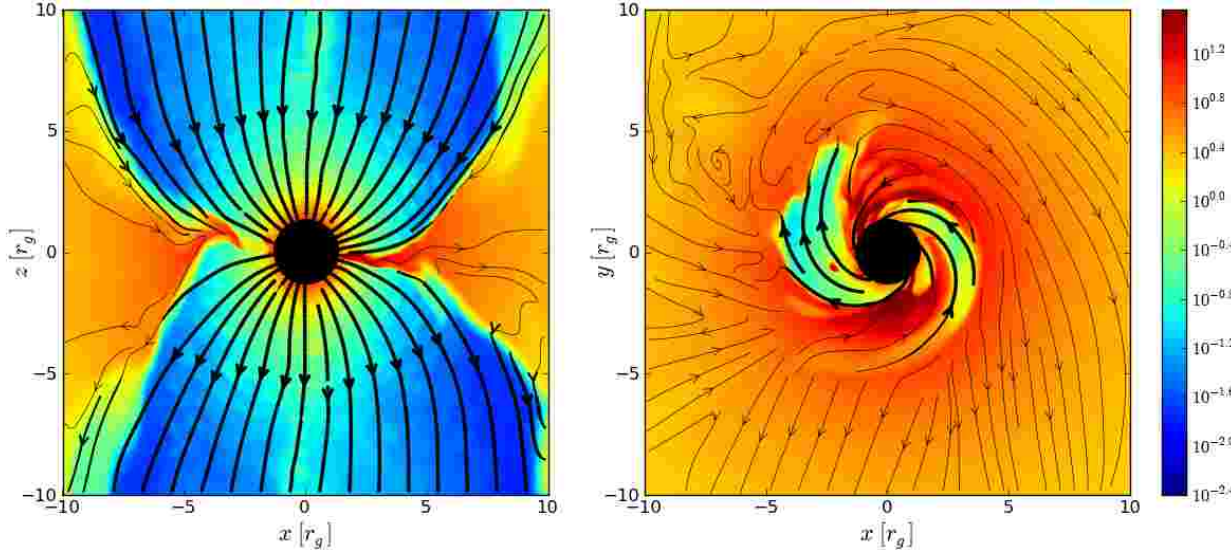
### 5.7 Time-Averaged Azimuthal ( $\phi$ ) Dependence

Figure 15 shows the normalized time-average of the Fourier decomposition in the  $\phi$ -direction ( $[|a_m|]_t/[|a_0|]_t$ ) using Eq. (30) for the “Disk” and “Jet” with quantity  $Q$  as  $\rho_0 u^r$ ,  $\rho_0$ ,  $u_g$ ,  $b^2$ , and  $T^{\text{EM}r}_t$  that gives, respectively, the actual  $\dot{M}$ , comoving mass  $\dot{M}_0$ , comoving thermal energy  $\dot{E}_g$ , comoving electromagnetic energy  $\dot{E}_B$ , and actual electromagnetic energy flux  $\dot{E}^{\text{EM}}$ . As with flux ratios, we compute  $[|a_m|]_t/[|a_0|]_t$  instead of  $[|a_m/a_0|]_t$  because the latter would exaggerate mode power during transient moments when  $a_0(t)$  becomes small and potentially zero.

We find that there is large  $|m| > 0$  power in  $\dot{M}$  and  $\dot{E}_{\text{EM}}$ , but there is little power in  $|m| > 0$  for  $b^2$  in the jet. Since  $|a_{m>0}| \approx |a_{m=0}|$  for  $\dot{M}$ , this shows that accretion occurs primarily through non-axisymmetric modes. Also,  $|a_{m>0}| \approx |a_{m=0}|$  for the jet electromagnetic power even at  $r = 8r_g$ , so the jet power contains significant non-axisymmetric structure. The  $|m| = 1$  dominates all  $|m| > 0$ , but  $|a_m|$  and  $|a_1|$  are similar up to  $m \approx 20$ .

Figure 15 also shows the azimuthal correlation length scale





**Figure 13.** Snapshot at  $t \approx 15172 r_g / c$  for the fiducial model during one of the larger magnetic Rayleigh-Taylor disruptions, just after which the mass accretion rate increases. Otherwise similar to the upper panels in Figure 4. During this disruption,  $|m| = 1, 2$  modes appear to dominate the non-axisymmetric accretion.

(Eq. (31)), which is always well-resolved beyond the horizon. Note that if we compute Eq. (30) as a spectrum of the averaged flow rather than as an average of the spectrum, then even on the horizon the correlation lengths are very well-resolved. The correlation length scale  $\lambda_{\phi, \text{cor}}$  is related to the mode  $m_{\text{cor}} = 2\pi/\lambda_{\phi, \text{cor}}$ . For example, for  $M_0$  (i.e. the density in the disk), we find  $m_{\text{cor}} \approx 33.8, 15.9, 13.2, 8.5$  at  $r = r_H, 4r_g, 8r_g, 30r_g$ , respectively. With  $\theta^d \approx 0.06, 0.13, 0.29, 0.59$ , one obtains  $\lambda_{\phi, \text{cor}}/\theta^d \approx 3.1, 3.0, 1.6, 1.3$ , respectively. So as the magnetic flux near the BH vertically compresses the inflow, the azimuthal correlation length drops, but not in proportion to the disk height.

### 5.8 Quasi-Periodic Oscillations

BH accretion disks are observed to have QPOs roughly classified as either high-frequency QPOs (HFQPOs) or low-frequency QPOs (LFQPOs). In BH x-ray binaries, QPOs are seen in only specific states (Fender et al. 2004; Abramowicz 2005; Remillard & McClintock 2006), such as the steep-power law (SPL) state (related to the very high state and intermediate state, during which powerful transient jets are observed) (Done & Gierliński 2003; Gierliński & Newton 2006; Oda et al. 2009). For BH x-ray binaries, HFQPOs range from 100Hz (GRS1915+105) to 300Hz (1655-40) corresponding to a period of  $\tau \sim 70\text{--}130 r_g / c$ . HFQPO frequencies are sometimes in a 3:2 ratio (Psaltis et al. 1999). QPOs are not expected to be as easily seen in AGN as for x-ray binaries (Vaughan & Uttley 2005); but some AGN may have QPOs, such as SgrA\* (Meyer et al. 2008; Dolence et al. 2012) and RE J1034+396 (Gierliński et al. 2008). NS QPOs have similar features (van der Klis 1998).

BH x-ray binary QPOs are not seen (or are very weak) in the high-soft state that is typically associated with a thin disk dominated by MHD-MRI turbulence (Wijnands & van der Klis 1999; Remillard 2005; Rubio-Herrera & Lee 2005; Machida & Matsumoto 2008; Mondal et al. 2009). The lack of QPOs in such a state is expected because non-linear turbulence tends to reduce coherence. Also, the existence of a bright hard state defies explanation by standard viscous models that would predict the bright state

should be soft (Oda et al. 2009). This indicates that a qualitatively new accretion state (like the MCAF state) may be required.

Analytical models and simulations have demonstrated QPOs through various mechanisms. The hope is that QPOs could be used to measure BH spin and mass (Stella & Vietri 1999). Disk mode oscillations may cause either HF or LF QPOs (Reynolds & Miller 2009; O’Neill et al. 2009, 2011), disk precession causes LFQPOs in GRMHD simulations of tilted disks (Dexter & Fragile 2011), and dynamo field oscillations in local MHD simulations show LFQPOs (Davis et al. 2010; Guan & Gammie 2011). In some cases QPOs may be seen, but their statistical significance is highly uncertain. This includes HFQPOs seen in pseudo-Newtonian MHD simulations (Kato 2004). GRMHD simulations have shown HFQPOs in tilted disks (Henisey et al. 2009). However, in the latter case higher resolutions were found to eliminate the QPOs as distinct features because MRI turbulence destroys their coherence (Henisey, 2010, priv. comm.). Other GRMHD simulations with radiative transfer show some HFQPO features (Schnittman et al. 2006), but their significance is highly dependent upon model of “continuum” spectrum as a single power-law, while their power spectrum is identified as a broken power-law. So extra apparent power appears near the break.

Our GRMHD simulations also show coherent HFQPOs. We identify the coherence of the QPO by its quality factor  $Q \approx \nu/(\Delta\nu)$  for frequency  $\nu$ , where  $\Delta\nu$  is the full width at half of the maximum power (FWHM) (e.g. if the QPO distribution is modelled by a Lorentzian). All our thick disk poloidal field simulations at both resolutions ( $136 \times 64 \times 128$  and  $272 \times 128 \times 256$ ) show coherent QPOs during some part of the simulation at various radii ( $r = r_H, 4r_g, 8r_g, 30r_g$ ), while the QPOs are most coherent for the high-resolution fiducial model. This expected resolution dependence on  $Q$  implies that damping at low resolutions can make it difficult to resolve a coherent QPO. Radiative transfer (Broderick & McKinney 2010; Shcherbakov et al. 2010; Dexter et al. 2011) is necessary to see if these QPOs are observable. In this paper, we only consider the MHD dynamical properties of the HFQPO.

Figure 16 shows  $b_\phi$  averaged over  $\phi = 0$  to  $\phi = \pi/4$  (with no weighting) vs.  $\theta$  and time  $t$  at  $r = 4r_g$  (averaged over  $\pm 0.4r_g$  with no weighting) for the fiducial model. This shows possible QPOs.

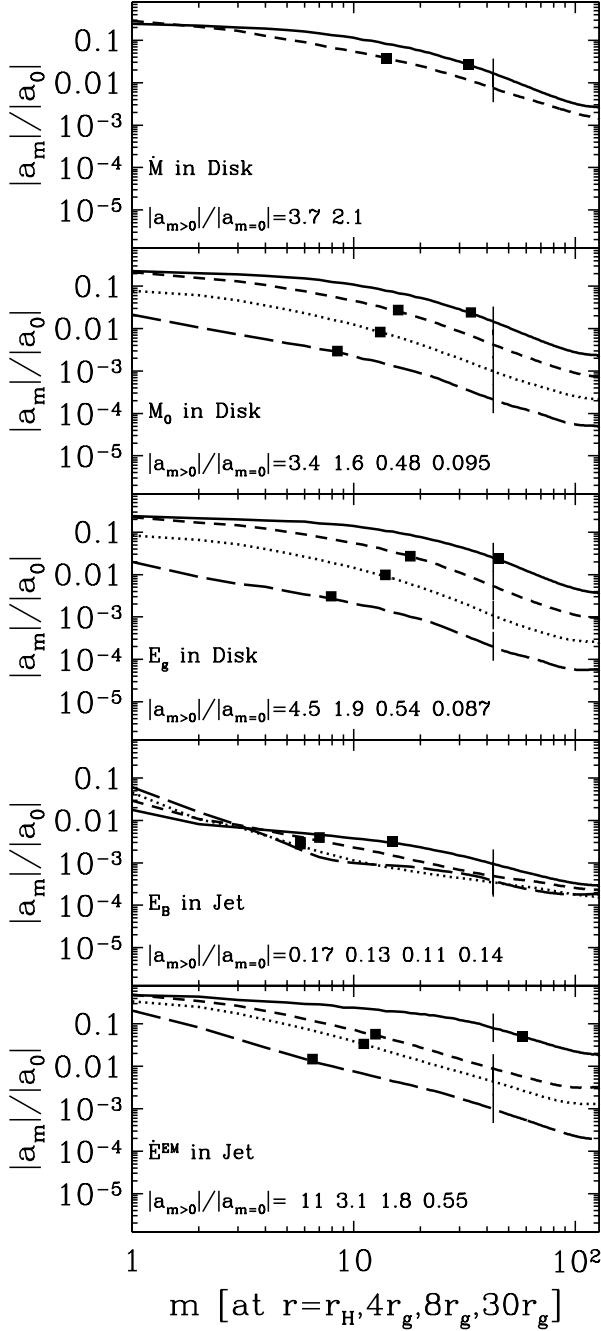


**Figure 15.** Time-averaged Fourier amplitude for  $m$  modes. Each panel shows result for  $r = r_H, 4r_g, 8r_g, 30r_g$  (respectively, solid, short-dashed, dotted, long-dashed lines), except the top panel that only shows results for  $r = r_H, 4r_g$  with same line types. The power in all  $|m| > 0$  modes relative to the  $|m| = 0$  mode is shown for each panel respectively for radii  $r = r_H, 4r_g, 8r_g, 30r_g$ . For each line, the vertical bar corresponds to  $m_{6\text{cells}} = N_\phi/6$ , where  $m > m_{6\text{cells}}$  are numerically damped on a dynamical time. For each line, squares mark the correlation length's  $m = m_{\text{cor}}$  mode, so azimuthal structure (e.g. turbulence) is resolved if  $m_{\text{cor}} \lesssim m_{6\text{cells}}$ . In summary, azimuthal structures are well-resolved across all quantities within the causally-connected region outside the horizon. Changes in  $m_{\text{cor}}$  with radius in the “Disk” partially track changes in the disk thickness. Most power is at  $|m| \sim 1$ , but significant power extends up to  $|m| \sim 20$  before dropping off more rapidly. Because  $|a_{m>0}| \approx |a_{m=0}|$  for  $\dot{M}$ , mass accretion is highly non-axisymmetric (see also Figure 14).

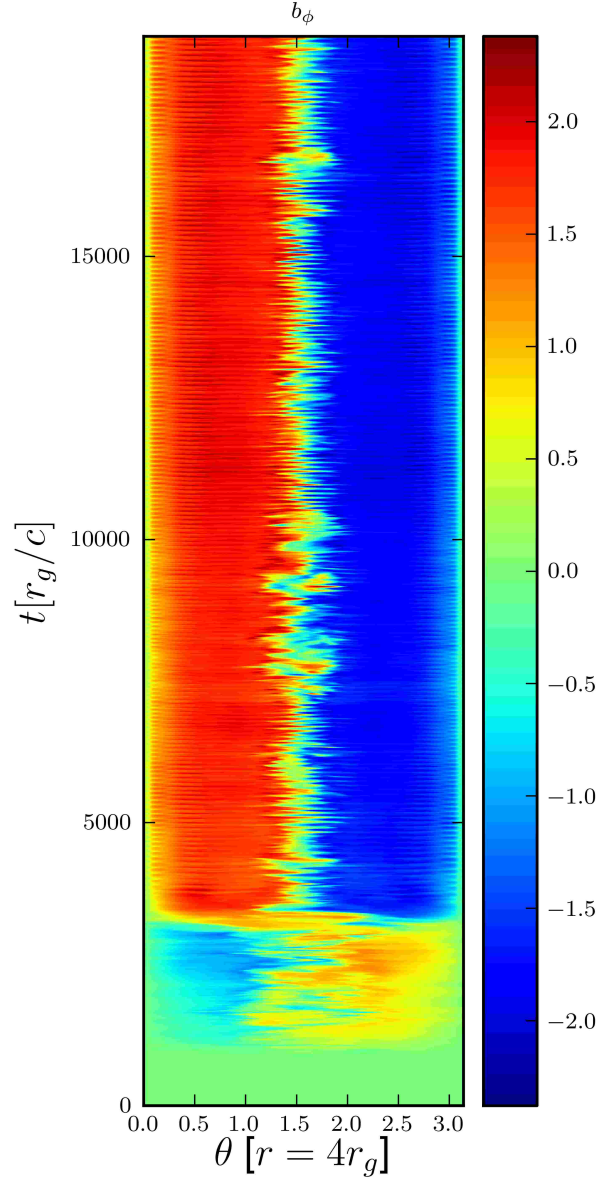


**Figure 16.**  $b_\phi$  vs.  $t$  and  $\theta$  at  $r = 4r_g$ . The field polarity switches at  $t \sim 2700r_g/c$ , after which magnetic flux accumulates and saturates. After saturation, the jet-disk QPO (JD-QPO) becomes coherent, here visible as horizontal stripes at late times.

Figure 17 shows a spectrogram for the power density vs. time and frequency for  $b^2$  at  $r = 4r_g$  at  $\theta \approx 2.9$  (i.e. deep within the jet). Power density is shown in commonly-used units: an integral of power density over a frequency range gives back the square of the fractional root-mean-squared (rms) amplitude of the variability in the original time series.

Figure 18 shows the Fourier transform of  $b^2(t)$  at the equatorial plane (at  $\theta = 0$ ), in the disk (at  $\theta = 1[\theta^d]_t$ , where  $[\theta^d]_t$  is the time-averaged  $\theta^d$ ) and in the jet (at  $\theta \approx 2.9$ ) at  $r = 4r_g$  as averaged from  $\phi = 0 - \pi/4$  to reduce noise while allowing us to resolve several  $|m|$  modes. The power density is given in units of  $(\text{rms}/\text{mean})^2$  multiplied by the total period ( $t = 12000 - 16000r_g/c$ , focusing on the high-Q period) over which the Fourier transform is performed, as a function of frequency (in units of  $c/r_g$ ). We find that  $Q \sim 100$

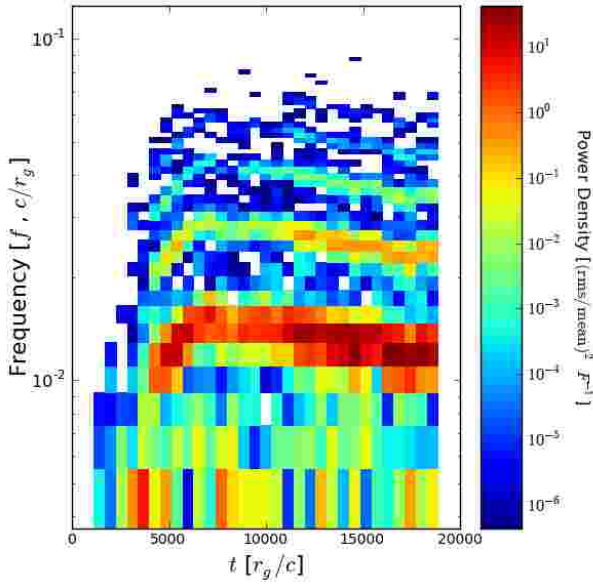


**Figure 17.** Spectrogram for the power density vs. time and frequency for  $b^2$  (with legend, where white is below lowest power in legend) at  $r = 4r_g$  at  $\theta \approx 2.9$  (i.e. deep within the jet). This shows the high  $Q$  oscillation starts once flux saturates for  $t \gtrsim 5000r_g/c$ , where  $\sim 3$  jet-disk QPO (JD-QPO) modes are visible. The frequency changes little as  $\dot{M}$  varies.

in the jet,  $Q \sim 10$  one scale height above the disk plane, and  $Q \lesssim 10$  in the disk plane. Other radii (e.g.  $r = r_H, 8r_g$ , and  $30r_g$ ) in the jet also show similar QPOs as features move out in the jet.

What is the nature of the HFQPOs in our simulations? Once poloidal magnetic flux has accumulated and reached its natural saturated limit, a semi-permeable magnetospheric barrier forms between the heavy disk inflow and magnetic flux threading the rotating BH and its jet. This magnetospheric interface is where magnetic field and density change somewhat abruptly. Linear stability analyses of such magnetospheric interfaces predict them to be unstable to Rayleigh-Taylor and Kelvin Helmholtz modes, which drive QPOs at spherical harmonic  $m$  modes based upon some rotational frequency ( $\Omega$ ) such that  $\Omega_{\text{QPO}} \approx m\Omega$  (Li & Narayan 2004; Fu & Lai 2012). These linear stability analyses predict that low  $m$  modes dominate the non-linear dynamics and that QPOs should appear. However, these models cannot determine what controls  $\Omega$ , the power of the  $m$  modes, or the coherence of the QPO.

Our MCAF simulations validate the prior linear stability analysis. We confirm that the magnetospheric interface is indeed unstable and that low- $|m|$  (primarily  $|m| = 1$ ) modes dominate. We also show that the unstable jet-disk interface drives coherent HFQPOs. A movie of snapshots like Figure 4 shows that once poloidal magnetic flux saturates, the jet and disk oscillate together.

Why do such QPOs appear in MCAFs and not MRI-dominated accretion flows? QPOs seen in prior MRI-dominated accretion flow simulations show (e.g.)  $m = 1$  spiral disk modes extending out in radius (Dolence et al. 2012). Other QPOs (Henisey et al. 2009) were absent at high resolutions due to decoherence by properly-resolved MRI-driven MHD turbulence (Henisey, 2010, priv. comm.). Such MRI-dominated simulations did not reach saturation of poloidal magnetic flux because of their limited initial poloidal flux. Yet, only once the poloidal flux has saturated does the magnetospheric interface form. In our models, the QPOs are driven due to the presence of an unstable *interface* between the jet

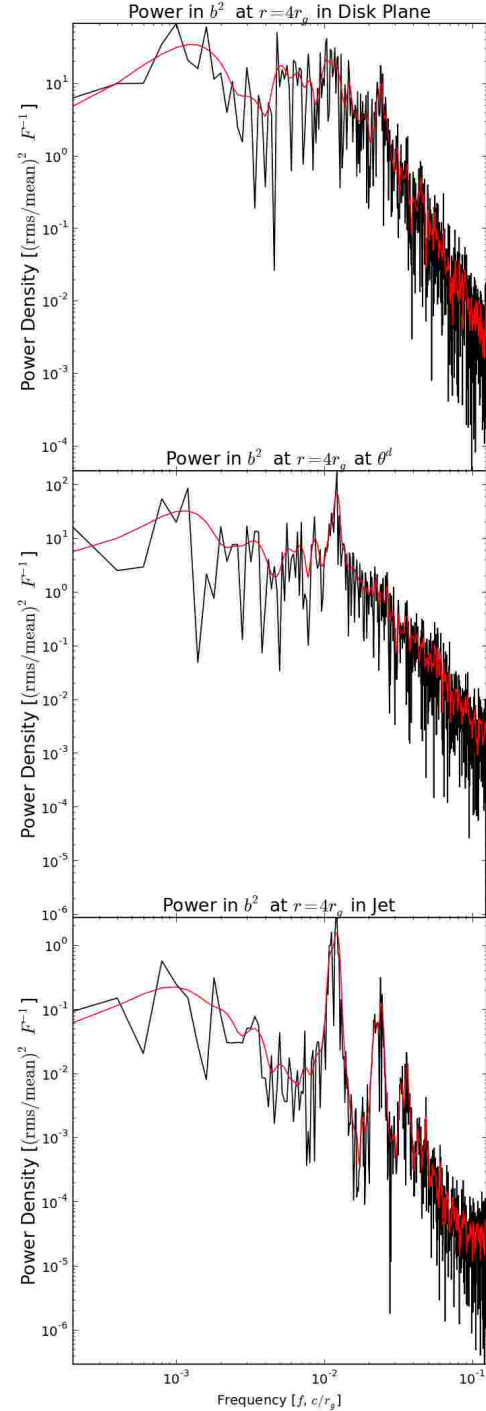


**Figure 18.** Power Density for  $b^2$  at  $r = 4r_g$  in the disk plane (top panel), one geometric half-angular thickness ( $\theta^d$ ) above the disk plane (middle panel), and deep within the jet at  $\theta \approx 2.9$  (bottom panel) shown as black lines. A smoothed (over 10 frequencies) version is shown as red lines. The disk has QPOs with quality factor  $Q \lesssim 10$ , a disk scale-height above the disk plane has  $Q \sim 10$ , while the jet itself shows a few different harmonics with up to  $Q \sim 100$ . The jet harmonics correspond to  $|m| = \{1, 2, 3\}$  modes based upon the field line angular frequency (driven by the black hole rotation frequency) at the disk-jet magnetospheric interface where the jet-disk QPO (JD-QPO) mechanism operates.

and disk where force balance has been achieved between magnetic forces by the jet and (e.g.) ram forces by the disk inflow.

What sets the frequency of the QPOs in our simulations? In prior magnetospheric QPO models, the QPO is driven as an interface instability that oscillates at an  $m$ -mode-based rotational frequency  $\Omega$ . The magnetospheric interface in our simulations is between the jet and the disk. The strong field at the disk-jet interface forces the plasma rotation frequency ( $\Omega$ ) to be similar to the field line rotational frequency  $\Omega_F$ , so all  $\Omega$  are similar at the interface. The QPO frequency is thus set by the BH spin frequency ( $\Omega_H = a/(2Mr_H)$ ) due to the BH dragging the field at angular frequency  $\Omega_F \approx \Omega_H/4$  at the jet-disk interface, as consistent with BZ's paraboloidal solution (see Figure 12).

The QPO frequencies seen in Figures 17,18 correspond to  $|m| = 1, 2, 3$  modes at the jet-disk interface. That is,  $\Omega_{\text{QPO}} \approx m\Omega_F \approx m\Omega_H/4$ . The  $|m| = 1$  mode dominates, as shown in Figure 15. So, for example, the dominant QPO is due to the  $|m| = 1$  mode that in the fiducial simulation has period  $\tau \sim 70r_g/c$ , which agrees with  $\tau \approx 2\pi/(m\Omega_H/4) \approx 72.3r_g/c$  for  $m = 1$  and  $a = 0.9375$  from the above analysis. Other BH spins (e.g.  $|a/M| \lesssim 0.4$ ) might saturate at  $\Omega_{\text{QPO}} \sim m\Omega$  at the (e.g.) ISCO due to the disk dominating the plasma rotation rate near the disk-jet interface for such models (McKinney & Gammie 2004; McKinney 2005).

In summary, the period  $\tau \sim 70r_g/c$  for  $a/M \sim 0.9$  for our  $|m| = 1$  mode (with longer periods expected for lower BH spins) is consistent with the range of HFQPOs observed in BH x-ray binaries. Also, the disk-jet interface (driving the QPO) harbors a large electromagnetic energy density, so the disk-jet interface can dominate (non-thermal) synchrotron emission. Our work shows that coherent HFQPOs may be initiated by large-scale magnetic flux near the BH, but more work is required to test their observability.

## 6 DEPENDENCE UPON FIELD GEOMETRY AND STRENGTH, SPIN, AND RESOLUTION

This section provides results for all our models. We also take this opportunity to tabulate results from the brief letters by McKinney & Blandford (2009); Tchekhovskoy et al. (2011). Quantities are time-averaged from  $T_i^a$  to  $T_f^a$  given in Table 2. The chosen  $T_i^a$  is at least after the dimensionless fluxes through the horizon have reached a quasi-steady-state. Typically  $T_f^a = T_f$ . Units in tables are  $GM = c = r_g = 1$ . Such tables are computed in other works (McKinney & Gammie 2004; De Villiers et al. 2005; Hawley & Krolik 2006), and our tables should prove useful for comparisons with future works.

Summarizing our MB09 models: Results are similar to most prior MHD simulations of moderately thick disks. The flows are dominated by the local MRI, nearly Keplerian, and not efficient. For MB09D,  $T_f^a = 3000$ , after which turbulence decays. The model MB09D focused on the large-scale jet that is only moderately affected by how the disk behaves at late time, and the jet's correlation lengths are well-resolved beyond the horizon. Unlike our other models, a color plot (not shown) of  $b_\phi$  or  $b^2$  vs.  $t$  and  $\theta$  shows a butterfly type LFQPO behavior with a period of roughly 15–30 times the orbital period at  $r = 4r_g$  or  $8r_g$ , as similar to fig. 10 in Guan & Gammie (2011) and figs. 8 and 12 in Davis et al. (2010).

Summarizing our “thinner disk” TNM11 models: Results are similar to the thick disk poloidal field models. Plotting (not shown) all prior figures, some similarities and differences are notable. The TNM11 models are more Keplerian due to  $\theta^t < 1$ . The efficiencies are  $\eta_j \sim 100\%$  for  $a/M \gtrsim 0.9$  and  $\eta_{\text{mw},w} \sim 30\%$  by  $r = 100r_g$  for  $a/M = 0.99$ . On the horizon,  $\Omega_F/\Omega_H$  vs.  $\theta$  more closely fol-

lows the profile expected for a paraboloidal field due to the lower numerical density floors.  $S_{d,\text{MRI}} \lesssim 1/2$  inside  $r \sim 20r_g$  (dependent upon initial  $\beta$  and simulation duration), indicating that the MRI is suppressed over smaller radii. The value of  $\alpha$  at  $r \sim 10r_g$  is larger. Compared to the thick disk models, the density-weighted inflow is even more weakly magnetized (i.e.  $b^2/\rho_0 \ll 1$  and  $\beta \gg 1$ ). Also,  $\epsilon \sim 0.05\text{--}0.1$ , as used in Eq. (1). No coherent HFQPOs are seen in the thinner disk models, but the quantities (e.g.  $\eta_H$ ) are much more variable. The lack of HFQPOs and the higher variability may be due to the disk being thinner. However, for some of these models, this could also be due to lower  $N_\theta, N_\phi$  available for capturing magnetic Rayleigh-Taylor modes, e.g., the azimuthal correlation length is only marginally resolved with  $Q_{m,\text{cor}} \leq 6$ . (However, the time-averaged quantities are actually well-resolved.)

### 6.1 Disk Thickness, Disk-Corona, and Corona-Jet Interfaces

Table 3 shows the number of grid cells ( $N_{\theta,H}^d$ ) at the horizon that cover the angular span of the disk's geometric half-angular thickness ( $\theta_H^d$ ) ( $\theta^d$  is computed by Eq. (12)), the disk thickness at the horizon ( $\theta_H^d$ ) and other radii  $r$  ( $\theta_{r/r_g}^d$ ), the thermal half-angular thickness ( $\theta_{20}^t$  is  $\theta_\rho^t$  at  $r = 20r_g$  as computed by Eq. (13)), the disk-corona interface angular locations at the same radii ( $\theta_{r/r_g}^{dc}$ , defined by where  $\beta = 1$ ), and the corona-jet interface angular locations at the same radii ( $\theta_{r/r_g}^{cj}$ , defined by where  $b^2/\rho_0 = 1$ ). See section 3.4 for details. In summary, jets in the thicker disk models collimate better.

The rest-mass density geometric half-angular thickness ( $\theta^d$ ) is quite different than the thermal half-angular thickness ( $\theta^t \equiv \arctan(c_s/v_{\text{rot}})$ ), the latter being an estimate of  $\theta^d$  if gas pressure balances vertical gravity. Close to the BH,  $\theta^d \ll \theta^t$  is controlled by magnetic forces, and  $\theta^t \sim \theta^d$  only at large radii. About 6 cells should span the full disk to resolve it at a basic level, and most 3D models satisfy this even on the horizon ( $\sim 20$  cells for the fiducial model). The “magnetospheric radius” ( $r_m$ ) is not a sharp boundary, and instead magnetic forces gradually compress the disk.

### 6.2 Mass Accretion and Ejection Rates

Table 4 shows  $\dot{M}$  computed via the first row of Eq. (14) through the BH horizon ( $\dot{M}_H$ ), inflow-only mass accretion rate ( $\dot{M}_{\text{in}}$ ) at an inner radius of  $r_i = 10r_g$  giving  $\dot{M}_{\text{in},i}$  and an outer radius of  $r_o = 50r_g$  (except model MB09Q that uses  $r_o = 30r_g$  due to its limited radial domain) giving  $\dot{M}_{\text{in},o}$ . Also shown are  $\dot{M}$  through the jet ( $\dot{M}_j$ ), the magnetized wind at  $r_i$  ( $\dot{M}_{\text{mw},i}$ ) and  $r_o$  ( $\dot{M}_{\text{mw},o}$ ), and the entire wind at the same radii ( $\dot{M}_{w,i}$  and  $\dot{M}_{w,o}$ ).

Most models show massive winds, and the poloidal models show some mass carried in the magnetized wind and jet. Our models are in inflow-outflow equilibrium with  $\dot{M}_{\text{in},o} - \dot{M}_H \approx \dot{M}_{w,o} + \dot{M}_j$  (i.e. all outflowing material, that is not in the jet, is part of the “entire wind”). Little mass is accreted in the 2D poloidal models because magnetic flux accumulates and fully (except through periodic reconnection events) suspends the inflow.

### 6.3 Energy Efficiency of Hole, Jet, and Winds

Table 5 shows the flow efficiency computed via Eq. (17) (see section 3.4), where  $\eta = \eta^{\text{EM}} + \eta^{\text{MAKE}}$  and  $\eta^{\text{MAKE}} = \eta^{\text{PAKE}} + \eta^{\text{EN}}$ . These efficiencies are computed at the horizon ( $\eta_H$ ), for the jet ( $\eta_j$ ), for the magnetized wind ( $\eta_{\text{mw}}$ ), and for the entire wind ( $\eta_w$ ). The winds are measured at  $r_i$  and  $r_o$  given above, while the jet is measured at  $r_o$ . The radial asymptotic efficiency is  $\eta_\infty \sim \eta_j + \eta_{\text{mw},o}$ , because



**Table 3.** Grid Cells across Half-Thickness at Horizon, Half-Thicknesses of Disk, and Location for Interfaces for Disk-Corona and Corona-Jet

ModelName	$N_{\theta,H}^d$	$\theta_H^d$	$\theta_5^d$	$\theta_{20}^d$	$\theta_{100}^d$	$\theta_{20}^t$	$\theta_H^{dc}$	$\theta_5^{dc}$	$\theta_{20}^{dc}$	$\theta_{100}^{dc}$	$\theta_H^{cj}$	$\theta_5^{cj}$	$\theta_{20}^{cj}$	$\theta_{100}^{cj}$
<b>A0.94BfN40</b>	10	0.061	0.17	0.53	0.66	1.4	0.089	0.22	1	1.4	0.089	0.3	1	1.4
A0.94BfN100c1	8.4	0.1	0.15	0.52	0.67	1.4	0.067	0.2	0.99	1.4	0.08	0.27	1	1.5
A0.94BfN100c2	6.5	0.08	0.16	0.52	0.67	1.4	0.057	0.21	1	1.4	0.069	0.29	1	1.5
A0.94BfN100c3	8.6	0.11	0.16	0.53	0.67	1.4	0.052	0.2	1	1.4	0.078	0.28	1.1	1.5
A0.94BfN100c4	9.5	0.12	0.14	0.52	0.67	1.4	0.043	0.2	0.99	1.5	0.067	0.26	1	1.5
A0.94BfN40c5*	2.2	0.015	0.2	0.51	0.67	1.5	0.026	0.23	1.1	1.5	0.03	0.25	1.1	1.5
<b>A-0.94BfN40HR</b>	10	0.061	0.16	0.53	0.66	1.4	0.078	0.22	1	1.4	0.08	0.3	1	1.4
A-0.94BfN30	10	0.13	0.23	0.53	0.67	1.4	0.096	0.27	1	1.4	0.1	0.43	1.1	1.5
A-0.5BfN30	3	0.043	0.28	0.51	0.66	1.3	0.03	0.14	0.87	1.4	0.039	0.22	1.1	1.5
A0.0BfN10	23	0.56	0.56	0.62	0.67	1.4	0.13	0.21	1.1	0	0.26	0.75	0	0
A0.5BfN30	4.3	0.059	0.31	0.53	0.67	1.3	0.036	0.13	0.9	1.4	0.047	0.23	1.1	1.5
A0.94BfN30	8.9	0.11	0.14	0.51	0.66	1.4	0.067	0.19	0.97	1.4	0.076	0.26	1	1.4
A0.94BfN30r	8.4	0.1	0.14	0.51	0.66	1.4	0.065	0.19	0.96	1.4	0.072	0.26	1	1.5
A0.94BpN100	9.3	0.12	0.16	0.51	0.65	1.4	0.09	0.21	0.96	1.4	0.1	0.29	1	1.4
A-0.94BtN10	24	0.58	0.63	0.66	0.66	1.1	0.47	0.23	0.00065	0	0.19	0.00049	0	0
A-0.5BtN10	23	0.57	0.61	0.64	0.65	0.99	0.57	0.4	0.03	0	0.21	0.00041	0	0
A0.0BtN10	23	0.59	0.63	0.66	0.66	1.1	0.58	0.45	0.02	0.00076	0.38	0.016	0	0
A0.5BtN10	23	0.6	0.64	0.66	0.67	1.2	0.59	0.56	0.15	0.00038	0.54	0.22	0.019	0
A0.94BtN10	23	0.53	0.63	0.66	0.65	1.1	0.5	0.38	0.16	0.026	0.4	0.13	0.055	0
<b>A0.94BtN10HR</b>	47	0.57	0.64	0.67	0.66	1.2	0.6	0.63	0.44	0.62	0.59	0.41	0.29	0.034
MB09D	5.5	0.1	0.21	0.25	0.55	0.3	0.11	0.55	0.68	0.63	0.31	0.76	1.1	1.3
MB09Q	12	0.21	0.3	0.36	0.37	0.4	0.28	0.54	0.58	0.62	0.78	1.2	1.3	1.1
A-0.9N100	13	0.17	0.17	0.3	0.46	0.42	0.17	0.16	0.41	0.51	0.2	0.34	0.92	1.3
A-0.5N100	6.1	0.08	0.13	0.28	0.47	0.46	0.094	0.12	0.36	0.53	0.11	0.25	0.86	1.3
A-0.2N100	3.5	0.048	0.1	0.25	0.48	0.43	0.055	0.08	0.32	0.63	0.066	0.18	0.85	1.3
A0.0N100	4.4	0.06	0.13	0.29	0.48	0.47	0.06	0.11	0.32	0.6	0.076	0.23	0.91	1.4
A0.1N100	4.9	0.066	0.13	0.3	0.51	0.47	0.053	0.097	0.31	0.45	0.072	0.22	0.88	1.3
A0.2N100	4.2	0.057	0.12	0.29	0.49	0.51	0.053	0.1	0.3	0.25	0.068	0.21	0.82	1.3
A0.5N100	3	0.042	0.11	0.26	0.51	0.46	0.041	0.1	0.32	0.36	0.055	0.21	0.79	1.3
A0.9N25	5.2	0.068	0.15	0.33	0.46	0.74	0.068	0.15	0.36	0.53	0.081	0.27	0.83	1.3
A0.9N50	5.9	0.077	0.17	0.3	0.47	0.59	0.075	0.16	0.33	0.62	0.09	0.3	0.85	1.3
A0.9N100	5.3	0.07	0.16	0.29	0.47	0.51	0.068	0.16	0.31	0.44	0.083	0.29	0.86	1.3
A0.9N200	5.2	0.068	0.15	0.3	0.44	0.49	0.066	0.15	0.39	0.55	0.08	0.29	0.87	1.3
<b>A0.99N100</b>	8.2	0.11	0.19	0.33	0.45	0.59	0.1	0.2	0.38	0.56	0.11	0.34	0.88	1.3

these are unbound outflows with roughly constant  $\eta$  by the measured radius. BH and jet efficiencies are shown decomposed into EM, MAKE, PAKE, and EN terms. The radiative efficiency ( $\eta_{NT}$ ) for the Novikov-Thorne (NT) model is shown for comparison.

Many models with  $|a/M| \gtrsim 0.9$  show greater than 100% efficiency (and up to about 300% for the 3D models) for the BH energy extraction and jet at larger radii. This is much higher than the efficiencies of order the NT efficiency seen in other 3D GRMHD simulations that start off with limited poloidal magnetic flux (e.g. Hawley & Krolik 2006). In the thick disk models, the MAKE efficiency is negative even though the particle term ( $\eta_H^{PAKE} \sim -\rho_0 u_i$ ) is positive. This negative  $\eta_H^{MAKE}$  is due to a high specific enthalpy (i.e.  $\eta_H^{EN} \propto (u_g + p_g)/\rho_0 \gtrsim 1$ ). The negative  $\eta_H^{MAKE}$  means the BH is accreting thermo-kinetically unbound material as can occur in a Bondi flows or does occur in ADAFs (Narayan & Yi 1994). For the thick disk models, part of the negative  $\eta_H^{MAKE}$  is due the initial torus being marginally unbound, which contributes  $\sim -26\%$  to  $\eta_H^{MAKE}$ .

The dependence upon initial  $\beta$  is relatively weak for the thick disk models.  $\beta$  varies by factors of 2–3, while the efficiency  $\eta \propto B_r^2$  varies by much less than factors of 2–3 expected if the initial

$\beta \propto 1/B_r^2$  completely controlled the flux on the BH.  $\Upsilon \propto B_r$  (discussed later) shows even less dispersion vs. initial  $(\beta)^{-1/2}$ . Similar insensitivity to initial  $\beta$  is seen in Igumenshchev et al. (2003).

Also, notice there are very similar results between the flipping and non-flipping poloidal field, which shows that the flipping models have plenty of constant polarity flux unlike the MB09D model.

The 2D axisymmetric simulations (for all thick disk poloidal cases, but only showing A0.94BfN40c5\* in tables) show relatively higher efficiencies than otherwise similar 3D models. Mass is not accreted except during infrequent penetrations of the magnetic barrier via magnetic reconnection.

Despite the presence of well-ordered poloidal field near the BH, we see no evidence for significant energy extraction by any ergospheric type disk threaded by magnetic flux that would convert spin energy to MA energy in the disk and then to EM energy out in the magnetic field (Punsly & Coroniti 1990) unlike suggested to be present sometimes in other simulations (Punsly et al. 2009). Such an effect would lead to  $\eta_H^{MAKE} \gg 0$  (i.e. outgoing MAKE energy on the horizon). For this effect to be dynamically important, one should find  $\eta_H^{MAKE} \gtrsim \eta_H^{EM}$ , while in all cases we find  $\eta_H^{MAKE} \ll \eta_H^{EM}$ .

**Table 4.** Rest-Mass Accretion and Ejection Rates

ModelName	$\dot{M}_H$	$\dot{M}_{in,i} - \dot{M}_H$	$\dot{M}_{in,o} - \dot{M}_H$	$\dot{M}_j$	$\dot{M}_{mw,i}$	$\dot{M}_{mw,o}$	$\dot{M}_{w,i}$	$\dot{M}_{w,o}$
<b>A0.94BfN40</b>	48	20	250	6.9	6.8	17	19	250
A0.94BfN100c1	37	16	170	6.2	4.6	14	15	170
A0.94BfN100c2	38	15	210	6.6	5.1	20	13	210
A0.94BfN100c3	39	17	200	6.5	6.3	20	15	190
A0.94BfN100c4	38	18	180	5.4	6.4	16	16	190
A0.94BfN40c5*	4	15	280	1.7	4.3	11	12	280
<b>A-0.94BfN40HR</b>	49	21	250	6.6	6.5	18	20	240
A-0.94BfN30	98	20	250	6.8	8.6	26	17	250
A-0.5BfN30	110	6.8	220	2e-6	0.53	7.2	3.8	220
A0.0BfN10	160	3.6	62	0	0.0049	0.033	5.1	100
A0.5BfN30	110	7.6	140	0	0.2	3.6	4.3	140
A0.94BfN30	41	18	160	7.6	6.4	21	15	150
A0.94BfN30r	41	17	170	5.7	6.4	19	15	160
A0.94BpN100	46	21	210	9.6	7.2	24	19	200
A-0.94BtN10	280	1.9	230	0	0.0044	1.7e-6	1	230
A-0.5BtN10	93	2.2	84	0	0.017	0.0007	2	86
A0.0BtN10	180	5	220	0	0.089	0.00083	4.1	220
A0.5BtN10	200	5.5	180	0	0.29	0.043	4.6	180
A0.94BtN10	190	16	420	0.00095	0.46	0.16	14	410
<b>A0.94BtN10HR</b>	330	-0.83	410	0.0085	1.6	0.59	9.6	440
MB09D	0.082	0.62	-0.016	0.0002	0.0011	0.015	0.77	0.35
MB09Q	0.94	0.65	0.13	3.1e-5	0.02	0.061	0.74	1.9
A-0.9N100	18	1.6	18	0.32	0.76	7.2	1.4	20
A-0.5N100	15	1.4	21	0.15	0.54	6.8	1.3	25
A-0.2N100	15	1.3	19	0.041	0.31	5.5	1.1	23
A0.0N100	17	1.3	14	0.015	0.4	6.7	1.2	19
A0.1N100	14	1.3	14	0.028	0.36	5.7	1.2	19
A0.2N100	15	1.3	14	0.063	0.35	5.8	1.2	19
A0.5N100	13	1.8	16	0.27	0.72	8	1.7	21
A0.9N25	13	4.3	20	0.8	2.2	15	3.7	22
A0.9N50	16	5.6	23	0.88	3	16	4.9	25
A0.9N100	11	3.9	21	0.61	2	11	3.5	24
A0.9N200	7.5	2.8	16	0.5	1.5	8.6	2.4	17
<b>A0.99N100</b>	9.8	3.7	14	0.4	2.2	11	3.3	16

except MB09 models give  $\eta_H^{\text{MAKE}} \gtrsim \eta_H^{\text{EM}}$ . However, in the MB09 models all of that horizon MAKE energy is dissipated in the disk. So in all cases, the jet power is dominated by the EM term, i.e.  $\eta_H^{\text{EM}} \sim \eta_j$ . In summary, we find that the energy reaching large radii is dominated by the EM power produced via the magnetic flux penetrating the horizon as in the BZ mechanism.

#### 6.4 Energy Efficiency of Magnetized and Entire Winds

Table 6 is similar to Table 5, but the magnetized wind (“mw”) and entire wind (“w”) efficiencies (both EM and MAKE decompositions) are shown as evaluated at  $r_i$  and  $r_o$  given earlier. The BH and jet are dominated by EM power, the magnetized wind has EM power similar to MAKE power, and the wind is dominated by MAKE power (especially at larger radii). The magnetized wind, which can reach large radii, is fairly efficient in the poloidal models. However, the efficiency is much less than the BH and jet efficiency. So the BH dominates the disk’s magnetized wind, unlike in some models (Ghosh & Abramowicz 1997; Livio et al. 1999).

#### 6.5 Angular Momentum Flux for Hole, Jet, and Winds

A table (not shown) similar to Table 5, except for the specific angular momentum flux (as computed via the third row of Eq. (14)), shows that the poloidal field models have net extraction of angular momentum from the BH. The jet carries most of the angular momentum and most of that is in EM form. The toroidal field models have small angular momentum flux because no steady magnetized winds or jets emerge. A table (not shown) similar to Table 6, except for the specific angular momentum flux, shows that the wind’s angular momentum flux follows our prior discussions for the efficiency of the winds, except that the EM term tends to dominate the MA term for the magnetized wind.

#### 6.6 Spin-Up Parameter

Table 7 is similar to Table 5 except the BH spin-up parameter is computed via Eq. (18), where  $s = s^{\text{EM}} + s^{\text{MA}}$  and  $s^{\text{MA}} = s^{\text{PA}} + s^{\text{EN}}$ . One can recover the specific angular momentum flux from this spin-up parameter and efficiency given in Table 5. The thick disk

**Table 5.** Percent Energy Efficiency: BH, Jet, Winds, and NT

ModelName	$\eta_H$	$\eta_H^{\text{EM}}$	$\eta_H^{\text{MAKE}}$	$\eta_H^{\text{PAKE}}$	$\eta_H^{\text{EN}}$	$\eta_j$	$\eta_j^{\text{EM}}$	$\eta_j^{\text{MAKE}}$	$\eta_{\text{mw},o}$	$\eta_{w,o}$	$\eta_{\text{NT}}$
<b>A0.94BfN40</b>	235	264	-29.2	63.4	-92.5	242	228	13.5	27.9	-6.48	17.9
A0.94BfN100c1	323	379	-56.1	83.1	-139	333	322	11	26.4	-7.21	17.9
A0.94BfN100c2	298	340	-42.3	74.2	-116	304	293	11.3	34.1	-4.45	17.9
A0.94BfN100c3	295	337	-41.7	74.3	-116	299	288	10.7	35.5	-2.95	17.9
A0.94BfN100c4	323	368	-44.1	73.2	-117	323	313	9.44	31.6	4.21	17.9
A0.94BfN40c5*	1170	1240	-65.5	86.4	-152	945	925	19.9	109	205	17.9
<b>A-0.94BfN40HR</b>	244	274	-30.4	64.3	-94.7	251	238	12.1	27.5	-7.01	3.85
A-0.94BfN30	87.8	122	-34.3	73.7	-108	101	95.3	5.38	15.6	-12.6	3.85
A-0.5BfN30	-13.2	39.4	-52.7	100	-153	-1.51	3.27	-4.78	1.15	-13.7	4.51
A0.0BfN10	-17	-0.114	-16.9	24.1	-41	0	0	0	-5.94	-12.2	5.72
A0.5BfN30	-17.1	38.8	-55.9	85.8	-142	-0.796	5.59	-6.38	-6.9	-18	8.21
A0.94BfN30	353	420	-67.1	88.6	-156	361	348	12.8	32.6	-11.4	17.9
A0.94BfN30r	323	386	-62.7	86.3	-149	334	326	8.37	26.1	-14.4	17.9
A0.94BpN100	238	291	-52.8	83.8	-137	241	220	20.5	40.6	1.94	17.9
A-0.94BtN10	-17.8	-0.703	-17.1	24.7	-41.8	0	0	0	-9e-7	-17.6	3.85
A-0.5BtN10	-13.6	-0.287	-13.3	19.8	-33.1	0	0	0	-7e-5	-13.2	4.51
A0.0BtN10	-18.7	-0.077	-18.7	21.9	-40.6	0	0	0	-0.006	-18.7	5.72
A0.5BtN10	-19.2	-0.246	-19	26.8	-45.8	0	0	0	-0.018	-19	8.21
A0.94BtN10	-22.8	-0.162	-22.7	33.2	-55.9	0.0008	0.0004	0.0004	0.033	-23.4	17.9
<b>A0.94BtN10HR</b>	-28.2	-0.569	-27.6	8.71	-36.3	0.007	0.006	0.002	0.032	-19.5	17.9
MB09D	14.4	3.08	11.4	24.9	-13.5	2.96	2.7	0.269	0.485	-0.739	16.7
MB09Q	5.19	0.199	4.99	22.9	-17.9	0.008	0.004	0.003	0.431	0.576	17.9
A-0.9N100	32.3	39.8	-7.51	74.6	-82.2	23.4	20.8	2.61	8.49	9.59	3.9
A-0.5N100	17.2	11.4	5.77	41.7	-36	9.4	8.69	0.706	7.18	8.03	4.51
A-0.2N100	6.64	0.906	5.73	34.5	-28.8	1.12	1.04	0.079	4.78	5.38	5.15
A0.0N100	4.51	-0.884	5.4	33.7	-28.3	0.052	0.035	0.017	3.78	4.23	5.72
A0.1N100	5.04	-0.242	5.29	32.4	-27.1	0.342	0.292	0.051	4.16	4.5	6.06
A0.2N100	7.34	1.89	5.46	34.9	-29.4	1.73	1.64	0.088	5.04	5.38	6.46
A0.5N100	30.8	24.3	6.48	38.1	-31.6	19.6	18.3	1.25	10.3	10.8	8.21
A0.9N25	113	112	1.46	53.3	-51.8	88.8	80.3	8.55	24.1	25.7	15.6
A0.9N50	102	99.3	2.91	51.3	-48.3	77.7	70.3	7.47	24.4	24.8	15.6
A0.9N100	101	97.2	4.19	50	-45.8	77.6	70.1	7.44	24.1	24.7	15.6
A0.9N200	121	117	4.28	52	-47.7	96.1	87.5	8.67	25.1	26	15.6
<b>A0.99N100</b>	130	127	2.89	64.4	-61.5	103	95.5	7.41	26.4	27	26.4

poloidal models have a spin-up parameter that is extremely negative relative to  $a/M$ , unlike the NT thin disk and MB09 models. The BH is always rapidly spinning down in absolute spin magnitude for all models except the MB09D and the A0.5BtN10 toroidal field model. In all cases, the  $a/M = 0$  models are spinning up, although quite weakly with the model A0.0BfN10 as compared to models A0.0BtN10 and A0.0N100. In summary, the thermal pressure and magnetic field are capable of greatly decreasing the BH's spin.

### 6.7 $\alpha$ Viscosity and Suppression of the MRI

Table 8 shows the  $\alpha$  viscosity parameters computed via Eq. (29) using various averaging as described below Eq. (29) in section 3.7, where  $\alpha_a$  includes the flow with  $b^2/\rho_0 < 1$  and  $\alpha_b$  focuses on the highest density parts of the disk flow by using averaging weight  $w = \rho$ .  $\alpha$  is averaged over  $r = 12\text{--}20r_g$  for all models except MB09 models that are averaged from  $r = 10\text{--}12r_g$ . If a component's contribution to  $\alpha$  is less than 10%, then we set that component to  $\sim 0$  in the table. Also provided is  $Q_{p,\text{cor}}$  ( $p = n, l, m$ ) com-

puted via Eq. (44) for quantities  $\rho_0$  and  $b^2$  at  $r = 8r_g$  for the “Disk” component. We also show  $Q_{\theta,\text{MRI}}$ ,  $Q_{\phi,\text{MRI}}$ , and  $S_{d,\text{MRI}}$  at  $r_i^{\text{dcden}}$  and  $r_o^{\text{dcden}}$  given in Table 10 as computed via Eq. (43) and Eq. (33). The convergence quality measures ( $\alpha_{\text{mag}}$ ,  $Q_{nlm,\text{cor}}$ ,  $Q_{\theta,\text{MRI}}$ , and  $Q_{\phi,\text{MRI}}$ ) are discussed in section 6.10. The radius ( $r_{S_{d,\text{MRI}}=1/2}$  – first occurrence of  $S_{d,\text{MRI}} = 1/2$  outside  $4r_g$  and up to a one inflow radius) within which the MRI is suppressed is provided, where “-” indicates that  $S_{d,\text{MRI}} > 1/2$  implying no strong MRI suppression.  $S_{d,\text{MRI}}$  and  $S_{d,\text{weak,MRI}}$  (focusing more on heavy disk) give similar results.

The radially-averaged  $\alpha$  depends upon the accumulated magnetic flux, disk thickness, and BH spin. Within the high-density disk, the thick disk poloidal field models have  $|\alpha_b| \sim 0.02$ , thick disk toroidal field models have  $\alpha_b \sim 0.05\text{--}0.07$ , and thinner disk poloidal field models have  $\alpha_b \sim 0.05\text{--}0.2$ . Our thick toroidal field models have higher  $\alpha$  than found in other works for which the MRI is not suppressed, such as  $\alpha \sim 0.025$  found by Beckwith et al. (2011). Also, (not shown)  $\alpha_a > \alpha_b$ , so the less dense and higher magnetized corona has larger  $\alpha$  as expected. MB09D, that has decaying turbulence, has  $\alpha_b \sim 0.01$ .

$\alpha$  and  $\alpha_{\text{eff}}$  are often quite different for our new thick/thinner

**Table 6.** Percent Energy Efficiency: Magnetized Wind and Entire Wind

ModelName	$\eta_{mw,i}$	$\eta_{mw,i}^{EM}$	$\eta_{mw,i}^{MAKE}$	$\eta_{mw,o}$	$\eta_{mw,o}^{EM}$	$\eta_{mw,o}^{MAKE}$	$\eta_{w,i}$	$\eta_{w,i}^{EM}$	$\eta_{w,i}^{MAKE}$	$\eta_{w,o}$	$\eta_{w,o}^{EM}$	$\eta_{w,o}^{MAKE}$
<b>A0.94BfN40</b>	7.49	5.9	1.59	27.9	13	14.9	-20.1	6.66	-26.8	-6.48	13.5	-20
A0.94BfN100c1	8.89	6.5	2.39	26.4	12.3	14.2	-19.9	7.24	-27.1	-7.21	8.16	-15.4
A0.94BfN100c2	9.39	7.36	2.03	34.1	14.6	19.5	-18.3	8.14	-26.5	-4.45	9.99	-14.4
A0.94BfN100c3	11.6	8.07	3.57	35.5	15.4	20.1	-17.8	8.82	-26.6	-2.95	11.6	-14.5
A0.94BfN100c4	11.9	6.98	4.92	31.6	14.8	16.8	-20	7.77	-27.8	4.21	12.3	-8.08
A0.94BfN40c5*	-4.03	15.4	-19.5	109	43.6	64.9	-33.6	15.9	-49.5	205	42.7	163
<b>A-0.94BfN40HR</b>	8.47	5.57	2.9	27.5	12.6	14.9	-20.4	6.44	-26.9	-7.01	13.1	-20.1
A-0.94BfN30	3.36	3.71	-0.346	15.6	7.55	8.01	-19	4.04	-23	-12.6	7.62	-20.2
A-0.5BfN30	-1.19	2.1	-3.29	1.15	6.48	-5.33	-13.2	2.19	-15.4	-13.7	6.06	-19.7
A0.0BfN10	-13.3	0.068	-13.4	-5.94	0.087	-6.03	-16.8	0.087	-16.9	-12.2	0.26	-12.4
A0.5BfN30	-3.82	1.54	-5.37	-6.9	3.92	-10.8	-14.8	1.42	-16.2	-18	4.09	-22.1
A0.94BfN30	11.2	7.26	3.9	32.6	15.4	17.2	-19.7	7.89	-27.6	-11.4	16.7	-28.1
A0.94BfN30r	9.03	6.62	2.41	26.1	11.9	14.2	-21	7.14	-28.1	-14.4	13.3	-27.7
A0.94BpN100	10.8	7.24	3.52	40.6	18.4	22.2	-16.9	8.23	-25.1	1.94	20.6	-18.7
A-0.94BtN10	-0.164	-0.017	-0.147	-9e-7	-2e-7	-7e-7	-17.6	-0.148	-17.4	-17.6	0.019	-17.7
A-0.5BtN10	-0.392	-0.014	-0.378	-7e-5	-3e-5	-4e-5	-13.5	-0.081	-13.4	-13.2	0.04	-13.2
A0.0BtN10	-0.457	0.026	-0.483	-0.006	-9e-5	-0.006	-18.7	0.054	-18.8	-18.7	0.057	-18.7
A0.5BtN10	-1.36	0.077	-1.44	-0.018	0.003	-0.022	-19	0.098	-19.1	-19	0.072	-19.1
A0.94BtN10	-0.413	0.09	-0.503	0.033	0.012	0.021	-22.9	0.109	-23	-23.4	0.113	-23.5
<b>A0.94BtN10HR</b>	-1.66	0.162	-1.83	0.032	0.04	-0.008	-23.1	0.187	-23.3	-19.5	0.177	-19.7
MB09D	3.15	3.42	-0.271	0.485	1.28	-0.792	5.99	6.18	-0.184	-0.739	1.36	-2.09
MB09Q	2.49	1.65	0.839	0.431	0.985	-0.555	4.84	2.17	2.67	0.576	1.14	-0.567
A-0.9N100	3.97	2.26	1.71	8.49	3.72	4.77	5.41	2.28	3.12	9.59	3.85	5.75
A-0.5N100	3.57	2.05	1.52	7.18	3.39	3.78	5.3	2.07	3.23	8.03	3.51	4.52
A-0.2N100	2.85	1.54	1.32	4.78	2.52	2.26	4.82	1.56	3.26	5.38	2.61	2.77
A0.0N100	2.88	1.67	1.21	3.78	2.37	1.41	4.5	1.7	2.79	4.23	2.45	1.78
A0.1N100	2.97	1.73	1.24	4.16	2.78	1.38	4.56	1.75	2.81	4.5	2.82	1.69
A0.2N100	3.42	2.09	1.32	5.04	3.42	1.63	4.94	2.1	2.83	5.38	3.49	1.89
A0.5N100	5.77	4.3	1.47	10.3	6.85	3.46	7.45	4.33	3.12	10.8	6.95	3.83
A0.9N25	9.8	7.01	2.79	24.1	12.2	11.9	11.7	7.09	4.66	25.7	12.3	13.4
A0.9N50	10.6	7.86	2.78	24.4	13.1	11.3	13	7.94	5.03	24.8	13.1	11.7
A0.9N100	11	8.21	2.84	24.1	13.3	10.8	13.4	8.27	5.13	24.7	13.4	11.3
A0.9N200	11.4	9.09	2.26	25.1	14.3	10.8	13	9.22	3.73	26	14.5	11.5
<b>A0.99N100</b>	11.8	8.69	3.08	26.4	13.8	12.5	13.6	8.79	4.85	27	14	13

poloidal field models and thick toroidal field models, which shows that local viscous  $\alpha$ -disk theory is inaccurate. For the poloidal field models,  $\alpha$ -disk theory fails for  $r \lesssim 10r_g$  due to disk compression (leading to smaller  $\theta^d$  than a hydrostatic solution would have) by magnetic flux. Even at larger radii within the inflow equilibrium region where  $\theta^d$  is not compressed much by magnetic flux,  $\alpha$ -disk theory still does poorly. Using  $\alpha_b \propto p_b$  leads to somewhat better agreement for some of the poloidal field models. The overall lack of agreement shows that large-scale magnetic torques through magnetic confinement (rather than direct magnetic torques within the heavy inflow) play an important role. Convection may also play an important role. For the toroidal field models, using  $\alpha_b \propto p_{tot}$  gives a radial scaling for  $v_{visc}$  similar to  $v_r$  but too small by a factor of  $\sim 10$ , while  $\alpha_b \propto p_b$  gives far too large  $v_{visc}$  compared to  $v_r$ . Summarizing, in all our new models, using  $p_{tot}$  leads to too small  $v_r = v_{visc}$  despite often having a reasonable radial scaling. Our poloidal and toroidal field simulations have  $\alpha_{eff} \sim 0.2$ –1 (which indicates the actual effective viscous timescale) that is large enough to be consistent with observations (King et al. 2007).

By contrast, the same table diagnostics for the multi-field loop

thin ( $\theta^d \sim 0.07$ ) disk model A0HR07 in Penna et al. (2010) give  $\alpha_b \sim \alpha_{b,eff} \sim 0.04$  for  $r = 7$ – $9r_g$ , so  $\alpha$ -disk theory works quite well for those multi-loop field thin disk models. Also, for  $\theta^d \sim 0.07$ , Beckwith et al. (2011) found  $\alpha \sim 0.025$  and  $\alpha_{eff} \sim 0.1$  (from their fig. 8 around  $r \sim 10r_g$  where  $G \approx 2$ ), so  $\alpha$ -disk theory is holding (at best) marginally well. The tables show that our older MB09 models show reasonable agreement with  $\alpha$ -disk theory.

$\alpha_{b,M2}$  dominates the local stress contribution to  $\alpha_b$  in many cases. Note that averaging  $|\alpha_{mag}|$  gives values of  $\sim 0.4$ – $0.6$  for all our simulations (including 2D models), but that neglects the direction of angular momentum transport. The PA (the Reynolds stress) term can be computed as  $\alpha_{PA} \approx \alpha - \alpha_{M2}$  from the table since other terms are small. Interestingly,  $\alpha_b$ ,  $\alpha_{b,M2}$ , and  $\alpha_{b,mag}$  are negative for  $a/M \leq 0$  for the thick disk poloidal field models, and such models even have  $v_{rot}$  the same sign as  $a/M$  (i.e. flow reversal) in the heavy disk inflow even out to  $r \sim 40r_g$  (e.g. in model A-0.94BfN30). This flow reversal behavior was validated by restarting the A0.94BfN40 model at  $t = 8000r_g/c$  with  $a/M = -0.9375$  that produced model A-0.94BfN40HR. (Compared to A-0.94BfN30, A-0.94BfN40HR shows much less variance in time-dependent quantities – proba-



Table 7. Spin-Up Parameter: BH, Jet, Winds, and NT

ModelName	$s_H$	$s_H^{EM}$	$s_H^{MA}$	$s_H^{PA}$	$s_H^{EN}$	$s_j$	$s_j^{EM}$	$s_j^{MA}$	$s_{mw,o}$	$s_{w,o}$	$s_{NT}$
<b>A0.94BfN40</b>	-23.5	-21.1	-2.37	-0.609	-1.76	-19.5	-16.8	-2.65	-3.1	-4.03	0.411
A0.94BfN100c1	-28	-25	-3.01	-0.27	-2.74	-22.6	-20.3	-2.31	-3.47	-5.67	0.411
A0.94BfN100c2	-26.6	-23.6	-2.95	-0.478	-2.47	-21.1	-18.6	-2.44	-3.45	-2.92	0.411
A0.94BfN100c3	-25.7	-22.7	-2.97	-0.484	-2.48	-20.2	-17.8	-2.43	-4.23	-4.44	0.411
A0.94BfN100c4	-26.8	-24.1	-2.75	-0.468	-2.29	-20.8	-18.4	-2.34	-3.11	-6	0.411
A0.94BfN40c5*	-111	-105	-6.41	-0.747	-5.66	-107	-103	-4.75	-11.6	-67.1	0.411
<b>A-0.94BfN40HR</b>	23.5	21.1	2.31	0.573	1.74	19.4	16.9	2.49	3.19	7.76	6
A-0.94BfN30	11.4	9.54	1.89	0.264	1.63	8.81	6.67	2.14	2.55	5.01	6
A-0.5BfN30	12.7	11.5	1.23	-0.144	1.37	5.62	4.91	0.714	6.97	8.5	4.84
A0.0BfN10	0.013	0.032	-0.019	-0.009	-0.009	-0	-0	-0	0.061	0.404	3.46
A0.5BfN30	-11.5	-10.2	-1.3	-0.005	-1.3	-5.15	-4.55	-0.599	-6.54	-8.05	1.98
A0.94BfN30	-30.6	-27.5	-3.08	-0.162	-2.92	-25	-22.3	-2.62	-4.06	-10.3	0.411
A0.94BfN30r	-28.9	-25.9	-3	-0.205	-2.79	-23.1	-20.7	-2.45	-3.63	-8.54	0.411
A0.94BpN100	-25	-22.3	-2.72	-0.214	-2.5	-21.3	-18.7	-2.56	-5.07	-5.97	0.411
A-0.94BtN10	3.29	0.205	3.09	1.98	1.11	1.88	0	1.88	1.88	3.2	6
A-0.5BtN10	2.39	0.103	2.29	1.61	0.678	1	0	1	1	2.18	4.84
A0.0BtN10	1.15	0.004	1.15	0.751	0.396	-0	-0	-0	0.0004	1.06	3.46
A0.5BtN10	-0.639	-0.297	-0.342	-0.208	-0.134	-1	-0	-1	-1	-0.793	1.98
A0.94BtN10	-1.53	-0.232	-1.3	-0.716	-0.584	-1.88	-0.0003	-1.87	-1.88	-1.63	0.411
<b>A0.94BtN10HR</b>	-2.04	-0.316	-1.72	-1.38	-0.336	-1.88	-0.002	-1.87	-1.88	-2.33	0.411
MB09D	-0.204	-0.069	-0.135	-0.039	-0.096	-1.99	-0.137	-1.85	-8.63	-15.3	0.492
MB09Q	0.103	-0.046	0.149	0.132	0.017	-1.88	-0.0005	-1.87	-5.39	-7.63	0.411
A-0.9N100	5.92	3.17	2.75	0.896	1.86	3.03	1.15	1.88	-0.151	3.52	5.9
A-0.5N100	5.28	3.63	1.65	1.03	0.625	2.61	1.54	1.06	-0.819	1.52	4.84
A-0.2N100	3.4	2.19	1.21	0.816	0.399	1.17	0.765	0.404	-0.761	0.879	4.02
A0.0N100	1.03	0.004	1.03	0.726	0.304	-0.045	-0.045	-0.0004	-3.19	-0.6	3.46
A0.1N100	-0.546	-1.03	0.481	0.339	0.141	-0.649	-0.448	-0.201	-3.91	-2.35	3.18
A0.2N100	-1.53	-1.98	0.451	0.323	0.128	-1.37	-0.954	-0.418	-4.28	-2.41	2.89
A0.5N100	-5.05	-5.15	0.099	0.096	0.002	-4.43	-3.27	-1.16	-6.39	-4	1.98
A0.9N25	-8.5	-7.31	-1.18	-0.511	-0.674	-6.5	-4.33	-2.17	-7.77	-4.49	0.58
A0.9N50	-7.46	-6.44	-1.01	-0.45	-0.565	-6.05	-3.9	-2.15	-8.34	-4.72	0.58
A0.9N100	-7.28	-6.35	-0.925	-0.429	-0.496	-6.05	-3.92	-2.13	-8.74	-5.41	0.58
A0.9N200	-8.64	-7.57	-1.07	-0.477	-0.591	-7.24	-4.98	-2.26	-10.1	-4.42	0.58
<b>A0.99N100</b>	-6.8	-5.57	-1.22	-0.394	-0.828	-5.51	-3.34	-2.16	-9.7	-4.57	0.111

bly due to lower-resolution models allowing some of the opposite polarity magnetic flux to reach the BH causing, e.g., the time-averaged  $\eta_H$  to be smaller.) Recall that  $\alpha_{mag} \propto -b_r b_\phi$ , which is just a term related to the Poynting flux. Evidently, BH angular momentum is being dumped even into the heavy disk. Yet, in all cases, mass continues to accrete due to large-scale stresses by magnetic flux and also possibly due to convection. Interestingly, the thick disk toroidal field models are dominated by positive  $\alpha_{b,PA}$  (Reynolds stress). The thick disk  $a/M = 0$  poloidal field model A0.0BfN10 has non-negligible negative  $\alpha_{b,PA}$ . Also, some of the thinner disk poloidal field models have (negative) Reynolds stress that is up to 50% of  $|\alpha_{b,M2}|$ .  $\alpha_{b,EN}$  contributes little to  $\alpha_b$ , except for the thick disk toroidal field models for which  $\alpha_{b,EN} \lesssim \alpha_{b,M2}$ , both at about 20% contribution to the total  $\alpha$ .

The MRI is not suppressed ( $S_{d,MRI} \gtrsim 1$ ) for thick disks at low spin, flows with initially toroidally-dominated field, or MB09 type limited poloidal flux or quadrupolar field models. However, for poloidal field models where magnetic flux saturates, the MRI is suppressed within  $r_{S_{d,MRI}=1/2} \sim 20\text{--}200r_g$  for many thick disk models and within  $r_{S_{d,MRI}=1/2} \sim 20r_g$  for the thinner disk models

(the radius depends upon the initial  $\beta$  and duration of simulation). The MRI is suppressed in the A0.0BfN10 model as due to the small initial  $\beta$  and much of the magnetic field staying in the dense flow (instead of a jet) where  $S_{d,MRI}$  is measured.

The suppression of the MRI is due to both the field strength and the angular velocity. The thinner disk models have accumulated much magnetic flux near the BH as most evident from Figure 19 (similar to Figure 6) showing the time-averaged flow-field for A0.99N100. This suggests that thinner disks accrete (or hold onto) magnetic flux as easily as thicker disks. However, the thick flows are more sub-Keplerian, as evident when computing  $S_{d,MRI}$  using  $\Omega_{rot} \rightarrow \Omega_K$ . Then, the thinner models would still have  $r_{S_{d,MRI}=1/2} \sim 20r_g$  because they are somewhat Keplerian, while the thick models would have  $r_{S_{d,MRI}=1/2} \sim 8r_g$ . The MB09Q and toroidal field models have  $S_{d,MRI} \sim \text{few}$  because poloidal flux build-up is competing against its destruction since there is no net flux except in small patches. Our high resolution toroidal field model shows smaller  $S_{d,MRI}$ , so even higher resolutions might lead to  $S_{d,MRI} \sim 0.3$  as in the poloidal field models. MB09D probably has  $S_{d,MRI} \sim 8$  simply because turbulence is under-resolved.

**Table 8.** Viscosities, Grid Cells per Correlation lengths and MRI Wavelengths, MRI Wavelengths per full Disk Height, and Radii for MRI Suppression

ModelName	$\alpha_{b,\text{eff}}$	$\alpha_b$	$\alpha_{b,M2}$	$\alpha_{b,\text{mag}}$	$Q_{n,\text{cor.}}$ $[\nu_0, b^2]$	$Q_{l,\text{cor.}}$ $[\nu_0, b^2]$	$Q_{m,\text{cor.}}$ $[\nu_0, b^2]$	$Q_{\theta,\text{MRI},[i,o]}$	$Q_{\phi,\text{MRI},[i,o]}$	$S_{d,\text{MRI},[i,o]}$	$r_{[S_d, S_{d,\text{weak}}]}$ MRI=1/2
<b>A0.94BfN40</b>	0.39	0.022	0.02	0.26	22, 21	6, 12	19, 18	110, 120	380, 540	0.33, 0.34	> 55, > 55
A0.94BfN100c1	0.35	0.029	0.029	0.36	13, 13	4, 7	12, 11	56, 53	210, 220	0.29, 0.38	64, 44
A0.94BfN100c2	0.3	0.029	0.028	0.3	13, 13	4, 7	6, 6	48, 61	98, 100	0.38, 0.34	> 44, > 44
A0.94BfN100c3	0.32	0.03	0.026	0.31	14, 13	4, 7	3, 3	54, 62	47, 59	0.31, 0.33	47, 42
A0.94BfN100c4	0.29	0.022	0.018	0.24	13, 13	3, 8	2, 2	36, 48	24, 31	0.47, 0.43	14, 72
A0.94BfN40c5*	0.089	0.0053	0.0032	0.051	22, 19	3, 22	1, 1	1300, 660	1, 1	0.025, 0.058	55, 60
<b>A-0.94BfN40HR</b>	0.088	-0.017	-0.017	-0.24	22, 21	6, 12	20, 18	110, 140	380, 560	0.36, 0.29	> 54, > 54
A-0.94BfN30	0.12	-0.04	-0.031	-0.37	15, 13	4, 7	10, 9	42, 45	180, 260	0.44, 0.46	210, 190
A-0.5BfN30	0.2	-0.11	-0.11	-0.65	13, 13	5, 6	15, 16	35, 23	200, 290	0.5, 0.91	-, -
A0.0BfN10	0.77	-0.012	~ 0	-0.011	15, 15	12, 8	13, 13	110, 120	110, 170	0.22, 0.19	> 88, > 88
A0.5BfN30	0.39	0.12	0.12	0.63	14, 13	3, 7	16, 19	47, 18	240, 270	0.39, 1.2	18, 18
A0.94BfN30	0.36	0.024	0.022	0.25	13, 13	3, 7	12, 12	35, 28	210, 370	0.46, 0.75	13, 23
A0.94BfN30r	0.28	0.024	0.023	0.19	13, 13	3, 6	12, 12	31, 34	190, 330	0.52, 0.6	11, 13
A0.94BpN100	0.45	0.028	0.024	0.3	13, 13	4, 8	12, 11	51, 100	180, 270	0.32, 0.19	130, 100
A-0.94BtN10	0.14	0.053	~ 0	0.4	15, 13	17, 10	20, 6	19, 10	40, 32	1.4, 2.7	-, -
A-0.5BtN10	0.17	0.096	0.01	0.38	15, 13	18, 10	20, 7	23, 12	48, 40	1.2, 2.1	-, -
A0.0BtN10	0.24	0.06	0.016	0.47	15, 13	17, 9	20, 8	19, 15	61, 64	1.5, 1.7	-, -
A0.5BtN10	0.48	0.067	0.022	0.44	15, 15	15, 12	15, 9	31, 23	87, 83	0.9, 1.1	-, -
A0.94BtN10	0.4	0.062	0.0072	0.34	14, 14	16, 11	19, 10	19, 16	58, 63	1.5, 1.7	-, -
<b>A0.94BtN10HR</b>	0.75	0.066	0.02	0.38	28, 25	29, 24	25, 18	71, 50	170, 170	0.8, 1	-, -
MB09D	0.014	0.01	0.0079	0.23	18, 14	4, 4	4, 3	3, 3	4, 4	7.5, 8.1	-, -
MB09Q	0.099	0.076	0.054	0.35	22, 19	12, 9	3, 3	11, 11	9, 9	3, 2.9	-, -
A-0.9N100	0.25	0.034	0.18	0.49	23, 22	9, 11	5, 5	110, 35	22, 21	0.29, 0.84	22, 20
A-0.5N100	0.51	0.067	0.19	0.48	32, 31	9, 9	4, 3	170, 33	25, 22	0.18, 0.84	25, 22
A-0.2N100	0.68	0.12	0.17	0.46	32, 29	8, 7	3, 3	140, 22	23, 21	0.21, 1.4	20, 18
A0.0N100	0.62	0.21	0.18	0.52	31, 29	9, 10	4, 3	110, 32	23, 21	0.28, 1.1	21, 18
A0.1N100	0.67	0.2	0.21	0.49	31, 31	9, 10	3, 3	140, 35	28, 23	0.23, 1	21, 19
A0.2N100	0.92	0.35	0.23	0.57	32, 31	8, 8	3, 3	150, 34	29, 22	0.21, 0.94	24, 23
A0.5N100	0.74	0.24	0.18	0.53	31, 28	3, 7	3, 3	90, 30	25, 20	0.32, 1.1	16, 15
A0.9N25	1.2	0.13	0.26	0.59	29, 27	8, 10	4, 4	160, 280	48, 45	0.21, 0.16	> 120, > 120
A0.9N50	0.96	0.16	0.21	0.55	28, 27	8, 10	3, 4	130, 88	30, 23	0.25, 0.4	34, 32
A0.9N100	0.92	0.17	0.21	0.54	29, 28	8, 10	4, 4	120, 42	30, 22	0.27, 0.79	23, 21
A0.9N200	0.53	0.18	0.15	0.46	27, 26	8, 9	3, 4	75, 24	26, 24	0.42, 1.5	14, 12
<b>A0.99N100</b>	0.83	0.2	0.2	0.53	22, 20	6, 8	7, 7	110, 67	66, 54	0.33, 0.56	26, 20

## 6.8 Magnetic Flux

Table 9 shows the value of  $\Upsilon$  (computed via the Eq. (26)) on the horizon ( $\Upsilon_H$ ), in the inflow-only ( $u_r < 0$ ) regions at  $r_i$  and  $r_o$  defined already ( $\Upsilon_{in,i}$  and  $\Upsilon_{in,o}$  respectively), in the jet ( $\Upsilon_j$ ), in the magnetized wind at  $r_i$  and  $r_o$  ( $\Upsilon_{mw,i}$  and  $\Upsilon_{mw,o}$  respectively), and in the entire wind at  $r_i$  and  $r_o$  ( $\Upsilon_{mw,i}$  and  $\Upsilon_{mw,o}$  respectively). Only  $\Upsilon_j$  uses the non-local normalization of  $\dot{M}_H$ .

In the poloidal field models,  $\Upsilon$  is dominated by the magnetic flux threading the BH polar regions as shown by comparing  $\Upsilon_H$  and  $\Upsilon_j$ . Also evident is that  $\Upsilon$  decreases from  $r_o$  to  $r_i$  (shown by  $\Upsilon_{in,o}$  and  $\Upsilon_{in,i}$ , respectively), but then rises near the horizon. The flux at large radii acts a reservoir. At smaller radii some flux gets accreted, and on the horizon much of the mass gets drained. This leaves the ordered part of the magnetic flux giving high  $\Upsilon_H$ .

The magnetized wind and entire wind values of  $\Upsilon$  are normalized by the local mass accretion rate for the inflow component at those radii (i.e.  $\dot{M}_{in,i}$  and  $\dot{M}_{in,o}$ ). This shows that the local mass-loading can be large in the wind and small in the magnetized wind.

The entire wind is just part of the overall circularizing flow and eventually feeds the pure inflow and feeds the inflow value of  $\Upsilon$ .

Also, notice that  $\Upsilon$  is quite similar between the flipping and non-flipping poloidal field, which shows that the flipping models have plenty of constant polarity flux unlike the MB09D model. This also shows that even with different initial conditions, the flux threading the BH saturates in some type of force balance between (e.g.) the inner magnetospheric pressure against the exterior disk gas+ram pressure. This unstable balance results in time-dependent magnetic Rayleigh-Taylor events that regulate the magnetic flux on the horizon by carrying magnetic flux back into the disk and wind.

Table 9 also shows the magnetic flux (computed as in section 3.6) on the horizon normalized in various ways. The values  $\Psi_H/\Psi_1(t=0)$ ,  $\Psi_H/\Psi_2(t=0)$ , and  $\Psi_H/\Psi_3(t=0)$  are for normalizations by the extrema (label of 1 for the extrema at smallest radii, and so forth) in the magnetic flux in the initial disk. For the flipping poloidal field geometry, we show only the first 3 extrema since only those are relevant over the entire evolution. A value of zero indicates no relevant value, as for the non-flipping poloidal field ge-

**Table 9.** Absolute Magnetic Flux per unit: Rest-Mass Fluxes, Initial Magnetic Fluxes, Available Magnetic Fluxes, and BH Magnetic Flux

ModelName	$\Upsilon_H$	$\Upsilon_{in,i}$	$\Upsilon_{in,o}$	$\Upsilon_j$	$\Upsilon_{mw,i}$	$\Upsilon_{mw,o}$	$\Upsilon_{w,i}$	$\Upsilon_{w,o}$	$\left  \frac{\Psi_H}{\Psi_1(t=0)} \right $	$\left  \frac{\Psi_H}{\Psi_2(t=0)} \right $	$\left  \frac{\Psi_H}{\Psi_3(t=0)} \right $	$\left  \frac{\Psi_H}{\Psi_a} \right $	$\left  \frac{\Psi_H}{\Psi_s} \right $	$\left  \frac{\Phi_H}{\Psi_H} \right $
<b>A0.94BfN40</b>	17	2.6	7.9	16	2.7	1.1	6.7	16	21	1	0.16	0.46	0.047	1
A0.94BfN100c1	18	2.6	14	17	2.9	2.7	6.8	28	31	1.5	0.24	0.65	0.065	1
A0.94BfN100c2	18	2.7	12	16	3.1	3	7.3	28	30	1.5	0.23	0.63	0.043	1
A0.94BfN100c3	18	2.6	14	16	3	2.3	6.8	29	31	1.5	0.25	0.7	0.063	1
A0.94BfN100c4	18	2.2	13	16	1.6	1.4	5.7	29	32	1.6	0.25	0.72	0.047	1
A0.94BfN40c5*	37	11	13	40	15	4.9	18	20	13	0.67	0.1	0.17	0.6	1
<b>A-0.94BfN40HR</b>	17	2.5	8.1	16	2.2	1.2	6.4	17	27	1.1	0.18	0.56	0.048	1
A-0.94BfN30	11	2.8	8.4	9.4	3.5	1.3	8.8	16	19	0.78	0.12	0.41	0.024	1
A-0.5BfN30	16	14	14	8.4	23	25	16	17	29	1.3	0.2	0.61	0.037	1
A0.0BfN10	8.9	9.7	15	0	1600	350	56	31	9.4	0.44	0.068	0.11	0.19	1.1
A0.5BfN30	15	14	14	8.3	45	35	17	16	24	1.1	0.18	0.5	1.6e-5	1
A0.94BfN30	19	2	7.8	18	2	0.98	5.6	15	17	0.84	0.13	0.36	1.3e-5	1
A0.94BfN30r	19	2.2	8.3	17	2.2	0.77	5.9	15	17	0.82	0.13	0.33	1.2e-5	1
A0.94BpN100	17	2.4	12	16	2.7	2.9	6	24	6.7e-5	0	0	1.3e-5	1.3e-5	1
A-0.94BtN10	0.74	0.93	1.2	0	21	0.11	16	2.6	6e3	3e2	3e2	0.46	0.27	4.3
A-0.5BtN10	1	1.3	1.6	0	19	0.85	9.1	3.1	8e3	1e2	11	0.55	0.4	4.5
A0.0BtN10	1.3	1.6	2.3	0	15	18	11	4.5	2e4	2e3	1.9	3.7	1.6	3.5
A0.5BtN10	2.1	2.7	3.1	0	30	14	18	6.7	4e3	2e2	1.9	13	0.57	3.5
A0.94BtN10	1.2	1.5	2	0.02	11	8.4	5.8	4.1	7e3	2e3	5e3	0.36	0.27	3.1
<b>A0.94BtN10HR</b>	2.1	2.7	3.1	0.1	14	8	15	6.7	4e4	1e4	4e3	4.4	3.2	3.8
MB09D	2.1	0.38	1	1.5	8	5.2	0.7	2.1	0.61	0	0	0.97	0.97	1
MB09Q	0.58	1.4	2.4	0.05	8.9	11	2.6	3.9	2e6	0	0	0.67	1.2	2.6
A-0.9N100	6.6	2.7	4.6	4.9	16	23	13	16	0.16	0	0	0.16	0.27	1.1
A-0.5N100	9.9	3.9	3.5	7.1	21	21	14	13	0.24	0	0	0.24	0.4	1.1
A-0.2N100	12	6.4	3.7	6.8	26	23	15	13	0.29	0	0	0.29	0.49	1
A0.0N100	11	8.1	8	5.1	24	24	15	17	0.29	0	0	0.29	0.47	1
A0.1N100	12	7.6	5.9	6.5	26	23	15	14	0.4	0	0	0.4	0.53	1
A0.2N100	12	5.9	4.1	8	23	22	14	14	0.3	0	0	0.3	0.51	1
A0.5N100	13	2.7	3.8	10	13	15	9.9	11	0.4	0	0	0.4	0.55	1
A0.9N25	11	2.8	9.1	9.3	9.9	25	8.6	24	0.15	0	0	0.15	0.21	1
A0.9N50	10	2.4	5.1	8.7	9.1	20	8	17	0.22	0	0	0.22	0.34	1
A0.9N100	10	2.3	4.4	8.7	8.9	16	7.6	13	0.26	0	0	0.26	0.41	1
A0.9N200	11	2.3	4.2	9.7	8.6	11	7.7	11	0.33	0	0	0.33	0.59	1
<b>A0.99N100</b>	9.1	2.4	5.5	7.7	7.9	16	7.5	16	0.23	0	0	0.23	0.36	1

ometries. For the toroidal field models, this just shows the growth of the initially small magnetic flux threading the equator.

The value  $\Psi_H/\Psi_a$  (as other quantities, this is  $[\Psi_H(t)/[\Psi_a]_t]$  in the table) is [the magnetic flux on the horizon] per unit [flux available on the BH plus beyond the BH of the same polarity of magnetic flux]. This ratio shows how much more flux is available to the BH, and a value of  $\Psi_H/\Psi_a \sim 1$  would mean the magnetic flux beyond the BH is only of opposite polarity – so that the BH has as much flux as it can get of the same field polarity. The value  $\Psi_H/\Psi_s$  is similar to  $\Psi_H/\Psi_a$ , except it shows how much magnetic flux is available to the BH of any polarity within the stagnation radius. The stagnation radius ( $r_s$ ) is defined by where  $0 = \int \rho_0 u^r dA_{\theta\phi}$  over the full flow within  $b^2/\rho_0 < 1$  (so includes the disk inflow and entire wind outflows), because the whole flow has not reached inflow equilibrium there. This is roughly where  $u_r = 0$  as weighted for the whole massive flow. If the density-weighted radial lab-frame 3-velocity  $v_r = 0$  inside this radius, then that radius is used instead for  $r_s$ . Note that  $\Psi_a$  and  $\Psi_s$  have been time-averaged before forming a ratio in the table. Lastly, the value  $|\Phi_H/\Psi_H|$  shows the value

of the absolute magnetic flux per unit absolute of the extremum of the signed magnetic flux, where the ratio itself is time-averaged since the measurements are exactly co-spatial. As discussed in section 3.6, this roughly measures the vector spherical harmonic  $l$  mode (e.g.  $l = 1$  is dipolar).

For the polarity-flipping poloidal field models, the values of  $\Psi_H/\Psi_i \gtrsim 1$  if the magnetic flux on the BH has already exceeded the  $i$ -th loop's initial magnetic flux. So, in our polarity flip simulations, the table shows that magnetic flux has accumulated and been destroyed already twice in the simulation with the flipping model settling on the third extremum (i.e. 3rd field loop). Longer times lead to the next polarity being accreted. This shows that ordered flux is easily transported through the accretion disk, and large-scale field that penetrates the corona (see, e.g., Rothstein & Lovelace 2008) is not required for flux transport. Movies of the field lines (contours of  $A_\phi$  or streamlines of  $B^i$ ) do show that magnetic field lines at higher latitudes initially transport more readily than those at the equator as seen in more idealized models (Beckwith et al. 2009). However, eventually the magnetic flux threading the equator does accrete as

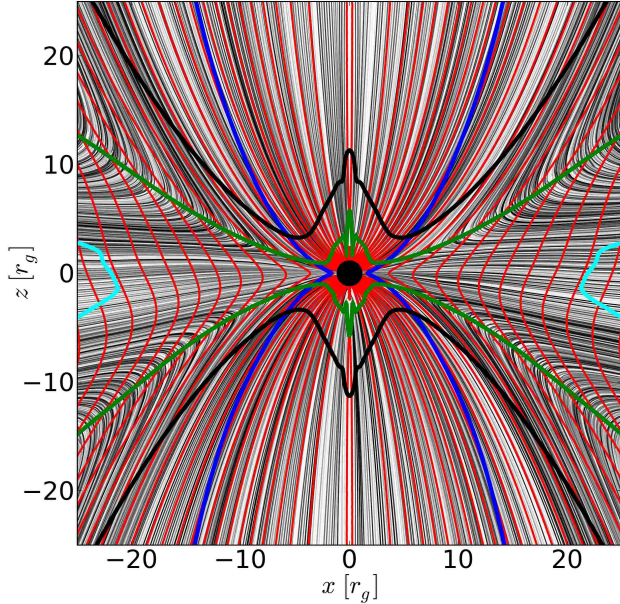


**Figure 19.** Flow-field (as in Figure 6 for our fiducial thick disk model) for model A0.99N100 with  $a/M = 0.99$  and a thinner disk. The thinner disks show less magnetic flux threading the BH. The dense inflow accretes onto the BH through the ordered magnetic flux via efficient non-axisymmetric magnetic Rayleigh-Taylor instabilities.

well, and in steady state we cannot identify anything special about the corona vs. the disk in accretion of ordered magnetic flux. Beckwith et al. (2009) suggest their simulations may have reached magnetic flux saturation near the BH (i.e. saturated  $\Upsilon_H$  and  $\Psi_H$ ), but they also found that most of the magnetic flux moves out to large radii rather than accreting. We suggest that this is due to their small initial torus leading to significant outflow of magnetic flux (as in their fig. 2, fig. 3, and animation).

The values of  $\Psi_H/\Psi_a$  and  $\Psi_H/\Psi_s$  show that there is plenty of magnetic flux available (including of the same polarity) for the BH in most models. These are time-averages, while in general each polarity loop that is accreted starts off at quite low values of  $\Psi_H/\Psi_a$  until nearing the next polarity when  $\Psi_H/\Psi_a \sim 1$  and then the field polarity inversion occurs on the horizon.

The MB09D model, typical of most torus-based MHD simulations in the literature, was time-averaged over an early period of accretion. However, already by  $t \sim 2000r_g/c$  the  $\Psi_H/\Psi_a \rightarrow 1$  and  $\Psi_H/\Psi_s \rightarrow 1$ , indicating there is no more available magnetic flux with the same polarity (either at all or within the part of the ingoing flow, respectively). Only the accretion of another  $\sim 5\times$  the same polarity magnetic flux would have led to a MCAF state and much higher  $\eta$ . Also, some prior MHD simulations may have been run for too short of a duration. Depending upon the initial conditions, the magnetic flux can accumulate over longer times than other quantities, so looking at only energy and angular momentum fluxes can be misleading. In short, the choice of initial conditions and short duration can limit  $\Upsilon_H$  and so the efficiencies.

The value of  $|\Phi_H/\Psi_H|$  shows the average approximate vector spherical harmonic  $|l|$ -mode. All poloidal field models have unity as expected, while the MB09Q large-scale quadrupolar field model has  $l \sim 3$  as expected given the large-scale field is quadrupolar ( $l = 2$ ) and there is an equatorial MHD turbulent disk.

Interestingly, the toroidal models show episodes with well-ordered and large-scale dipolar  $|l| \approx 1$  field on the horizon.

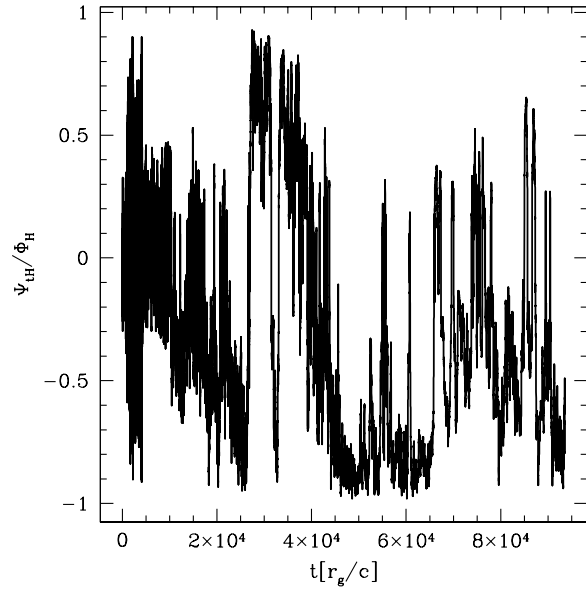


**Figure 20.** Value of  $\Psi_{IH}/\Phi_H$  corresponding to the approximate value of  $1/l$  for the vector spherical harmonic  $l$ -mode for model A0.94BtN10 (similar results for A0.94BtN10HR). This shows that well-ordered dipolar ( $|\Psi_{IH}/\Phi_H| \approx 1$ , where  $|\Psi_{IH}/\Phi_H| \approx 1/2$  corresponds to quadrupolar) field on the BH appears for somewhat sustained durations. In summary, only weak relativistic jets are produced in our simulations that start with mostly toroidal field, but much higher resolutions might allow this emergent large-scale dipolar field to launch persistent lightly-loaded relativistic jets.

For model A0.94BtN10 (A0.94BtN10HR is similar), Figure 20 shows  $\Psi_{IH}/\Phi_H$  (approximate  $1/l$  for the vector spherical harmonic  $l$  mode). The large-scale dipolar field is evident in Figure 21, where the large-scale dipolar flux extends out to  $r \sim 50r_g$ .

By contrast, Figure 22 shows the typical flow at times when  $|\Psi_{IH}/\Phi_H| \ll 1$ . The magnetic field is strongly mass-loaded and not particularly aligned with any rotational axis. The high-density material inflows from quite random directions.

During the episodes of large-scale dipolar flux formation in the toroidal field models, only weakly powered highly relativistic jets emerge due to too low  $\Upsilon \sim 3$ . Higher resolutions, higher  $\Upsilon$ , or somewhat thinner disks might promote more persistent jet formation, which is required by some reconnection-based jet models (Uzdensky & McKinney 2011; McKinney & Uzdensky 2012).

## 6.9 Power-Law Fits for Radial Dependence

The power-law scaling of quantities in the flow is important for testing accretion flow models. RIAFs such as ADAFs have  $\rho \propto r^{-3/2}$  and  $p_g \propto r^{-5/2}$ , while CDAFs have  $\rho \propto r^{-1/2}$ , and ADIOSs vary over this range. ADAFs have  $c_s/v_K \sim 0.5$ – $0.7$  and  $c_s/v_\phi \gtrsim 1$ .

Viscous simulations and RIAF models show similar radial scalings for density, velocity, and mass accretion rate (Stone et al. 1999; Igumenshchev et al. 2000; Igumenshchev & Narayan 2002; McKinney & Gammie 2002). For example, flows with  $\theta^d \sim 0.2$  show an inflow  $\dot{M} \propto r$  (Hawley & Balbus 2002). For viscous simulations, Igumenshchev & Abramowicz (2000) found  $\rho \propto r^{-1/2}$  to  $r^{-0.7}$  for  $\Gamma = 5/3$ – $4/3$ , respectively. For relatively thin disk injection 3D MHD simulations giving  $c_s/v_{\text{rot}} \sim 0.4$ , Igumenshchev et al. (2003) found  $\rho \propto r^{-1}$  and  $v_{\text{rot}} \propto r^{-1/2}$ . In 2D MHD simulations with  $c_s/v_{\text{rot}} \sim 0.6$ , Stone & Pringle (2001) (i.e. Run F) found  $\rho \propto$  con-

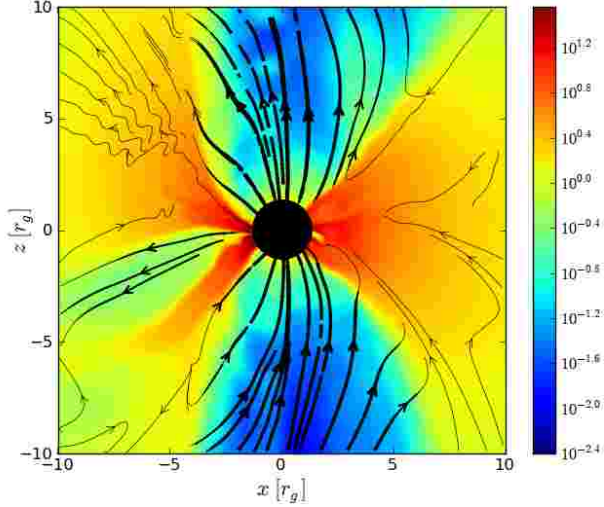


**Figure 21.** Like upper-left panel in Figure 4 and Figure 13, but for initially toroidally-dominated magnetic field model A0.94BtN10. This shows “spontaneous” formation of large-scale and dipolar magnetic flux near the BH at  $t \approx 62828 r_g/c$  – as also occurs at other times when  $|\Psi_{\text{th}}/\Psi_{\text{H}}| \sim 1$  (see Figure 20). The magnetic field lines are shown as thick (thin) black lines when they are lightly (heavily) mass-loaded. Only lightly mass-loaded field lines would permit ultrarelativistic jets. The magnetic field and low-density (blue in plot) wind/jet regions extend out to (not shown)  $r \sim 50 r_g$ .

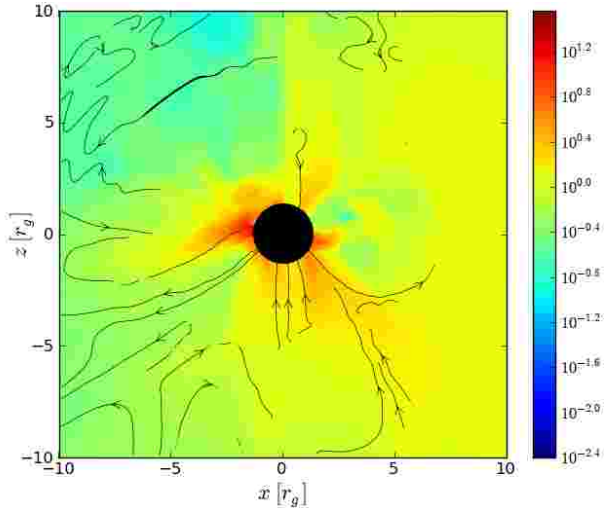


**Figure 22.** Like Figure 21, but typical snapshot at  $t \approx 40164 r_g/c$  when  $|\Psi_{\text{th}}/\Psi_{\text{H}}| \ll 1$  while the field is not dipolar or large-scale. Magnetic field lines are strongly mass-loaded (i.e. field lines shown as thin lines). Field lines appear/disappear because (in this slice) they bend in/out of the plotted plane. In such thick flows, mass inflow occurs from quite random directions with no strong preference for the plane of the disk/BH rotation.

stant,  $p_g \propto r^{-1.5}$  and  $v_r \propto r^{-1}$ . However, these MHD simulations involved relatively thin disks with  $\theta_\rho \lesssim 0.6$ . For MHD simulations of truly thick ( $\theta \sim 1$  or  $c_s/v_{\text{rot}} \gg 1$ ) flows, Pen et al. (2003) found  $\rho \propto r^{-0.72}$ ,  $p_g \propto r^{-1.5}$ , and  $v_{\text{rot}} \sim 0.1 v_K$  – a sub-Keplerian flow.

We now consider radial power-law fits (to the form  $f = f_0(r/r_0)^n$ ) for various quantities. Table 10 shows some of our results. The 5- $\sigma$  errors in the least squares fits for the power-law index are shown as a subscript, where systematic errors (not statistical errors) dominate the lack of a fit. We also by-eye looked at all fits and

confirmed that they are reasonable. This is how we tuned the time, number of inflow times, and number of  $\sigma$  that best represent something about the systematic uncertainties. A “-” is shown if the 5- $\sigma$  error permits  $n$  to pass through zero, except for  $|n| < 0.25$  in which case a “-” is shown if the 5- $\sigma$  error is larger than 0.25. MB09D and 2D models are not shown because of their small inflow equilibrium radii. The resulting power-law can change at larger radii because the flow is not strongly self-similar where fits are obtained.

Table 10 shows fits for “disk quantities”:  $\rho_0$ ,  $p_g$ , and  $|b|$  (where  $|b_\phi| \sim |b|$ ). We also consider (not shown)  $|v_r|$ ,  $|v_{\text{rot}}|$ ,  $|b_r|$ . These “disk quantities” have been averaged using the “dcden” averaging (i.e. density-weighted average). Power-law fits for cases “f”, “fdc”, “dc”, “ $\theta^d$ ”, “eq”, and “jet” are also considered but not shown (see section 3.4 for definitions of these other cases and more details).

These “disk quantities” are fit for radii  $r_i^{\text{dcden}}$  to  $r_o^{\text{dcden}}$ , where  $r_i^{\text{dcden}} = 12$  is typically set and  $r_o^{\text{dcden}}$  corresponds to  $N = 3$  inflow times for time  $T_i^a$  computed via Eq. (28) except limited to  $r_o^{\text{dcden}} \leq 30 r_g$  to get an accurate fit across all models. A single inflow for time  $T_i^a$  is given as  $r_f^{\text{dcden}}$ . The stagnation radius ( $r_s$ ), used in section 6.8, is used to restrict  $r_o^{\text{dcden}} < r_s$ . For some models (e.g. MB09D), if  $r_s < 12 r_g$  or  $r_o^{\text{dcden}} < 12 r_g$ , then we force  $r_i^{\text{dcden}} = 12$  and  $r_o^{\text{dcden}} = 16$ .

Table 10 also shows quantities  $\dot{M}_{\text{in}} - \dot{M}_{\text{H}}$ ,  $\dot{M}_{\text{mw}}$ , and  $\dot{M}_{\text{w}}$ . For these wind quantities, fits are from  $r = 20 r_g$  up to  $r_o^{\text{w}} = r_o^{\text{dcden}}$  defined before, but  $r_o^{\text{w}} > 40 r_g$  and  $r_o^{\text{w}} < 100 r_g$  are enforced.

For thick poloidal field models, roughly:  $\rho_0 \propto r^{-0.6}$ ,  $p_g \propto r^{-0.9}$ ,  $|v_r| \propto r^{-0.8}$ ,  $|v_{\text{rot}}| \propto r^{-0.5}$ ,  $|b_r|$ ,  $|b_\phi|$ ,  $|b| \propto r^{-1}$ , and  $\dot{M}_{\text{in}}$ ,  $\dot{M}_{\text{w}} \propto r^{1.3}$ . However, our A0.94BfN40 and A0.94BpN100 models have  $|v_{\text{rot}}| \propto r^{-1.0}$ . This occurs because our fiducial model (A0.94BfN40) was run for a longer time than any other models, while A0.94BpN100 has no polarity inversions so also has accumulated magnetic flux over a longer time. So these models are choked out to a larger radial range. The flows are sub-Keplerian, with  $v_{\text{rot}} \sim 0.2 v_K$  at  $r \sim 10 r_g$  for the fiducial model (similar to in Pen et al. 2003).

For thick toroidal field models, roughly:  $\rho_0 \propto r^{-0.6}$ ,  $p_g \propto r^{-0.8}$ ,  $|v_r| \propto r^{-0.7}$ ,  $|v_{\text{rot}}| \propto r^{-0.3}$ ,  $|b_r| \propto r^{-1}$ , and  $|b_\phi|$ ,  $|b| \propto r^{-1}$ ,  $\dot{M}_{\text{in}}$ ,  $\dot{M}_{\text{w}} \propto r^{1.3} - r^2$  with secular spin dependence. The flow is slightly sub-Keplerian in magnitude with  $v_{\text{rot}} \sim 0.5 v_K$  at  $r \sim 10 r_g$ .

For our thinner (TNM11) models with poloidal magnetic flux, roughly:  $\rho_0 \propto r^{-0.7}$  (depending upon initial  $\beta$ ),  $p_g \propto r^{-1.9}$ ,  $|v_r| \propto r^{-1}$  (but depends upon spin),  $|v_{\text{rot}}| \propto r^{-0.3}$ ,  $|b_r| \propto r^{-1.5}$ ,  $|b_\phi|$ ,  $|b| \propto r^{-1}$ , and  $\dot{M}_{\text{in}}$ ,  $\dot{M}_{\text{w}} \propto r^1 - r^2$  with secular spin dependence. These flows are mildly sub-Keplerian with  $v_{\text{rot}} \sim 0.6 v_K$  at  $r \sim 10 r_g$  for  $a/M = 0.99$ .

The MB09 models are close to Keplerian both in profile ( $v_{\text{rot}} \propto r^{-0.5}$ ) and value, as expected for weakly magnetized thinner disks.

Consider an example usage of these fits. Table 4 gives  $\dot{M}_{\text{j+mw}}(r = 50 r_g) \sim \dot{M}_{\text{j}} + \dot{M}_{\text{mw,o}}$ , and  $\dot{M}_{\text{w}}$  dominates. Table 10 gives the radial power-law index, so the total mass ejected to large radii is  $\dot{M}_{\text{j+mw}} \sim \dot{M}_{\text{j+mw}}(r = 50 r_g)(r/50 r_g)^n$  where  $n$  is from the second to last column in Table 10. For thick toroidal field models, the larger errors in  $\dot{M}_{\text{w}}(r)$  is because it flattens-out at larger radii. Perhaps steady-state has not been fully achieved by  $r \sim 100 r_g$ , or perhaps the self-similar region actually has a much shallower power-law index (consistent with  $\dot{M}_{\text{w}} \propto r^{0.5}$  in Pang et al. 2011).

In summary, our thicker disk MHD simulations lead to: flatter density profiles than the ADAF model, quite sub-Keplerian motion, and flat pressure profiles at large radii due to the hot material reservoir. Our thinner disk models have flatter density profiles than the ADAF model and somewhat sub-Keplerian motion. Our thick poloidal/toroidal power-law results are stable to the chosen time-averaging interval, while some TNM11 models evolve to slightly steeper density profiles.



**Table 10.** Inner and Outer Radii for Least-Square Fits, Disk+Corona Stagnation Radius, and Fitted Power-Law Indices for Disk and Wind Flows

ModelName	$r_i^{\text{dcen}}$	$r_o^{\text{dcen}}$	$r_f^{\text{dcen}}$	$r_s^{\text{dcen}}$	$\rho_0$	$p_g$	$ b $	$r_i^w$	$r_o^w$	$\dot{M}_{\text{in}} - \dot{M}_{\text{H}}$	$\dot{M}_{\text{mw}}$	$\dot{M}_w$
<b>A0.94BfN40</b>	12	29	55	310	$-0.61_{\pm 0.05}$	$-0.83_{\pm 0.07}$	$-1.1_{\pm 0.02}$	20	42	$1.3_{\pm 0.04}$	$0.5_{\pm 0.08}$	$1.3_{\pm 0.04}$
A0.94BfN100c1	12	27	280	280	$-0.63_{\pm 0.09}$	$-0.9_{\pm 0.1}$	$-0.85_{\pm 0.1}$	20	40	$1.3_{\pm 0.03}$	$0.6_{\pm 0.1}$	$1.3_{\pm 0.02}$
A0.94BfN100c2	12	27	44	340	$-0.62_{\pm 0.08}$	$-0.9_{\pm 0.1}$	$-0.8_{\pm 0.1}$	20	40	$1.4_{\pm 0.04}$	$0.8_{\pm 0.1}$	$1.5_{\pm 0.03}$
A0.94BfN100c3	12	27	590	280	$-0.6_{\pm 0.08}$	$-0.87_{\pm 0.1}$	$-0.8_{\pm 0.2}$	20	40	$1.4_{\pm 0.1}$	$0.6_{\pm 0.2}$	$1.4_{\pm 0.1}$
A0.94BfN100c4	12	29	280	310	$-0.63_{\pm 0.08}$	$-0.9_{\pm 0.1}$	$-0.8_{\pm 0.1}$	20	40	$1.5_{\pm 0.1}$	$0.4_{\pm 0.3}$	$1.6_{\pm 0.1}$
<b>A-0.94BfN40HR</b>	12	30	54	320	$-0.62_{\pm 0.06}$	$-0.85_{\pm 0.08}$	$-0.98_{\pm 0.06}$	20	46	$1.4_{\pm 0.04}$	$0.58_{\pm 0.05}$	$1.4_{\pm 0.04}$
A-0.94BfN30	12	30	310	310	$-0.68_{\pm 0.07}$	$-0.9_{\pm 0.1}$	$-1_{\pm 0.2}$	20	52	$1.5_{\pm 0.08}$	$0.58_{\pm 0.04}$	$1.5_{\pm 0.08}$
A-0.5BfN30	12	30	320	410	$-0.62_{\pm 0.08}$	$-0.9_{\pm 0.1}$	$-0.94_{\pm 0.09}$	20	58	$1.4_{\pm 0.2}$	$3_{\pm 2}$	$2.2_{\pm 0.1}$
A0.0BfN10	12	30	88	83	$-0.68_{\pm 0.07}$	$-0.93_{\pm 0.1}$	$-1.1_{\pm 0.1}$	20	75	$1.3_{\pm 0.1}$	-	$1.7_{\pm 0.02}$
A0.5BfN30	12	30	450	14000	$-0.55_{\pm 0.08}$	$-0.84_{\pm 0.09}$	$-0.8_{\pm 0.1}$	20	58	$0.8_{\pm 0.3}$	$4_{\pm 1}$	$1.4_{\pm 0.4}$
A0.94BfN30	12	27	310	14000	$-0.66_{\pm 0.09}$	$-0.9_{\pm 0.1}$	$-0.88_{\pm 0.05}$	20	40	$1.4_{\pm 0.06}$	$0.57_{\pm 0.03}$	$1.4_{\pm 0.05}$
A0.94BfN30r	12	27	430	14000	$-0.61_{\pm 0.08}$	$-0.8_{\pm 0.1}$	$-1_{\pm 0.02}$	20	40	$1.3_{\pm 0.09}$	$0.5_{\pm 0.2}$	$1.2_{\pm 0.09}$
A0.94BpN100	12	30	290	14000	$-0.65_{\pm 0.08}$	$-0.9_{\pm 0.1}$	$-0.8_{\pm 0.1}$	20	52	$1.3_{\pm 0.04}$	$0.56_{\pm 0.04}$	$1.2_{\pm 0.03}$
A-0.94BtN10	12	30	240	240	$-0.64_{\pm 0.07}$	$-0.88_{\pm 0.09}$	$-1.3_{\pm 0.1}$	20	100	$2.1_{\pm 0.2}$	-	$2.2_{\pm 0.3}$
A-0.5BtN10	12	30	160	160	$-0.64_{\pm 0.08}$	$-0.9_{\pm 0.1}$	$-1.2_{\pm 0.07}$	20	100	$1.3_{\pm 0.2}$	-	$1.4_{\pm 0.2}$
A0.0BtN10	12	30	190	190	$-0.61_{\pm 0.07}$	$-0.83_{\pm 0.09}$	$-1.1_{\pm 0.08}$	20	100	$1.4_{\pm 0.2}$	-	$1.5_{\pm 0.2}$
A0.5BtN10	12	30	200	200	$-0.67_{\pm 0.08}$	$-0.9_{\pm 0.1}$	$-1.2_{\pm 0.08}$	20	100	$1.7_{\pm 0.2}$	$-3_{\pm 2}$	$1.8_{\pm 0.2}$
A0.94BtN10	12	30	230	230	$-0.6_{\pm 0.08}$	$-0.8_{\pm 0.1}$	$-1_{\pm 0.08}$	20	100	$1.4_{\pm 0.2}$	$-1.6_{\pm 0.4}$	$1.4_{\pm 0.2}$
<b>A0.94BtN10HR</b>	12	30	180	170	$-0.72_{\pm 0.05}$	$-0.97_{\pm 0.07}$	$-1.1_{\pm 0.06}$	20	100	$2.2_{\pm 0.3}$	$-1.1_{\pm 0.1}$	$1.9_{\pm 0.2}$
MB09Q	12	15	23	20	$-0.9_{\pm 0.2}$	$-2.1_{\pm 0.1}$	$-0.64_{\pm 0.01}$	6	18	$0.7_{\pm 0.2}$	$1.6_{\pm 0.3}$	$1.3_{\pm 0.06}$
A-0.9N100	12	30	110	110	$-0.52_{\pm 0.05}$	$-1.5_{\pm 0.05}$	$-0.98_{\pm 0.03}$	20	73	$1.4_{\pm 0.1}$	$0.99_{\pm 0.03}$	$1.6_{\pm 0.09}$
A-0.5N100	12	30	100	100	$-0.6_{\pm 0.1}$	$-1.7_{\pm 0.09}$	$-0.96_{\pm 0.03}$	20	64	$1.9_{\pm 0.2}$	$1.1_{\pm 0.02}$	$2.2_{\pm 0.1}$
A-0.2N100	12	30	100	100	$-0.65_{\pm 0.02}$	$-1.7_{\pm 0.03}$	$-1_{\pm 0.05}$	20	65	$1.8_{\pm 0.2}$	$1.2_{\pm 0.04}$	$2.1_{\pm 0.08}$
A0.0N100	12	30	110	110	$-0.94_{\pm 0.05}$	$-2_{\pm 0.06}$	$-0.98_{\pm 0.05}$	20	69	$1.5_{\pm 0.2}$	$1.2_{\pm 0.09}$	$1.8_{\pm 0.1}$
A0.1N100	12	30	110	110	$-0.78_{\pm 0.04}$	$-1.9_{\pm 0.04}$	$-1_{\pm 0.04}$	20	65	$1.5_{\pm 0.2}$	$1.1_{\pm 0.07}$	$1.9_{\pm 0.2}$
A0.2N100	12	30	110	100	$-0.71_{\pm 0.05}$	$-1.8_{\pm 0.05}$	$-1_{\pm 0.03}$	20	66	$1.7_{\pm 0.2}$	$1.2_{\pm 0.06}$	$2_{\pm 0.1}$
A0.5N100	12	30	100	100	$-0.86_{\pm 0.02}$	$-1.9_{\pm 0.06}$	$-1.2_{\pm 0.03}$	20	61	$1.1_{\pm 0.07}$	$0.98_{\pm 0.03}$	$1.4_{\pm 0.04}$
A0.9N25	12	30	120	120	$-1.4_{\pm 0.1}$	$-2.3_{\pm 0.1}$	$-1.1_{\pm 0.02}$	20	90	$0.66_{\pm 0.02}$	$1_{\pm 0.06}$	$0.84_{\pm 0.02}$
A0.9N50	12	30	110	110	$-1_{\pm 0.1}$	$-2.1_{\pm 0.1}$	$-1.3_{\pm 0.02}$	20	81	$0.51_{\pm 0.08}$	$0.55_{\pm 0.04}$	$0.76_{\pm 0.07}$
A0.9N100	12	30	97	97	$-0.89_{\pm 0.09}$	$-2_{\pm 0.09}$	$-1.1_{\pm 0.02}$	20	60	$1.1_{\pm 0.1}$	$0.79_{\pm 0.02}$	$1.4_{\pm 0.1}$
A0.9N200	12	30	86	84	$-0.88_{\pm 0.04}$	$-1.9_{\pm 0.05}$	$-1.2_{\pm 0.009}$	20	66	$0.87_{\pm 0.07}$	$0.85_{\pm 0.008}$	$1_{\pm 0.05}$
<b>A0.99N100</b>	12	30	120	110	$-0.99_{\pm 0.07}$	$-2.1_{\pm 0.08}$	$-1.2_{\pm 0.01}$	20	77	$0.65_{\pm 0.04}$	$0.68_{\pm 0.04}$	$0.87_{\pm 0.05}$

## 6.10 Resolution

In this section, we determine whether our models are numerically converged. We consider both explicit convergence testing and so-called “convergence quality factors” that (e.g.) measure how many grid cells resolve various critical length scales (Sano et al. 2004; Hawley et al. 2011; Shiokawa et al. 2012; Sorathia et al. 2011). Note that MRI quality factors like  $Q_{\theta, \text{MRI}}$ ,  $Q_{\phi, \text{MRI}}$  are not too useful for the new poloidal field models for which the MRI is suppressed.

First, consider our overall resolution, box size, and numerical method choices. We knew that  $|m| = 1$  modes would dominate and even be required for (non-axisymmetric) accretion once the magnetic barrier formed in poloidal field models. So, we chose to treat the poloidal and toroidal dimensions equally by ensuring the grid has a uniform grid cell aspect ratio, which also allows us to use less poloidal resolution to accurately capture the MRI (Hawley et al. 2011). Also, because  $m = 1$  modes generally dominate,  $\Delta\phi = 2\pi$  is required, as also found by Shiokawa et al. (2012) and Henisey et al. (2009). In addition, other HARM-based GRMHD codes use the diffusive Tóth scheme, while our code uses a staggered field scheme that treats field quantities more accurately.

One indicator that an MHD simulation is unresolved is that

MHD turbulence decays, magnetic field strengths drop, and fluxes secularly tend towards Novikov-Thorne values. These were used by Shiokawa et al. (2012) and Noble et al. (2010) as evidence that certain resolutions were insufficient to resolve the MRI. Except for the MB09D model, we see no evidence for such behavior.

Just because turbulence does not decay does not mean the saturated state is converged. Convergence can only be ensured by performing explicit convergence testing and by resolving critical length scales.  $\alpha_{\text{mag}} \gtrsim 0.4$ ,  $Q_{\text{nlm}, \text{cor}} \gtrsim 6$ ,  $Q_{\theta, \text{MRI}} \gtrsim 10$ , and  $Q_{\phi, \text{MRI}} \gtrsim 20$  may be required to achieve tens of percent level convergence for the MRI (Hawley et al. 2011; Shiokawa et al. 2012). These quantities are given in Table 8 as described in section 6.7.

Consider how changing  $N_\phi$  changes the results for models A0.94BfN?c? and A0.94BfN30(r). Although initial  $\beta$  varies in those models, we already discussed how the magnetic flux near the BH has saturated independently from the initial magnetic flux. All tabulated results for these 3D models are similar to within  $\sim 30\%$  fractional differences. Also, different realizations (A0.94BfN30(r)) and different  $\beta$  (A0.94BfN100c1) are within  $\sim 10\%$  fractional differences in  $\eta_{\text{H}}$ . Statistically, our averages are only accurate to  $\sim 20\%$  fractional differences, so values within this range are con-

sidered similar. However, we already saw from section 5.6 and section 5.7 that there is significant power at higher  $|m|$ . While these higher  $|m|$  modes only moderately affect the  $\theta - \phi$  integrated quantities on the horizon or other radii, they significantly affect the time dependence of the solution. A plot (not shown) of (e.g.) efficiency vs. time shows more violent oscillations at lower  $N_\phi$ . This suggests that the temporal behavior is qualitatively affected by how well-resolved the  $|m|$  modes are, and only the  $N_\phi = 128$  model shows temporal variability similar to the fiducial model.

Consider how changing  $N_r, N_\theta, N_\phi$  by a factor of two changes the results for models A0.94BfN40 (fiducial model) vs. A0.94BfN100c1 and A0.94BfN30(r). Changes in measured quantities are order tens of percent as discussed before. In addition, consider the azimuthal correlation length's  $m$  mode ( $m_{\text{cor}}$ , via Eq. (31)) for quantities  $\rho_0, u_g, b^2, \underline{u}', b_i, B_i, F_M, F_E^{\text{EM}}, F_E^{\text{MA}}$  (and their absolute value versions) both in the “Disk” and “Jet”. For A0.94BfN40, across all quantities,  $m_{\text{cor}} \sim 6$ –14, except in the “Disk” we found  $m_{\text{cor}} \sim 20$  for  $b_r$  and  $m_{\text{cor}} \sim 15$  for  $b^2$  at  $r/r_g = 4, 8, 30$ . On the horizon itself, where the disk is quite geometrically thin and the flow is causally disconnected from the rest of the solution, magnetic field components in the disk+corona have  $m_{\text{cor}} \leq 45$ . Even for field components,  $Q_{m,\text{cor}} \geq 14$  (via Eq. (44), grid cells per correlation length) outside the horizon and  $Q_{m,\text{cor}} \geq 6$  on the horizon. Beyond the horizon, the jet is always even better resolved than the disk. So, our lower-resolution choice of  $N_\phi = 128$  is sufficient to resolve most structures beyond the horizon.

Consider the vertical and radial correlation lengths in the “Disk”. At  $r = r_H, 4r_g, 8r_g, 30r_g$ , respectively, we find  $l_{\rho_0,\text{cor}} \approx 95, 58, 58, 57$  giving  $Q_{l,\text{cor},\rho_0} \approx 3, 6, 6, 5$  grid cells per vertical correlation length. Also,  $l_{b^2,\text{cor}} \approx 108, 37, 27, 17$  giving  $Q_{l,\text{cor},b^2} \approx 3, 8, 12, 18$ . Also, the grid cells per radial correlation lengths are  $Q_{n,\text{cor},\rho_0} \approx 7, 18, 22, 22$  and  $Q_{n,\text{cor},b^2} \approx 7, 16, 21, 22$ . Note that taking the spectrum of the averaged flow rather than the averaged spectrum leads to about twice higher *apparent* mode resolution for the vertical and radial correlation lengths. With  $\theta^d \approx 0.06, 0.13, 0.29, 0.59$ , this gives  $\lambda_{\theta,\text{cor},\rho_0}/\theta^d \approx 0.6, 0.4, 0.2, 0.1$  and  $\lambda_{\theta,\text{cor},b^2}/\theta^d \approx 0.5, 0.7, 0.4, 0.3$ . Beyond the horizon, the jet is always even better resolved than the disk. Summarizing, this shows that the narrow density filaments are fairly resolved despite the strong magnetic Rayleigh-Taylor instabilities, while the magnetic field that fills-in the region between the dense filaments is well-resolved beyond the horizon. Across our poloidal field models,  $N_\theta = 128$  is optimal to resolve the compressed dense magnetic Rayleigh-Taylor filaments outside the horizon, while the magnetic field is marginally resolved even at  $N_\theta = 64$  (used for sweeping over spin).

Consider the A0.94BtN10(HR, i.e. high-resolution) toroidal field models. The HR model gives  $\alpha_b$  and all  $\eta$ 's as quite similar. So, our lower-resolution toroidal field models are probably quantitatively converged. Indeed, all our toroidal models have  $Q_{\theta,\text{MRI}} \geq 10$ ,  $Q_{\phi,\text{MRI}} \geq 10$ ,  $Q_{\phi,\text{weak,MRI}} \geq 20$ , and  $\alpha_{\text{mag}} \approx 0.4$  as required to well-resolve the MRI (Hawley et al. 2011). The A0.94BtN10 model has  $Q_{\theta,\text{MRI}} \geq 10$ ,  $Q_{\phi,\text{weak,MRI}} \geq 10$ ,  $Q_{\phi,\text{MRI}} \geq 58$ ,  $Q_{\phi,\text{weak,MRI}} \geq 32$ , and  $\alpha_{\text{mag}} \approx 0.34$ . The A0.94BtN10HR model has  $Q_{\theta,\text{MRI}} \geq 50$ ,  $Q_{\phi,\text{weak,MRI}} \geq 30$ ,  $Q_{\phi,\text{MRI}} \geq 170$ ,  $Q_{\phi,\text{weak,MRI}} \geq 80$ , and  $\alpha_{\text{mag}} \approx 0.38$ . (The stated  $Q$ 's are limited by flow at  $r = r_o$  where 3 inflow times have passed.) So the MRI is probably well-converged. In addition, for A0.94BtN10HR, across all quantities (see list in previous paragraph) and locations (disk+corona and jet), the azimuthal correlation's  $m_{\text{cor}} \approx 6$ –22 (typically  $\sim 10$ ) at all radii  $r = r_H, 4r_g, 8r_g, 30r_g$  corresponding to  $Q_{m,\text{cor}} > 12$  (typically  $\sim 20$ ) grid cells per correlation length. Also, this corresponds to a typical azimuthal correlation length  $d\phi_{\text{cor}} \sim 0.9\theta^d$ , so that the

largest correlated azimuthal structures are about as extended as the half-vertical disk extent. These facts suggest that  $N_\phi = 128$  (all our toroidal field models have  $N_\phi \geq 128$ ) is sufficient to well-resolve azimuthal structures. The vertical correlation lengths are resolved with  $Q_{l,\text{cor}} \sim 18$ –30 (typically  $\sim 25$ ) cells across all quantities and all radii, while the radial correlation length is resolved with  $Q_{n,\text{cor}} \approx 7, 20, 25, 25$  grid cells at  $r = r_H, 4r_g, 8r_g, 30r_g$ , respectively, for both  $\rho_0$  and  $b^2$ . In summary, our A0.94BtN10HR model is among the highest-resolved global MHD simulations.

The 2D axisymmetric simulations are inappropriate for studying MCAFs (see also Igumenshchev 2009). Once magnetic flux has accumulated up to a saturation point even beyond the BH, accretion cannot occur in axisymmetry except through reconnection. Once so much magnetic flux has accumulated just beyond the BH, the entire flow rebounds backwards leading to low  $\eta_H$ . Eventually, mass builds up and forces magnetic flux back onto the BH leading to high  $\eta_H$ . Also, of course, 2D axisymmetric simulations cannot resolve the non-axisymmetric MRI or sustain a magnetic dynamo.

We now compare our resolutions with prior simulations of magnetic flux accumulation. Stehle & Spruit (2001) used a resolution up to  $N_r \times N_\phi = 156 \times 128$  per decade in radius. So their simulations are roughly equally resolved to our fiducial models that have about half of the resolution per decade. They used van Leer interpolation, which has less than half the accuracy of our PPM-type interpolation. The 3D pseudo-Newtonian (PN) MHD simulations by Igumenshchev et al. (2003) used a Cartesian grid with  $\Delta\phi = \pi/2$ . Their inner-most cell size is  $0.5r_g$  at  $R_{\text{in}} = 4r_g$ . (a quite large  $R_{\text{in}}$ , see McKinney & Gammie 2002.) Our fiducial model has  $dr \sim 0.1r_g$ ,  $dz \sim 0.037r_g$ , and  $r \sin\theta d\phi \sim 0.097r_g$  at  $r = 4r_g$  and has  $dr \sim 0.035r_g$ ,  $dz \sim 0.0076r_g$ , and  $r \sin\theta d\phi \sim 0.033r_g$  at  $r = r_H$ , so our  $z$ -resolution is about  $10\times$  higher. The 3D PNMHD energy-conserving PPM-type simulations by Igumenshchev (2008); Punsky et al. (2009) are full  $\Delta\phi = 2\pi$  with  $N_r \times N_\theta \times N_\phi = 182 \times 84 \times 240$  for a comparable resolution per radii as our fiducial model, except very close to the BH where we have about  $4\times$  the  $\theta$ -resolution.

## 7 DISCUSSION

Our simulations show that the accumulation of poloidal magnetic flux leads to a two-phase-like magnetospheric accretion flow that is dramatically different than the standard MRI-driven MHD turbulent accretion flow. The flow that develops in our simulations is conceptually similar to the “magnetically arrested disk” (MAD) flow (Narayan et al. 2003). While the standard weakly magnetized MRI-driven MHD turbulent flow has gas and magnetic pressures in force balance near the hole, the MAD state develops as magnetic flux accumulates and magnetic forces balance the inflow's ram or gravitational forces. The originally-conceived MAD flow has a sharp magnetospheric boundary layer with a large density contrast at some radius, as confirmed by low-resolution 3D MHD simulations (e.g., fig. 13 in Igumenshchev et al. 2003; also seen in our 2D axisymmetric simulations). In these pioneering studies, accretion occurs primarily via diffusive reconnection events.

Our high-resolution fully 3D simulations show that efficient non-axisymmetric magnetic Rayleigh-Taylor (RT) instabilities prevent the formation of the MAD's sharp magnetospheric barrier. Any additional magnetic flux that tries to accrete onto the BH is redistributed out in the disk by these instabilities. Also, we found that the magnetosphere geometrically compresses the dense inflow. We call this fully non-linear MAD flow a “magnetically choked accretion flow” (MCAF), referring to the magnetic flux compressing

the dense inflow leading to enhancement of the magnetization over much of the horizon. Such a magnetic choke is analogous to chokes in man-made engines, within which it enriches the fuel mixture by partially shutting off the air intake.

Our simulations confirm the brief 3D pseudo-Newtonian MHD simulations by Igumenshchev (2008) that also show MCAF formation. We also roughly confirm the magnetospheric QPO mechanism by Li & Narayan (2004), which in their model drives some disk-based frequency at a vertical magnetic barrier. However, our 3D simulations show that the disk inflow interacts with the polar magnetic flux threading the rotating BH, which leads to a new “jet-disk” QPO (JD-QPO) mechanism based upon the BH rotation frequency. We also reaffirm that the BZ mechanism operates efficiently, except our low-spin thick-disk models do not form relativistic jets due to mass infall. Otherwise, the BZ mechanism leads to powerful jets directly from the BH for our poloidal field models. We confirm the 3D GRMHD simulations by Tchekhovskoy et al. (2011), who showed that outflow efficiencies of  $\eta \gtrsim 100\%$  are possible once the BH with  $|a/M| \gtrsim 0.9$  has reached poloidal magnetic flux saturation. As in other MHD simulations, the entire wind’s outflow rate is roughly  $\dot{M}_w \propto r$ .

We also confirm the results of Igumenshchev (2008) that  $a/M = 0$  MCAF models have low heat+outflow efficiencies of  $\eta \sim$  few percent. One would expect heat+outflow efficiencies of  $\eta \sim 100\%$  even for  $a/M = 0$  if even the dense inflow were significantly arrested (Narayan et al. 2003). In particular, for  $a/M = 0$ , our thinner disk models have  $\eta_H \sim 5\%$ , while the NT efficiency is  $\eta_{NT} \sim 6\%$ . For the thick disk models,  $\eta_H < 0\%$  and  $\eta_H^{EM} \sim 0\%$ . In the simulations, the heavy disk inflow is relatively unmagnetized and not sufficiently slowed to achieve high  $\eta$ .

Radiatively efficient MCAF states (not studied in this paper) might still be hyper-NT efficient even for  $a/M = 0$  (Narayan et al. 2003). Our thinner disk models have a high specific enthalpy such that  $\eta_H^{PAKE} \sim 34\%$  and  $\eta_H^{EN} \sim -28\%$  for  $a/M = 0$  and  $\eta_H^{PAKE} \sim 64\%$  and  $\eta_H^{EN} \sim -62\%$  for  $a/M = 0.99$ . Emission of that free thermal energy would give a radiative efficiency of up to  $\eta_{rad} \sim 28\%$  for  $a/M = 0$  and  $\eta_{rad} \sim 62\%$  for  $a/M = 0.99$ . However, the trend with thickness is roughly  $\eta^{EN} \propto \theta'$  across our models, so we would predict that thin disks with  $\theta' \lesssim 0.03$  (as relevant for BH x-ray binaries in the thermal state; Kulkarni et al. 2011) would have no enhanced radiative efficiency. Thin radiatively efficient MCAFs should be studied with GRMHD simulations to check.

We confirm the suggestion by Igumenshchev et al. (2003) that most prior MHD disk simulations used initial conditions that limited the available magnetic flux. For example, a relatively radially-narrow torus can only have a relatively small amount of magnetic flux inserted if also keeping  $\beta \gg 1$  to allow for the MRI. Also, much of the matter and field can be ejected or remain beyond the torus pressure maximum rather than being accreted. After  $\Psi_H$  reaches a quasi-steady-state, one can test whether an MHD simulation is limited by such initial conditions. One computes  $\Psi_H/\Psi_a$  (i.e. [flux on hole] per unit [flux on the hole plus just outside the hole of the same polarity]) and also  $\Psi_H/\Psi_s$  ([flux on hole] per unit [flux on the hole plus available within the stagnation radius for radial inflow]). One must compute both because there may be plenty of same-polarity magnetic flux beyond the hole, but it may not be accreting. One could also compute how much flux is available within the inflow equilibrium region. Both  $\Psi_H/\Psi_a \sim 1$  and  $\Psi_H/\Psi_s \sim 1$  for MB09D, so the initial conditions artificially limited the magnetic flux that can reach the hole. Also, it appears that  $\Psi_H/\Psi_s \sim 1$  in the simulations by Beckwith et al. (2009), who show much magnetic flux is ejected to (or remains at) large radii.

A local  $\alpha$ -viscosity leads to a poor model of angular momentum transport for the simulations. The effective  $\alpha$  is different than predicted by local stresses divided by either total or magnetic pressure for all our thick ( $H/R \sim 1$ ) disk and poloidal field thinner ( $H/R \sim 0.3$ ) disk models. The  $\alpha$ -disk theory only works well for our weak poloidal field models of either very thin ( $H/R \sim 0.05$ ) or relatively thin ( $H/R \sim 0.3$ ) disks. Large-scale magnetic confinement forces, rather than local stresses, may be acting on the dense inflow. Also, for our toroidal thick disk models, convection may be important because Reynolds stress dominates Maxwell stress.

Interestingly,  $S_{d,MRI} \sim 1$  (or  $S_{d,MRI} \sim 0.25$ – $0.5$ ) gives the disk’s saturated vertical field strength in our toroidal (or poloidal) field models. Also, the effective viscosity is  $\alpha_{eff} \sim 0.1$ – $1$  ( $\alpha_{eff2}$  is at most  $2\times$  smaller for the new thinner models and at most  $4\times$  smaller for the new thick disk models), which is sufficiently consistent with observations (King et al. 2007).

MCAFs might explain observations of apparently highly efficient jets (Laing et al. 1983; Willott et al. 1999; Birzan et al. 2004; Ogle et al. 2006; Richards et al. 2006; Ghisellini et al. 2010; McNamara et al. 2011; Fernandes et al. 2011; Punsly 2011). However, more work is required to ensure the observations are accurately modelled. For example, the jet models in Fernandes et al. (2011) have factors (e.g.  $f$ , see Willott et al. 1999) that can significantly change depending upon estimates of the invisible work done by the jet. Also, there are similar uncertainties in translating to the jet power in McNamara et al. (2011) as related to work done by bubble expansion (Birzan et al. 2004). Also, the Blazar estimates of jet power by Ghisellini et al. (2010) can be affected by models of the Doppler factor. 178Mhz observations by Ogle et al. (2006) are affected by a lack of simultaneity between optical and radio emission, and the systems they observe could be low-luminosity radiatively inefficient systems that lowers their jet efficiency requirements. Our simulations may help constrain such jet power estimates.

MCAFs may also help explain the variety of spectral states seen in BH x-ray binaries (Rutledge et al. 1999; de Gouveia dal Pino & Lazarian 2005; Igumenshchev 2008, 2009). The accumulation of magnetic flux might lead to the low-hard, bright-hard, and hard:steep-power-law intermediate states with LFQPOs whose frequency is controlled by the “magnetospheric radius” ( $r_m$ ) and with a persistent (mostly invisible) radio jet. The steep power law (very high) state could be due to reconnection as a field polarity reversal makes its way to the hole, where the reconnection with the jet on slightly larger scales makes the HFQPOs visible near the BH. Dissipation of the accumulated magnetic flux on the hole could cause the jet to light-up as a radio bright outgoing reconnecting plasmoid. The remaining disk without accumulated flux can lead back to the thermal (high-soft) state that has no jet and no (or very weak) QPOs. Notice that we distinguish between QPOs and jets being present vs. visible. Future work can test these speculations.

## 8 CONCLUSIONS

Black hole systems may have plenty of coherent magnetic flux available at large radii that can feed the accretion flow down to the black hole. Using fully 3D GRMHD simulations of extended radiatively inefficient accretion flows, we found that poloidal magnetic flux readily accretes from large radii and builds-up to a natural saturation point near the black hole independently from the initial poloidal magnetic flux. The accumulated poloidal magnetic flux naturally leads to a highly non-axisymmetric “magnetically choked accretion flow” (MCAF), within which the MRI is suppressed.



In such a choked state, the polar magnetic flux forces accretion to occur through magnetic Rayleigh-Taylor instabilities and geometric compression. Near the black hole, the inflow is highly compressed, which leads to a highly magnetized state over most of the horizon. So the accumulated flux acts as an inflow choke (analogous to air chokes in engineering that lead to fuel enrichment), which allows for greater than 100% jet efficiencies for  $|a/M| \gtrsim 0.9$ .

Once the horizon's magnetic flux reaches a saturated state, the inflow pushes its way through the jet's bulging magnetosphere. This leads to a new jet-disk high-frequency quasi-periodic oscillation (JD-HFQPO) mechanism driving spherical harmonic  $|m|$  mode oscillations with a frequency set by the black hole's field line angular rotation frequency at the jet-disk interface. So these HFQPOs may allow one to measure black hole spin. The coherence quality factor is highest in the jet and at the jet-disk interface (harboring large magnetic energy) rather than in the disk plane, so these HFQPOs could be dominated by non-thermal emission. More work is required to test their observability.

In contrast to our initially poloidally-dominated magnetic field models that develop the uncommonly-found MCAF state, our initially toroidally-dominated magnetic field simulation results are similar to as seen in prior works. A significant new result is that such models do show large-scale dipolar magnetic flux formation near the horizon. However, only weak transient highly magnetized relativistic jets emerge. Higher resolutions or spins could promote this emergent dipolar field to launch persistent relativistic jets.

As with any numerical study, more convergence testing is required. Our toroidal field models satisfy the convergence quality factors of  $Q_{\theta, \text{MRI}} \gtrsim 10$ ,  $Q_{\phi, \text{MRI}} \gtrsim 20$ , and  $\alpha_{\text{mag}} \approx 0.4$  in Hawley et al. (2011) and  $r, \theta, \phi$  correlation lengths are well-resolved. Our fiducial poloidal model well-resolves all correlation lengths. We explicitly tested convergence with  $r, \theta, \phi$ -resolutions for  $a/M = 0.9375$  poloidal/toroidal models, and most values are converged to 30% and some values (e.g.  $\Upsilon$  for poloidal models) are converged to 10%. We found that the convergence criteria of Hawley et al. (2011) are not generally sufficient (e.g. jet efficiency continues to change significantly in toroidal models) or applicable (e.g. MRI can be suppressed). Our code conserves energy during large-scale field reconnection (as in Lyutikov & McKinney 2011), occurring in magnetic Rayleigh-Taylor disruptions and field polarity inversions, but the reconnection rate may be set by grid diffusivity.

In summary, the MCAF state and the spontaneous large-scale dipolar field generation seen in toroidal field models should be accounted for when seeking to understand SgrA\*, M87, Blazars, high-powered quasars, black hole x-ray binaries, and other systems. In future work, we will consider the spin dependence of the jet/wind power (Tchekhovskoy & McKinney 2012) and of the JD-QPO, characterize the “magnetospheric radius” and determine its spin dependence, perform radiative transfer to identify the observational signatures of MCAFs, and study the source of angular momentum transport (e.g. turbulence vs. large-scale stresses).

## ACKNOWLEDGMENTS

We thank Ramesh Narayan, Serguei Komissarov, Robert Penna, Eliot Quataert, Ioannis Contopoulos, Julian Krolik, Charles Gammie, Jonathan Arons, Vasily Beskin, and Kris Beckwith for useful discussions. This work was supported by a NASA Chandra Fellowship PF7-80048 (JCM), Princeton Center for Theoretical Science Fellowship (AT), and NSF/XSEDE resources provided by

TACC (Lonestar/Ranch) and NICS (Kraken) under awards TG-AST080025N (JCM) and TG-AST100040 (AT).

## SUPPORTING INFORMATION

Additional Supporting Information may be found in the online version of this article: Movie file. Movie of the fiducial model A0.94BfN40 showing the animated version of Fig. 4 (see caption alongside movie file for more detail).

## APPENDIX A: NUMERICAL METHODS

Our simulations use the GRMHD code HARM based upon a conservative shock-capturing Godunov scheme with 2nd order Runge-Kutta time-stepping, Courant factor 0.8, LAXF fluxes, simplified wave speeds, PPM-type interpolation (with no contact steepener, but with shock flattener based upon rest-mass flux density and total pressure) for primitive quantities ( $(\rho_0, u_g, \tilde{u}^i, \underline{B}^i)$ ), a staggered magnetic field representation, and any regular grid warping (Gammie et al. 2003; Noble et al. 2006; Tchekhovskoy et al. 2007).

One key feature of our HARM is its handling of grid cells with large magnetic energy per unit rest-mass energy. The code first tries to convert conserved to primitive quantities using the ideal MHD equations (Mignone & McKinney 2007). If that fails, the entropy conservation equations are tried. If that fails, the cold ideal MHD equations (with the failed grid cell having its internal energy averaged over its immediate neighbors) are tried. If that fails, the primitives are averaged over non-failed neighbors. The inversions are sought to machine accuracy. Density floors are used to avoid too low densities that lead to inversion failures.  $u_g$  is chosen as to enforce  $u_g/\rho_0 \leq 50$ , then  $\rho_0$  is chosen as to enforce  $b^2/\rho_0 \leq 50$  and  $b^2/u_g \leq 10^3$ , and then these implied comoving changes are added to the stress-energy tensor in the ZAMO frame. Using a fixed (rather than comoving) frame avoids run-away energy-momentum gains.

These inversion reductions and density floors mostly occur in the cold highly-magnetized jet with ordered magnetic field along which the flow moves. So, we set  $\rho_0 = u_g = 0$  in calculations (except in color images) if, e.g. for the “thick disk” simulations,  $b^2/\rho_0 \geq 30$  to  $b^2/\rho_0 \geq 10$  from  $r_H$  to  $r = 9r_g$ , respectively, as interpolated linearly with radius (tracing injected mass-energy, as in Tchekhovskoy et al. 2011, gives a bit more accuracy). Floors affect  $\tilde{u}^\phi, \Omega_F$  only near the axes (not in the disk or collimated jets).

Another key feature of our HARM is how the 3D polar axis is treated (McKinney & Blandford 2009). To resolve the staggered field component  $\underline{B}^{(2)}$ , a machine error polar cut-out of size  $d\theta = 10^{-13}$  is used. The values of  $\underline{B}^{(2)}$  on the polar cut-out are copied asymmetrically across the pole. All other primitives are interpolated from active cells to ghost cells at the same physical locations and also to the polar cut-out. All fluxes are set to vanish at the pole, except for the induction update to  $\sqrt{-g}\underline{B}^{(2)}$ . The small  $\theta$  factors in  $\sqrt{-g}$  cancel on both sides of the induction equation allowing one to recover  $\underline{B}^{(2)}$  on the polar cut-out. This procedure introduces a complex phase to the otherwise singular polar axis, where for general discontinuous flows the only constraint is from  $\nabla \cdot \underline{B} = 0$  that forces  $\underline{B}^{(2)}$  to be continuous along  $\theta$  across the pole for each  $\phi$ . This transmissive polar boundary condition allows the flow to pass through the polar region with only additional dissipation due to the polar triangular mesh as compared to a more uniform mesh.

Another key feature is the connection coefficients are corrected to obtain zero body forces to machine error for constant

pressure. Nominally, constant pressure flux and source terms do not cancel, and this secular differencing error sits at the polar axes. For constant pressures, the relevant equation of motion is

$$\partial_t(\sqrt{-g}\delta_\nu^i) = -\partial_j(\sqrt{-g}\delta_\nu^j) + \sqrt{-g}\delta_\lambda^k\Gamma_{\nu k}^\lambda. \quad (\text{A1})$$

Assuming  $\partial_t(\sqrt{-g}) \sim 0$  and  $\partial_j(p_{\text{tot}}) \sim 0$ , then  $0 = -\partial_\nu(\sqrt{-g}) + \sqrt{-g}\Gamma_{\nu k}^\lambda$  or  $\Gamma_{\nu k}^\lambda = \partial_\nu(\sqrt{-g})/\sqrt{-g}$ . We need to subtract off face-related flux-positioned values and add center-related conservative-positioned values. Let a grid cell indexed by  $i, j, k$  have grid face position  $x_-^k \equiv x_f^k(i, j, k)$  and upper grid face position of  $x_+^k \equiv x_f^k(i + dx^k\delta_\kappa^1, j + dx^k\delta_\kappa^2, k + dx^k\delta_\kappa^3)$  ( $\kappa$  chosen, not summed) such that the cell size is  $\Delta x^k = x_+^k - x_-^k$  and cell center position is  $x_c^k = (x_+^k + x_-^k)/2$ . First, compute  $C_k = \Gamma_{\mu k}^\mu$  as using a *continuous* approximation to the derivatives at  $x_c$ . These are computed using a modified `dfridr()` in Press et al. (1986) to achieve a uniformly low error. The conversion from internal to physical coordinates is generated from a simplified continuous approximation to the derivative with a difference size of  $10^{-5}dx^k$ , which depends upon range in  $x^k$  as necessary to ensure the differencing scales with the grid. Second, compute  $D_k = \Gamma_{\mu k}^\mu$  using *discrete* differences across the actual grid cell via  $D_k = (\sqrt{-g}[x_+^k] - \sqrt{-g}[x_-^k])/(\Delta x^k \sqrt{-g}[x_c])$ . Now, changing each  $\kappa$  term independently can lead to too large changes in some limits. Instead, we construct the weights  $S_\kappa = 10^{-300} + |\Gamma_{\kappa\mu}^\mu|$  (sum over  $\mu$ ) and let  $dS_\kappa = D_k - C_k$ ,  $W_{\kappa\mu} = |\Gamma_{\kappa\mu}^\mu|/S_\kappa$  (no sum over  $\kappa$  or  $\mu$ ). Finally, for each  $\mu$  and each  $\kappa$ , the correction is

$$\Delta\Gamma_{\kappa\mu}^\mu = dS_\kappa W_{\kappa\mu} \quad (\text{A2})$$

(no sum over  $\kappa$  or  $\mu$ ). The new connection gives machine error cancellation between source and flux differencing of pressure.

## REFERENCES

- Abramowicz M. A., 2005, *Astronomische Nachrichten*, 326, 782  
 Abramowicz M. A., Chen X., Granath M., Lasota J., 1996, *ApJ*, 471, 762  
 Abramowicz M. A., Chen X., Kato S., Lasota J., Regev O., 1995, *ApJ*, 438, L37  
 Agol E., Krolik J. H., 2000, *ApJ*, 528, 161  
 Aly J. J., Kuijpers J., 1990, *A&A*, 227, 473  
 Arons J., Lea S. M., 1976, *ApJ*, 207, 914  
 Arons J., Lea S. M., 1980, *ApJ*, 235, 1016  
 Babcock H. D., 1959, *ApJ*, 130, 364  
 Balbus S. A., Hawley J. F., 1991, *ApJ*, 376, 214  
 Balbus S. A., Hawley J. F., 1998, *Rev. Mod. Phys.*, 70, 1  
 Barkov M. V., Komissarov S. S., 2008, *MNRAS*, 385, L28  
 Beckwith K., Armitage P. J., Simon J. B., 2011, *MNRAS*, 416, 361  
 Beckwith K., Hawley J. F., Krolik J. H., 2008a, *ApJ*, 678, 1180  
 Beckwith K., Hawley J. F., Krolik J. H., 2008b, *MNRAS*, 390, 21  
 Beckwith K., Hawley J. F., Krolik J. H., 2009, *ApJ*, 707, 428  
 Begelman M. C., 2011, *astro-ph/1110.5356*  
 Beskin V., Tchekhovskoy A., 2005, *A&A*, 433, 619  
 Břřzan L., Rafferty D. A., McNamara B. R., Wise M. W., Nulsen P. E. J., 2004, *ApJ*, 607, 800  
 Bisnovatyi-Kogan G. S., Lovelace R. V. E., 2007, *ApJ*, 667, L167  
 Bisnovatyi-Kogan G. S., Lovelace R. V. E., Belinski V. A., 2002, *ApJ*, 580, 380  
 Bisnovatyi-Kogan G. S., Ruzmaikin A. A., 1974, *Ap&SS*, 28, 45  
 Bisnovatyi-Kogan G. S., Ruzmaikin A. A., 1976, *Ap&SS*, 42, 401  
 Blandford R. D., 1976, *MNRAS*, 176, 465  
 Blandford R. D., Begelman M. C., 1999, *MNRAS*, 303, L1  
 Blandford R. D., Payne D. G., 1982, *MNRAS*, 199, 883  
 Blandford R. D., Znajek R. L., 1977, *MNRAS*, 179, 433  
 Broderick A. E., McKinney J. C., 2010, *ApJ*, 725, 750  
 Burnard D. J., Arons J., Lea S. M., 1983, *ApJ*, 266, 175  
 Cao X., 2011, *ApJ*, 737, 94  
 Contopoulos I., Kazanas D., 1998, *ApJ*, 508, 859  
 Cowling T. G., 1934, *MNRAS*, 94, 768  
 Cunningham A. J., McKee C. F., Klein R. I., Krumholz M. R., Teyssier R., 2012, *ApJ*, 744, 185  
 Davis S. W., Stone J. M., Pessah M. E., 2010, *ApJ*, 713, 52  
 de Gouveia dal Pino E. M., Lazarian A., 2005, *A&A*, 441, 845  
 De Villiers J.-P., Hawley J. F., Krolik J. H., 2003, *ApJ*, 599, 1238  
 De Villiers J.-P., Hawley J. F., Krolik J. H., Hirose S., 2005, *ApJ*, 620, 878  
 Dexter J., Agol E., Fragile P. C., McKinney J. C., 2010, *ApJ*, 717, 1092  
 Dexter J., Fragile P. C., 2011, *ApJ*, 730, 36  
 Dexter J., McKinney J. C., Agol E., 2011, *astro-ph/1109.6011*  
 Dolence J. C., Gammie C. F., Shiokawa H., Noble S. C., 2012, *ApJ*, 746, L10  
 Done C., Gierliński M., 2003, *MNRAS*, 342, 1041  
 Elsner R. F., Lamb F. K., 1977, *ApJ*, 215, 897  
 Fender R. P., Belloni T. M., Gallo E., 2004, *MNRAS*, 355, 1105  
 Fernandes C. A. C., Jarvis M. J., Rawlings S., et al., 2011, *MNRAS*, 411, 1909  
 Ferrière K., 2009, *A&A*, 505, 1183  
 Fishbone L. G., Moncrief V., 1976, *ApJ*, 207, 962  
 Fragile P. C., Blaes O. M., Anninos P., Salmonson J. D., 2007, *ApJ*, 668, 417  
 Fragile P. C., Meier D. L., 2009, *ApJ*, 693, 771  
 Fu W., Lai D., 2012, *arXiv:1201.5370*  
 Gammie C. F., 1999, *ApJ*, 522, L57  
 Gammie C. F., McKinney J. C., Tóth G., 2003, *ApJ*, 589, 444  
 Gammie C. F., Shapiro S. L., McKinney J. C., 2004, *ApJ*, 602, 312  
 Ghisellini G., Della Ceca R., Volonteri M., et al., 2010, *MNRAS*, 405, 387  
 Ghosh P., Abramowicz M. A., 1997, *MNRAS*, 292, 887  
 Gierliński M., Middleton M., Ward M., Done C., 2008, *Nature*, 455, 369  
 Gierliński M., Newton J., 2006, *MNRAS*, 370, 837  
 Greiner J., Cuby J. G., McCaughrean M. J., 2001, *Nature*, 414, 522  
 Guan X., Gammie C. F., 2011, *ApJ*, 728, 130  
 Hawley J. F., Balbus S. A., 2002, *ApJ*, 573, 738  
 Hawley J. F., Balbus S. A., Stone J. M., 2001, *ApJ*, 554, L49  
 Hawley J. F., Guan X., Krolik J. H., 2011, *ApJ*, 738, 84  
 Hawley J. F., Krolik J. H., 2001, *ApJ*, 548, 348  
 Hawley J. F., Krolik J. H., 2006, *ApJ*, 641, 103  
 Heger A., Woosley S. E., Spruit H. C., 2005, *ApJ*, 626, 350  
 Henisey K. B., Blaes O. M., Fragile P. C., Ferreira B. T., 2009, *ApJ*, 706, 705  
 Ichimaru S., 1977, *ApJ*, 214, 840  
 Igumenshchev I. V., 2008, *ApJ*, 677, 317  
 Igumenshchev I. V., 2009, *ApJ*, 702, L72  
 Igumenshchev I. V., Abramowicz M. A., 2000, *ApJS*, 130, 463  
 Igumenshchev I. V., Abramowicz M. A., Narayan R., 2000, *ApJ*, 537, L27  
 Igumenshchev I. V., Narayan R., 2002, *ApJ*, 566, 137  
 Igumenshchev I. V., Narayan R., Abramowicz M. A., 2003, *ApJ*, 592, 1042  
 Johansen A., Levin Y., 2008, *A&A*, 490, 501  
 Justham S., Rappaport S., Podsiadlowski P., 2006, *MNRAS*, 366, 1415  
 Kaisig M., Tajima T., Lovelace R. V. E., 1992, *ApJ*, 386, 83  
 Kato Y., 2004, *PASJ*, 56, 931  
 King A. R., Pringle J. E., Livio M., 2007, *MNRAS*, 376, 1740  
 Komissarov S. S., Barkov M. V., 2009, *MNRAS*, 397, 1153  
 Komissarov S. S., Barkov M. V., Vlahakis N., Königl A., 2007, *MNRAS*, 380, 51  
 Komissarov S. S., McKinney J. C., 2007, *MNRAS*, 377, L49  
 Krolik J. H., 1999, *ApJ*, 515, L73  
 Kulkarni A. K., Penna R. F., Shcherbakov R. V., et al., 2011, *MNRAS*, 414, 1183  
 Kulkarni A. K., Romanova M. M., 2008, *MNRAS*, 386, 673  
 Laing R. A., Riley J. M., Longair M. S., 1983, *MNRAS*, 204, 151  
 Lamb F. K., Pethick C. J., Pines D., 1973, *ApJ*, 184, 271  
 Lang C. C., Morris M., Echevarria L., 1999, *ApJ*, 526, 727  
 LaRosa T. N., Nord M. E., Lazio T. J. W., Kassim N. E., 2004, *ApJ*, 607, 302  
 Li L., 2002, *Phys. Rev. D*, 65, 8, 084047

- Li L., Narayan R., 2004, *ApJ*, 601, 414
- Li L.-X., 2000, *ApJ*, 533, L115
- Li L.-X., Paczyński B., 2000, *ApJ*, 534, L197
- Livio M., Ogilvie G. I., Pringle J. E., 1999, *ApJ*, 512, 100
- Livio M., Pringle J. E., King A. R., 2003, *ApJ*, 593, 184
- Lovelace R. V. E., 1976, *Nature*, 262, 649
- Lovelace R. V. E., Romanova M. M., Newman W. I., 1994, *ApJ*, 437, 136
- Lubow S. H., Papaloizou J. C. B., Pringle J. E., 1994, *MNRAS*, 267, 235
- Lubow S. H., Spruit H. C., 1995, *ApJ*, 445, 337
- Lyutikov M., McKinney J. C., 2011, *Phys. Rev. D*, 84, 8, 084019
- MacDonald D. A., 1984, *MNRAS*, 211, 313
- Machida M., Hayashi M. R., Matsumoto R., 2000, *ApJ*, 532, L67
- Machida M., Matsumoto R., 2003, *ApJ*, 585, 429
- Machida M., Matsumoto R., 2008, *PASJ*, 60, 613
- Machida M., Nakamura K. E., Matsumoto R., 2006, *PASJ*, 58, 193
- Mahmud M., Gabuzda D. C., Bezrukovs V., 2009, *MNRAS*, 400, 2
- McKinney J. C., 2005, *ApJ*, 630, L5
- McKinney J. C., 2006a, *MNRAS*, 367, 1797
- McKinney J. C., 2006b, *MNRAS*, 368, 1561
- McKinney J. C., Blandford R. D., 2009, *MNRAS*, 394, L126
- McKinney J. C., Gammie C. F., 2002, *ApJ*, 573, 728
- McKinney J. C., Gammie C. F., 2004, *ApJ*, 611, 977
- McKinney J. C., Narayan R., 2007a, *MNRAS*, 375, 513
- McKinney J. C., Narayan R., 2007b, *MNRAS*, 375, 531
- McKinney J. C., Uzdensky D. A., 2012, *MNRAS*, 419, 573
- McNamara B. R., Rohanizadegan M., Nulsen P. E. J., 2011, *ApJ*, 727, 39
- Meier D. L., 2001, *ApJ*, 548, L9
- Mestel L., Strittmatter P. A., 1967, *MNRAS*, 137, 95
- Meyer L., Do T., Ghez A., et al., 2008, *ApJ*, 688, L17
- Mignone A., McKinney J. C., 2007, *MNRAS*, 378, 1118
- Mineshige S., Kusnose M., Matsumoto R., 1995, *ApJ*, 445, L43
- Mondal S., Basu P., Chakrabarti S. K., 2009, *MNRAS*, 396, 1038
- Muñoz D. J., Marrone D. P., Moran J. M., Rao R., 2012, *ApJ*, 745, 115
- Nakamura M. S., Matsumoto H., Fujimoto M., 2002, *Geophys. Res. Lett.*, 29, 8, 1247
- Narayan R., Igumenshchev I. V., Abramowicz M. A., 2000, *ApJ*, 539, 798
- Narayan R., Igumenshchev I. V., Abramowicz M. A., 2003, *PASJ*, 55, L69
- Narayan R., McClintock J. E., 2012, *MNRAS*, 419, L69
- Narayan R., McKinney J. C., Farmer A. J., 2007, *MNRAS*, 375, 548
- Narayan R., Paczyński B., Piran T., 1992, *ApJ*, 395, L83
- Narayan R., Yi I., 1994, *ApJ*, 428, L13
- Narayan R., Yi I., 1995a, *ApJ*, 444, 231
- Narayan R., Yi I., 1995b, *ApJ*, 452, 710
- Noble S. C., Gammie C. F., McKinney J. C., Del Zanna L., 2006, *ApJ*, 641, 626
- Noble S. C., Krolik J. H., Hawley J. F., 2009, *ApJ*, 692, 411
- Noble S. C., Krolik J. H., Hawley J. F., 2010, *astro-ph/1001.4809*
- Novikov I. D., Thorne K. S., 1973, in *Black Holes*, (Eds C De Witt, B S De Witt) (London: Gordon and Breach, 1973)
- Oda H., Machida M., Nakamura K. E., Matsumoto R., 2007, *PASJ*, 59, 457
- Oda H., Machida M., Nakamura K. E., Matsumoto R., 2009, *ApJ*, 697, 16
- Oda H., Machida M., Nakamura K. E., Matsumoto R., 2010, *ApJ*, 712, 639
- Ogle P., Whysong D., Antonucci R., 2006, *ApJ*, 647, 161
- O'Neill S. M., Reynolds C. S., Miller M. C., 2009, *ApJ*, 693, 1100
- O'Neill S. M., Reynolds C. S., Miller M. C., Sorathia K. A., 2011, *ApJ*, 736, 107
- Page D. N., Thorne K. S., 1974, *ApJ*, 191, 499
- Pang B., Pen U.-L., Matzner C. D., Green S. R., Liebendörfer M., 2011, *MNRAS*, 415, 1228
- Parker E. N., 1966, *ApJ*, 145, 811
- Pen U.-L., Matzner C. D., Wong S., 2003, *ApJ*, 596, L207
- Penna R. F., McKinney J. C., Narayan R., Tchekhovskoy A., Shafee R., McClintock J. E., 2010, *MNRAS*, 408, 752
- Penna R. F., Sądowski A., McKinney J. C., 2012, *MNRAS*, 420, 684
- Pessah M. E., Psaltis D., 2005, *ApJ*, 628, 879
- Popham R., Gammie C. F., 1998, *ApJ*, 504, 419
- Press W. H., Flannery B. P., Teukolsky S. A., 1986, *Numerical recipes. The art of scientific computing*
- Proga D., Begelman M. C., 2003, *ApJ*, 592, 767
- Proga D., Zhang B., 2006, *MNRAS*, 370, L61
- Psaltis D., Belloni T., van der Klis M., 1999, *ApJ*, 520, 262
- Punsly B., 2011, *ApJ*, 728, L17+
- Punsly B., Coroniti F. V., 1990, *ApJ*, 354, 583
- Punsly B., Igumenshchev I. V., Hirose S., 2009, *ApJ*, 704, 1065
- Quataert E., Gruzinov A., 2000, *ApJ*, 539, 809
- Remillard R. A., 2005, *Astronomische Nachrichten*, 326, 804
- Remillard R. A., McClintock J. E., 2006, *ARA&A*, 44, 49
- Reynolds C. S., Garofalo D., Begelman M. C., 2006, *ApJ*, 651, 1023
- Reynolds C. S., Miller M. C., 2009, *ApJ*, 692, 869
- Richards G. T., Lacy M., Storrie-Lombardi L. J., et al., 2006, *ApJS*, 166, 470
- Romanova M. M., Kulkarni A. K., Lovelace R. V. E., 2008, *ApJ*, 673, L171
- Romanova M. M., Ustyugova G. V., Koldoba A. V., Lovelace R. V. E., 2011, *astro-ph/1111.3068*
- Rothstein D. M., Lovelace R. V. E., 2008, *ApJ*, 677, 1221
- Rubio-Herrera E., Lee W. H., 2005, *MNRAS*, 357, L31
- Rutledge R. E., Lewin W. H. G., van der Klis M., et al., 1999, *ApJS*, 124, 265
- Sano T., Inutsuka S., Turner N. J., Stone J. M., 2004, *ApJ*, 605, 321
- Scharlemann E. T., 1978, *ApJ*, 219, 617
- Schnittman J. D., Krolik J. H., Hawley J. F., 2006, *ApJ*, 651, 1031
- Shafee R., McKinney J. C., Narayan R., Tchekhovskoy A., Gammie C. F., McClintock J. E., 2008, *ApJ*, 687, L25
- Shakura N. I., Sunyaev R. A., 1973, *A&A*, 24, 337
- Shcherbakov R. V., Penna R. F., McKinney J. C., 2010, *astro-ph/1007.4832*
- Shibata K., Tajima T., Matsumoto R., 1990, *ApJ*, 350, 295
- Shiokawa H., Dolence J. C., Gammie C. F., Noble S. C., 2012, *ApJ*, 744, 187
- Shu F., Najita J., Ostriker E., Wilkin F., Ruden S., Lizano S., 1994, *ApJ*, 429, 781
- Sorathia K. A., Reynolds C. S., Armitage P. J., 2010, *ApJ*, 712, 1241
- Sorathia K. A., Reynolds C. S., Stone J. M., Beckwith K., 2011, *arXiv:1106.4019*
- Spruit H. C., Stehle R., Papaloizou J. C. B., 1995, *MNRAS*, 275, 1223
- Spruit H. C., Uzdensky D. A., 2005, *ApJ*, 629, 960
- Stehle R., Spruit H. C., 2001, *MNRAS*, 323, 587
- Stella L., Vietri M., 1999, *Physical Review Letters*, 82, 17
- Stone J. M., Gardiner T., 2007, *ApJ*, 671, 1726
- Stone J. M., Pringle J. E., 2001, *MNRAS*, 322, 461
- Stone J. M., Pringle J. E., Begelman M. C., 1999, *MNRAS*, 310, 1002
- Tagger M., Pellat R., 1999, *A&A*, 349, 1003
- Tchekhovskoy A., McKinney J. C., 2012, *ArXiv:1201.4385*
- Tchekhovskoy A., McKinney J. C., Narayan R., 2007, *MNRAS*, 379, 469
- Tchekhovskoy A., McKinney J. C., Narayan R., 2009, *ApJ*, 699, 1789
- Tchekhovskoy A., McKinney J. C., Narayan R., 2012, *arXiv:1202.2864*
- Tchekhovskoy A., Narayan R., McKinney J. C., 2010a, *ApJ*, 711, 50
- Tchekhovskoy A., Narayan R., McKinney J. C., 2010b, *New Astronomy*, 15, 749
- Tchekhovskoy A., Narayan R., McKinney J. C., 2011, *MNRAS*, 418, L79
- Thorne K. S., 1974, *ApJ*, 191, 507
- Tout C. A., Pringle J. E., 1996, *MNRAS*, 281, 219
- Uzdensky D. A., McKinney J. C., 2011, *Physics of Plasmas*, 18, 4, 042105
- Vallée J. P., 2011, *New Astronomy Reviews*, 55, 91
- van der Klis M., 1998, *Advances in Space Research*, 22, 925
- Vaughan S., Uttley P., 2005, *MNRAS*, 362, 235
- Wang Y.-M., 1984, *Advances in Space Research*, 3, 327
- Wang Y.-M., 1996, *ApJ*, 465, L111+
- Wijnands R., van der Klis M., 1999, *ApJ*, 514, 939
- Willott C. J., Rawlings S., Blundell K. M., Lacy M., 1999, *MNRAS*, 309, 1017
- Woosley S. E., Langer N., Weaver T. A., 1993, *ApJ*, 411, 823
- Znajek R., 1976, *Nature*, 262, 270